Universidade de São Paulo
Instituto de Física

Dinâmica caótica em potenciais periódicos

Matheus Jean Lazarotto

Orientador
Prof. Dr. Iberê Luiz Caldas

Co-orientador
Prof. Dr. Yves Elskens

Tese de doutorado apresentada ao Instituto de Física da Universidade de São Paulo como requisito parcial para a obtenção do título de doutor em ciências.

Banca examinadora:
Prof. Dr. Iberê Luiz Caldas – Orientador (IFUSP, São Paulo/SP)
Prof. Dr. Ricardo Luiz Viana (IFUSP, São Paulo/SP)
Prof. Dr. Clodoaldo Grotta Ragazzo (IME-USP, São Paulo/SP)
Prof. Dr. Renato Pakter (UFRGS, Porto Alegre/RS)
Prof. Dr. Rafael Ribeiro Dias Vilela de Oliveira (UFABC, Santo André/SP)

São Paulo
2023

FICHA CATALOGRÁFICA
Preparada pelo Serviço de Biblioteca e Informação
do Instituto de Física da Universidade de São Paulo

Lazarotto, Matheus Jean

Dinâmica caótica em potenciais periódicos. São Paulo, 2023.

Tese (Doutorado) - Universidade de São Paulo. Instituto de Física. Depto. de Física Aplicada.

Orientador: Prof. Dr. Iberê Luiz Caldas

Área de Concentração: Física.

Unitermos: 1. Caos Hamiltoniano; 2. Sistemas dinâmicos; 3. Difusão; 4. Potencial periódico.

USP/IF/SBI-023/2023

University of São Paulo
Physics Institute

Chaotic dynamics in periodic potentials

Matheus Jean Lazarotto

Oriented by
Prof. Dr. Iberê Luiz Caldas

Co-oriented by
Prof. Dr. Yves Elskens

Thesis submitted to the Physics Institute of the University of São Paulo in partial fulfillment of the requirements for the degree of Doctor of Science.

Examining committee:
Prof. Dr. Iberê Luiz Caldas – Supervisor (IFUSP, São Paulo/SP)
Prof. Dr. Ricardo Luiz Viana (IFUSP, São Paulo/SP)
Prof. Dr. Clodoaldo Grotta Ragazzo (IME-USP, São Paulo/SP)
Prof. Dr. Renato Pakter (UFRGS, Porto Alegre/RS)
Prof. Dr. Rafael Ribeiro Dias Vilela de Oliveira (UFABC, Santo André/SP)

São Paulo
2023

Agradecimentos

O presente trabalho foi realizado com o apoio financeiro do CNPq (processo 141750/2019-7), permitindo dedicação integral à pesquisa, e conjuntamente das agências CAPES e COFECUB (processo 88887.628292/2021-00), pela promoção de um estágio na *Aix-Marseille Université*. The authors acknowledge the *Centre do Calcul Intensif d'Aix-Marseille Université* for granting access to its high performance computing resources.

Ao longo dos 4 anos em que este trabalho foi realizado, o meio acadêmico me proporcionou o privilégio de conviver e conhecer um número maior de pessoas de que tenho espaço para o devido agradecimento, porém, alguns exigem menção.

Agradeço a Iberê Caldas, por partilhar de sua experiência e pela gentileza e oportunidades concedidas desde os primeiros dias de trabalho.

To Yves Elskens, for all the cordiality and attention devoted and for the patient sharing of his experience, keeping me critical along all the work.

To all the friends scattered around the world that I had the fortuitous pleasure of meeting in Marseille. A short but forever memorable experience.

À todos os amigos que fiz na Universidade de São Paulo, por compartilharem das vicissitudes da vida acadêmica e por tornarem a universidade mais do que um local de trabalho. Aos amigos de outrora, por manterem-se perto, apesar da distância.

À Larissa, por toda a motivação, apoio e por dividir os fardos que o tempo de trabalho exigiu.

À Vanessa e ao Bruno, pelo acolhimento e conforto que me proporcionaram, desde os meus primeiros dias em São Paulo.

Aos meus pais, Rildo e Clarice, por todos os sacrifícios e afetos, desde os primeiros dias de escola, hoje e sempre.

Interviewer: *'You wrote on the back of one album: 'I accept chaos, does it accept me?"*
Bob Dylan: *'Chaos is a friend of mine. It's like I accept him, does he accept me?.'*
Interviewer: *'Do you see the world as chaos?'*
Bob Dylan: *'Truth is chaos. Maybe beauty is chaos.'*

Interview published in *"A retrospective"* by Craig McGregor (1965)

Abstract

Spatial diffusion of particles in periodic potential models has provided a good framework for studying the role of chaos in global properties of classical systems. Here a square-symmetric potential, classically modeled from an optical lattice Hamiltonian system, was initially used to numerically study diffusion transitions under variation of the control parameters. Sudden transitions between normal and ballistic regimes were found and characterized by inspection of topological changes taking place in phase-space. Particular transitions, correlated with increases in global stability area, were seen to occur for energy levels where local maxima points become accessible, deviating trajectories approaching them. These instabilities promote a slowing down of the dynamics and an island myriad bifurcation phenomenon, along with the suppression of long flights within the lattice.

On further investigating the island myriad, its structure was found to be intimately related to the translational and rotational symmetries of the lattice potential. With a high fractal pattern, the myriad of islands is concentrically organized in isochronous chains, formed either by orbits with limited range or high escape transport. As the local maxima points change with the control parameters, the bifurcation of each chain sequentially follows a separatrix reconnection, as in a local non-twist scenario. Due to the myriad's dependence on the tiling symmetry property of the square lattice, its presence was conjectured and confirmed also for a hexagonal lattice, although found in attenuated form due to extra instabilities in the potential. Beyond that, the numerical techniques applied for analyses along this work are of wide use and can be adapted to generic conservative systems, allowing their study as their parameters change in an automated way.

Key-words: Diffusion, Periodic potential, Hamiltonian chaos, Dynamical Systems

Resumo

A difusão espacial de partículas em potenciais periódicos têm fornecido bons cenários para o estudo do papel do caos em propriedades globais na dinâmica de sistemas clássicos. Neste trabalho, um potencial de simetria quadrada, classicamente modelado a partir de um Hamiltoniano de rede óptica, foi inicialmente usado para o estudo de transições de difusão conforme a variação dos parâmetros de controle. Transições repentinas entre os regimes normal e balístico de difusão foram encontradas e descritas em termos das mudanças topológicas acontecendo no espaço de fase. Em particular, transições correlacionadas com aumentos na área de estabilidade foram vistas para níveis de energia onde máximos locais do potencial tornam-se acessíveis. Estas instabilidades promovem uma desaceleração da dinâmica e um fenômeno de miríade de ilhas, assim como a supressão de voos longos na rede.

Ao se investigar o fenômeno de miríade em detalhe, sua estrutura foi vista ser intimamente ligada às simetrias translacional e rotacional do potencial da rede. Com alta fractalidade, a miríade de ilhas organiza-se em camadas concêntricas de cadeias isócronas, formadas tanto por órbitas de alcance limitado ou com alto transporte para escape. Conforme os pontos de máximo local variam com os parâmetros de controle, as cadeias de ilha sequencialmente bifurcam seguindo reconexões de separatriz, em um cenário local não-*twist*. Devido à dependência com a simetria de preenchimento da rede quadrada, a presença da miríade foi conjecturada e confirmada também para uma rede hexagonal, porém, em forma atenuada devido à fontes extras de instabilidade do potencial. Além destes resultados, os métodos numéricos aplicados em análises ao longo deste trabalho são de ampla aplicação e adaptáveis à sistemas dinâmicos genéricos, permitindo a automação de seu estudo conforme seus parâmetros de controle mudam.

Palavras-chave: Difusão, Potencial periódico, Caos Hamiltoniano, Sistemas dinâmicos

Contents

List of symbols and abbreviations

$H(x, y, p_x, p_y)$ — Hamiltonian function

$x, y, \vec{r}$ — Spatial positions

$p_x, p_y, \vec{p}$ — Canonical momenta

$V(x, y)$ — Potential energy function

V_{saddle} — Potential saddle point energy

$V_{\text{l-max}}$ — Potential local maxima point energy

$V_{\text{g-max}}$ — Potential global maxima point energy

E — Energy (numerically equal to H)

α — Coupling parameter between laser waves

$\vec{s}$ — System state vector

μ — Diffusion exponent

$\mathbf{M}$ — Monodromy matrix

$W_{u,s}$ — Unstable (u) or Stable (s) manifold

RKCK — Runge-Kutta-Cash-Karp

PBC — Periodic boundary conditions

PSS — Poincaré surface section (also symbolized as Σ)

PO — Periodic orbit

SPO — Stable periodic orbit

UPO — Unstable periodic orbit

List of Figures

List of Tables

1

Introduction

"O caos é mais divertido do que a ordem."
Ricardo Araújo Pereira, *Diário de Notícias* (2004)

From a wide range of experimental scenarios, periodic potential functions arise as simple yet rich models to a diversity of physical systems. Ranging from cold gases in optical lattices [1–3], to ionic particles submitted to guided waves in $\mathbf{E} \times \mathbf{B}$ fields and plasma physics [4, 5], to wave propagation in photonic crystals [6], and to xenon atoms diffusion over platinum surfaces [7], periodic potentials provide a mathematical description for the dynamical behavior of such systems.

Within the field of condensed matter physics, one may find optical lattices as experimental devices used to confine and control ultra-cold atoms from Lorentz gases or Bose-Einstein condensates. These lattices are created from the superposition of multiple stationary laser waves, which allow the imprisonment of particles inside the wave's minima regions [2]. Thus, given the natural periodicity of the waves that shape the lattice, the confined particles dynamics is promptly described by a Hamiltonian formulation with a periodic potential modeling the wave-particle interaction. It is this experimental setup that motivates the mathematical model subjected to study for this work.

Experimentally, the use of these devices, besides confining and control, is to allow the study of quantum properties of matter, such as energy bands structures with Dirac points or quantum-classical correspondence of chaos for many-body systems, including, in the latter, matter waves [1]. As shown by Thommen [8] and Mitchell [9], particles in quantum lattices could present a behavior similar to classical chaos and fractality. Similarly, as proposed by Prants [10, 11], inspired by a semi-classical model considering the particle-field interaction for two-level atoms, the effect of chaos in particles displacement could be observed experimentally.

From the theoretical perspective, particularly in classical dynamics, periodic dynamical systems often appear as one of two ways. Either as classical billiards, where particles move freely and collide with hard walls (Sinai billiards [12] – fig. 1), or as Hamiltonian functions with a periodic potential. Billiard systems have been widely used as simple models for Lorentz gases [13–15], where particles do not interact with each other and are scattered by colliding with a series of surfaces. Such systems are usually studied via discrete maps, or, whenever possible, with solutions via geometrical considerations. Alternatively, in Hamiltonian formulations, particles are constrained to move in a smooth potential surface (fig. 2) instead of bouncing between hard walls, thus being referred to as 'soft' billiards. In this case, the dynamical evolution requires the integration of the equations of motion.

The Hamiltonian scenario is particularly interesting since it provides the main framework for deterministic chaos, where 'stochastic'-like behavior emerges without the application of random variables, being due purely to instabilities. It is possible to observe either regular behavior (integrable trajectories) or chaotic motion (non-integrable) and often the simultaneous presence of both kinds.

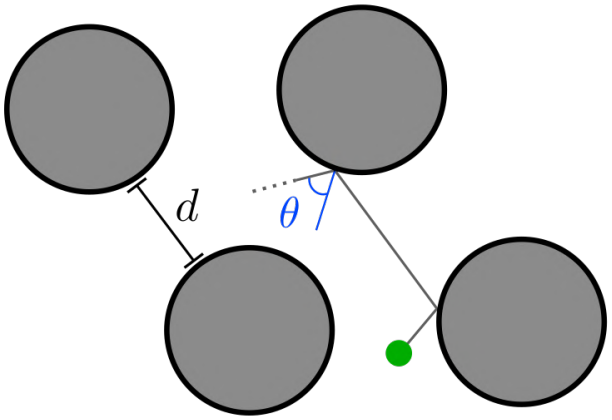

Figure 1: Representation of a periodic Sinai billiard. The distance d between the scatterer circles is taken as the control parameter of the system. Reflections with hard walls are assumed to be specular, *i.e.* the incident and reflected angles are equal.

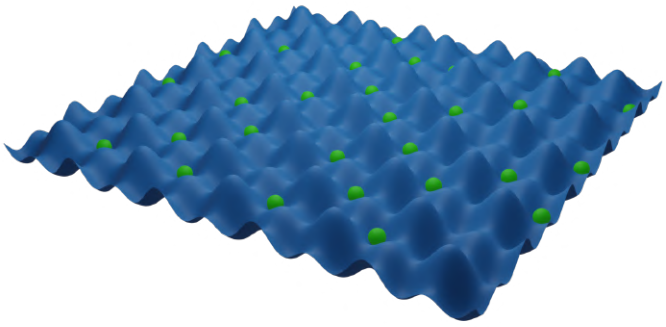

Figure 2: Representation of a smooth potential surface from a bidimensional lattice. The particles (in green) can either remain trapped in the minima regions or travel between multiple lattice cells.

Among theoretical studies, diffusion is often the main inquired topic, that is, the evaluation of spatial dispersion of particles throughout a given lattice and its dependence with control parameters [13–15]. Special emphasis is given on understanding how such systems can present diffusion regimes away from normal (*i.e.* anomalous diffusion), where the squared average displacement of an ensemble of particles does not grow linearly as $t \to \infty$, as in the case of the normal regime in a classical random-walk or brownian motion for example, but instead it presents growth rates with any deviation from linear. As aforementioned, since movement in these models is oftentimes considered to occur without collisions between particles or application of random forces, any deviation from normal behavior is purely due to unstable solutions and their consequential chaos, thus making these models a good framework for the study of chaotic dynamics.

Indeed, in previous studies for soft billiards, Zaslavsky performed some of the prominent works for continuous flows and Hamiltonian models considering the variation of control parameters [15–17]. Particularly in [17], for a periodic Q-model, were shown the existence of long flights within the chaotic motion, the consequent anomalous diffusion regime, the tail thickening effect in the position power-law distribution, and the occurrence of sudden transitions in diffusion rate as a function of a control parameter. Similarly, Argonov and Prants [18–20] showed the fractal structure of escape time basins and the effect of chaos in different diffusion regimes due to Lévy flights. The connection between these

flights and anomalous regimes has been shown for a wide variety of models [4, 17, 21, 22], including systems analogous to the one considered in this work.

Few recent works considered the same models selected for study here, with particular mention to Horsley *et al.* [23], for a work on the square lattice, and Porter [24], for the hexagonal one. Regarding classical aspects on quantum models, Porter [25] considered a modified topology for the square lattice, including a quantum calculation for energy bands and the effect of symmetry breaking. In [26], Prants studies the same Hamiltonian function used here but taking into account a dipole-field interaction, in a semi-classical approach. Although these works provided a classical treatment of the Hamiltonian and presented the mixed nature of its phase-space, they did not consider diffusion and its dependence on control parameters, nor the properties of phase-space for this matter, thus differing in spirit and purpose from this current work.

Therewith, guided by this theoretical background, this thesis focuses on numerical studies on the classical dynamics of particles in a 2D lattice system. Considering a Hamiltonian model with a bidimensional periodic potential, inspired by an optical lattice, the diffusion of particles for a lattice with square symmetry was initially investigated. We thus aimed to understand how some transitions in diffusion rate occur as the control parameters of the system vary, namely its total energy and the couplings of waves that form the lattice. Complementary details on the phase-space structure are given to describe these diffusion transitions via a series of numerical techniques. Later, as will be detailed in the following chapters, a particular structure found in phase-space, namely an island myriad bifurcation, is further investigated. Additionally for this purpose, a second lattice model, with hexagonal symmetry, is also considered to provide information on the phenomenon. We aimed to understand the role of classical chaos in dynamics and how the symmetry properties of the potential simplify and give rise to particular structures in phase-space. The applied numerical techniques themselves are also worth exploration as they are widely applicable to conservative dynamical systems beyond the ones shown here and allow for the automation of many phase-space diagnostics.

In what follows, chapter 2 starts by presenting Hamiltonian models for optical lattices (sec. 2.1), emphasizing details on the potential functions used to model the square (sec. 2.2) and hexagonal lattices (sec. 5.3). Chapter 3 then presents the numerical methods and dynamical systems theory used for phase-space diagnostics, from numerical integration of the motion equations (sec 3.1), to the calculation of diffusion exponent (sec 3.2) and algorithms for the search of periodic orbits (sec 3.3), manifolds (sec 3.4) and chaotic area measurement (sec 3.5). The main results obtained are organized into two chapters, starting in chapter 4, regarding the behavior of the diffusion exponent μ as a function of the control parameters (sec. 4.1), and the description of the diffusion transitions found, considering the chaotic area (sec. 4.2), phase-space portraits (sec. 4.3) and bifurcation of periodic orbits (sec. 4.4). Lastly, the island myriad phenomenon is discussed in detail

in chapter 5, with its structure described in terms of the main periodic orbits (sec. 5.1) and how they evolve with the control parameters (sec. 5.2). The myriad phenomenon was also conjectured and investigated for the hexagonal lattice potential (sec. 5.3). Complementary information is provided in an appendix at the end and will be pointed out through the text as they become suitable.

2

Hamiltonian models

"The simplicities of natural laws arise through the complexities of the language we use for their expression."

Eugene Paul Wigner, *Communications on Pure and Applied Algebra* (1959)

The two Hamiltonian models selected for our study consist of a purely classical description based on optical lattices. We start by showing how the imprisonment of particles is achieved in these lattices while deducing the resulting potential function to which they are submitted (sec. 2.1). Next, details on the two potentials geometry are described, one with square symmetry (sec. 2.2) and another with hexagonal symmetry (sec. 2.3), and how their control parameters, namely the couplings, affect their topology. Equilibrium points and symmetry properties are listed since they are of primal importance to describe the dynamics and will be referred to along all this work.

2.1 Lattice Hamiltonians

In an optical lattice, the trapping of neutral atoms is realized by the interaction between each particle and a monochromatic standing laser wave [2]. When any wave is reflected along its propagation direction with the specific phase that generates a constructive superposition of the incoming and the reflected waves, the result is a stationary pattern, a sort of constant 'frozen' picture of it in time. For a laser, this state is achieved with a pair of parallel and opposing mirrors for example.

Once a neutral particle interacts with such a wave, in spite of its null electrical charge, the electric field will induce an oscillating dipole moment $\vec{d}$ in the particle along the wave's polarization direction (fig. 3) given by

$$\vec{d}(t) = \rho(\omega)\vec{E}(\vec{r}, t), \tag{2.1}$$

where $\vec{r} = (x, y, z)$ is the spatial position and ρ a polarizability factor dependent on the wave angular frequency ω. This frequency shall not be close to the particle's resonance frequency ω_R, otherwise absorbing the radiation and changing internal energy states, producing a different dipolar response than the linear one from eq. 2.1. Also, since the time scale for the center-of-mass motion of atoms is much slower than the inverse driving frequency ω^{-1}, the interaction with the field is well approximated by its time-averaged intensity.

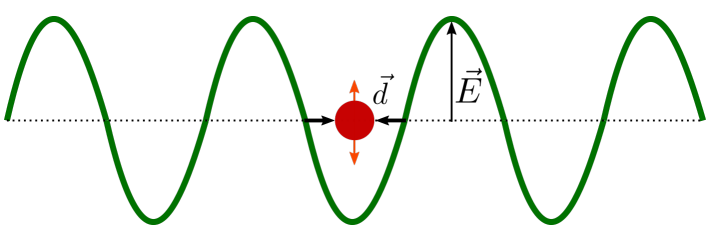

Figure 3: Schematic representation of a particle trapped by a standing laser wave. The electrical field $\vec{E}$ induces a dipole $\vec{d}$ that furthers re-interacts with the field, causing horizontal forces that constrain the particle's movement along the wave propagation axis (dotted line).

Once induced, the dipole re-interacts with the field further submitting the particle to

a potential with amplitude directly proportional to the laser intensity [1, 27]

$$V_{\text{dip}}(\vec{r}) = -\langle \vec{d}(t) \cdot \vec{E}(\vec{r}, t) \rangle = -\frac{1}{2}\rho(\omega)|\vec{E}(\vec{r})|^2, \tag{2.2}$$

with the brackets denoting time average over rapid oscillating frequencies; thereby yielding a force with direction perpendicular to the wave polarization axis

$$\vec{F}_{\text{dip}} = -\nabla V_{\text{dip}} = \frac{1}{2}\rho(\omega)\nabla|\vec{E}(\vec{r})|^2. \tag{2.3}$$

Therewith, the particle is constantly being pushed towards the wave minima point under the action of this restoring force, thus becoming trapped along the wave's propagation direction.

Applying stationary waves along multiple axes, one can trap the particle along a 1D line, a 2D surface or a 3D 'crystal' lattice. These setups are illustrated in figure 4 for the 2D and 3D cases. For physical scale reference, as obtained by Greiner *et al.* [28, 29], half a million Rubidium (^{87}Rb) atoms were stored inside a cigar-shaped magnetic cage of approximate size of 45×4 μm. The unit cell size of the lattice is given by the wavelength ($\lambda = 852$ nm).

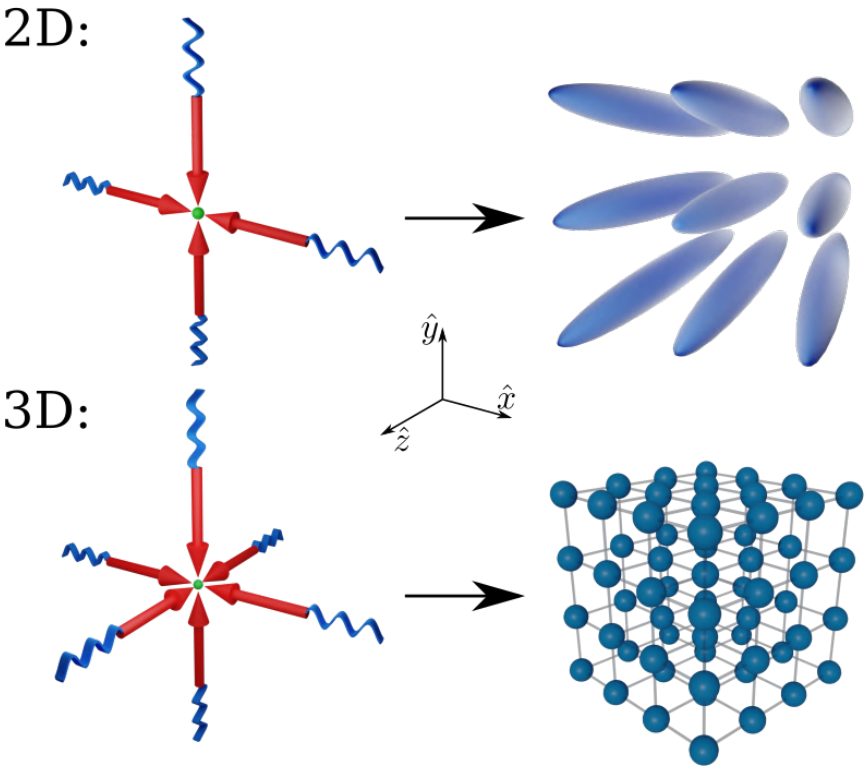

Figure 4: Schematic representation of two optical lattice setups, for 2D and 3D lattices. In the left column, the incoming and reflected wave pairs (forming a standing wave) in orthogonal directions. In the right column, the spatial 3D representation of the confinement region where particles are trapped. Reproduction based on I. Bloch *et al.* [1].

Generically, the potential function for any optical lattice can be written as the superposition of the multiple electrical fields from each incident wave. Writing the field for N

monochromatic waves, one has

$$\vec{E}_{\text{latt}}(\vec{r},t) = \sum_{i=1}^{N} \hat{e}_i \; E_0^i \cos\left(\vec{k}_i \cdot \vec{r} + \phi_i - \omega t\right), \tag{2.4}$$

with $\hat{e}_i$ as the polarization versor, $\vec{k}_i$ the wave-vector and ϕ_i an arbitrary phase. From eq. 2.2, the resulting lattice potential is then

$$V_{\text{latt}}\left(\vec{r}\right) = \frac{1}{2}\rho(\omega)E_0^2\left(\sum_{i=1}^{N}\cos^2\left(\vec{k}_i\cdot\vec{r}\right) + 2\sum_{i=1}^{N}\sum_{j>i}^{N}\alpha_{ij}\cos\left(\vec{k}_i\cdot\vec{r}\right)\cos\left(\vec{k}_j\cdot\vec{r}\right)\right), \tag{2.5}$$

where the amplitudes E_0^i are also taken as equal for simplicity. The coefficients α_{ij} are the superposition coupling between waves i and j, and stand for the product of polarization directions and phase difference: $\alpha_{ij} = (\hat{e}_i \cdot \hat{e}_j)\cos(\phi_i - \phi_j)$. They are, therefore, accessible parameters to be controlled in the laboratory either by turning the laser beam direction or the mirrors position to alter their relative phase.

As presented in the context of condensed matter, particles in optical lattices are quantum systems and are thus described by wave functions and their dynamics by the Schrödinger equation. However, spatial trajectories within the lattice may be regarded as classical when interaction between pairs is negligible [1]. Therefore, the classical Hamiltonian model to be studied here can not be assumed as a faithful representation for an experimental Bose-Einstein condensate, but instead, it is motivated by it and will be treated in a purely classical scheme. Connections between the classical and quantum regimes can be made from periodic classical solutions or even a correspondence between classical and quantum chaos and tunneling [8, 30–33], although none of these topics are treated in this work.

2.2 Square lattice

The potential form in equation 2.5 stands for the most generic lattice possible, with the combination of multiple waves and incidence orientations of $\vec{k}_i$. For a 2D lattice, all laser beams must be co-planar and at least two of them linearly independent, constraining the particle movement along two cartesian axes. Three or more waves propagating in the same $(\vec{k}_1, \vec{k}_2)$ plane can be placed in order to achieve different topologies, as will be shown in section 2.3 for the hexagonal lattice.

The main lattice model considered here is a bidimensional one formed by two orthogonal waves in the (x, y) plane, as shown by the correspondent electrical fields in figure 5. Writing the total field as the linear superposition of each stationary wave, the lattice field reads

$$\vec{E}(\vec{r},t) = E_{0x}\cos(k_x x + \phi_x)e^{-i\omega_x t}\;\hat{e}_x + E_{0y}\cos(k_y y + \phi_y)e^{-i\omega_y t}\;\hat{e}_y, \tag{2.6}$$

Note that the polarization directions $\hat{e}_x$ and $\hat{e}_y$ are contained respectively in the planes (z, y) and (z, x), but can have any orientation in these planes.

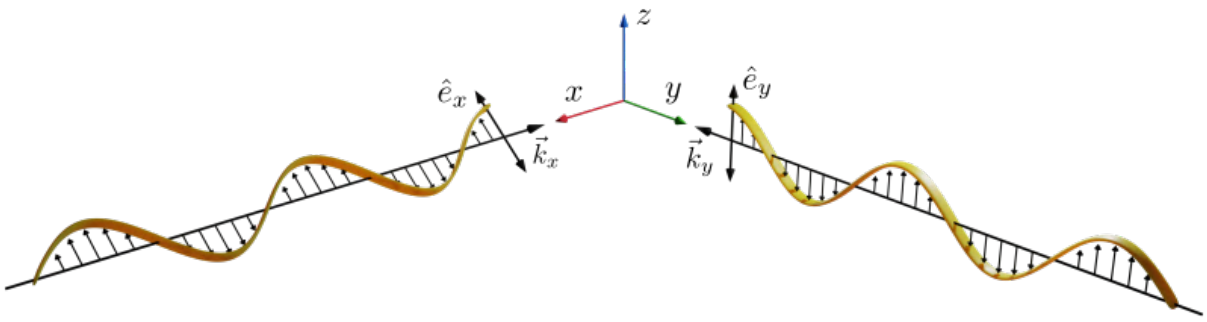

Figure 5: Schematic representation of the two orthogonal electrical wave fields $\vec{E}_x$ and $\vec{E}_y$ that form a bidimensional lattice.

For simplicity, both waves will be assumed as identical, meaning that wave vectors $\vec{k}_x = k\hat{x}, \vec{k}_y = k\hat{y}$, frequencies $\omega_x = \omega_y = \omega$ and amplitudes $E_0^x = E_0^y = E_0$ are chosen to be the same. Thereupon, substituting equation 2.6 into equation 2.2 provides the potential function for the 2D square lattice:

$$V_{\text{dip}}(x', y') = \frac{1}{2}\rho(\omega)E_0^2\left(\cos^2(kx') + \cos^2(ky') + 2\alpha\cos(kx')\cos(ky')\right). \tag{2.7}$$

The lattice system is thus composed of a classical particle moving on a potential surface given by equation 2.7, as illustrated in figure 2 in the introductory chapter.

The complete dynamical model will be given by the classical Hamiltonian

$$H'(x', y', p'_x, p'_y) = \frac{1}{2m}\left((p'_x)^2 + (p'_y)^2\right) + U'\left(\cos^2(kx') + \cos^2(ky') + 2\alpha\cos(kx')\cos(ky')\right), \tag{2.8}$$

where (p'_x, p'_y) are canonical momenta, m is the mass and $U' = \frac{1}{2}\rho(\omega)E_0^2 > 0$ an energy scale parameter; as previously mentioned, the coupling is $\alpha = (\hat{e}_x \cdot \hat{e}_y)\cos(\phi_x - \phi_y)$. By re-scaling space units to $(x = kx', y = ky')$, momenta $(p_x, p_y) = (\frac{p'_x}{\sqrt{2m}}, \frac{p'_y}{\sqrt{2m}})$ and energy $H = 2mH'$, so that energy scale is $U = 2mU'$, the Hamiltonian is simplified to

$$H(x, y, p_x, p_y) = p_x^2 + p_y^2 + U\left(\cos^2(x) + \cos^2(y) + 2\alpha\cos(x)\cos(y)\right). \tag{2.9}$$

Since the Hamiltonian function in equation 2.9 is time-independent, the dynamics of particles is conservative and has H itself as a constant of the motion, further identified as the total energy $E = H$.

The energy scale U is of no relevance in the classical regime, in the sense that it does not alter the topology of solutions whatsoever, and can be set to 1 by rescaling time. In the quantum regime on the other hand, this energy scale relates to the accessible eigenstates and thus has further relevance. For this study, we fix $U = 20$ following Horsley *et al.* [23]

since it is a feasible value obtainable in experiments.

As seen from potential 2.7, the parameter α acts as a perturbation to the integrable Hamiltonian of two pendulum-like potentials along x and y, coupling them for any $\alpha \neq 0$. Although α ranges in the interval $[-1, 1]$, it is only required to consider solutions for $[0, 1]$, since the negative counterpart is equivalent to a spatial translation by π in one of the cartesian directions, thus not altering solutions properties.

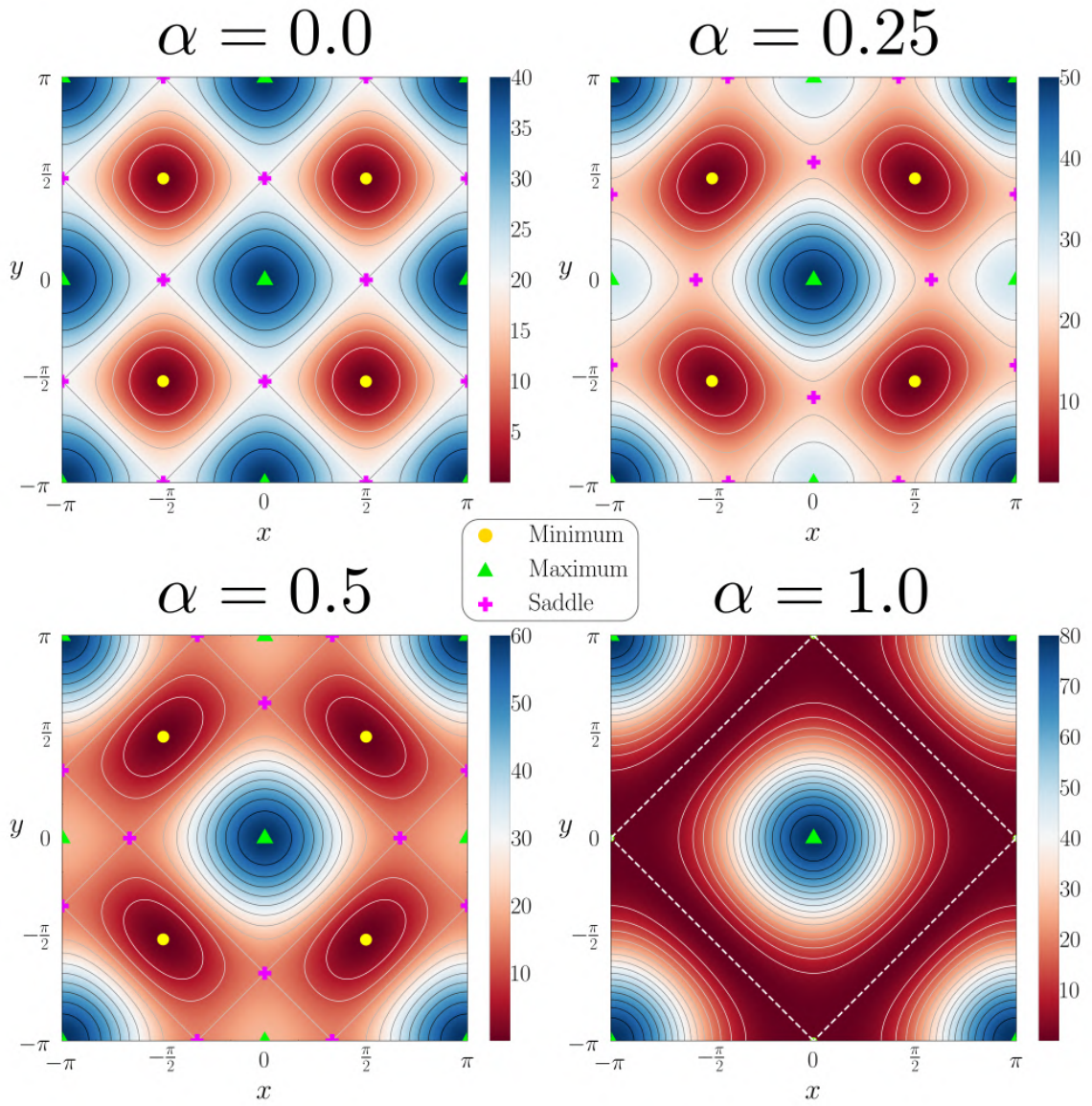

Figure 6: Color plot and equipotential curves for the unit cell of potential $V(x, y)$ for different couplings parameter α. Equilibrium points are marked as: minima (yellow circles), maxima (green triangles) and saddles (pink crosses).

A topographical view of the potential function, reduced to its unit cell ($(x, y) \in [-\pi, \pi) \times [-\pi, \pi)$), is shown in figure 6 for different values of coupling α. As α increases from 0 to 1, only the saddle points change position, moving towards the local maxima and eventually coalescing with them at $\alpha = 1$. At this point, the minimum of $V(x, y)$ becomes a 'trench' line given by $y_T(x) = \cos^{-1}(\pm\cos(x))$. Table 1 lists all the equilibrium points (x^*, y^*) in the unit cell along with their energy values $V(x^*, y^*)$. These points are relevant

to understand the dynamics as their stability indicates how local solutions may behave, and their energy values provide a reference for transitions in the system. For example, the saddle points energy level is the threshold between particles being trapped in oscillations around lattice pits or traveling to neighboring cells.

Equilibrium points	(x^*, y^*)	$V(x^*, y^*)$
Minima	$\left(\frac{\pi}{2}, \frac{\pi}{2}\right)$ $\left(-\frac{\pi}{2}, -\frac{\pi}{2}\right)$ $\left(\frac{\pi}{2}, -\frac{\pi}{2}\right)$ $\left(-\frac{\pi}{2}, \frac{\pi}{2}\right)$	0
Maxima (global)	$(0, 0)$ (π, π)	$2U(1+\alpha)$
Maxima (local)	$(\pi, 0)$ $(0, \pi)$	$2U(1-\alpha)$
Saddle	$(0, \pm\cos^{-1}(-\alpha))$ $(\pm\cos^{-1}(-\alpha), 0)$ $(\pi, \pm\cos^{-1}(\alpha))$ $(\pm\cos^{-1}(\alpha), \pi)$	$U(1-\alpha^2)$

Table 1: Equilibrium points position (x^*, y^*), *i.e.* points where $\nabla V(x^*, y^*) = 0$, and their energy value $V(x^*, y^*)$ within a unit cell of the lattice potential; positions are taken modulo 2π. At $\alpha = 1$, saddle points merge with local maxima and form minimum trench lines given by $\cos(y_t(x)) = -\cos(x)$.

As can be seen from equation 2.9 and figure 6, the potential is invariant under spatial reflections ($x \to -x$ or $y \to -y$), translations $(x, y) \to (x + n\pi, y + m\pi)$, for $n, m \in \mathbb{Z}$, and rotations of $\frac{\pi}{2}$: $(x, y) \to (\pm y, \mp x)$. Moreover, the lattice presents a square symmetry, in the sense that it is possible to define a unit cell as the region $(x, y) \in [-\pi, \pi] \times [-\pi, \pi]$, thus allowing periodic boundary conditions, which simplifies simulations of trajectories.

2.3 Hexagonal lattice

Analogous to the construction of the square lattice, where two waves provided two symmetry axes, the hexagonal lattice is built with a triple of co-planar waves (fig. 7). For simplicity, the amplitudes $|\vec{k}_i| = k$ and angular spacing between the $\vec{k}_i$ directions will be taken as $\delta\theta_k = \frac{\pi}{3}$, such that the wave-vectors are written as

$$\vec{k}_i = k\cos\left(i\frac{\pi}{3}\right)\hat{x} + k\sin\left(i\frac{\pi}{3}\right)\hat{y}. \tag{2.10}$$

From equation 2.5, the resulting potential is

$$\begin{aligned} V(x,y) = U'\Bigg(&\cos^2(kx) + \cos^2\left(\frac{k}{2}x + \frac{\sqrt{3}k}{2}y\right) + \cos^2\left(-\frac{k}{2}x + \frac{\sqrt{3}k}{2}y\right) \\ &+ 2\alpha_{12}\cos(kx)\cos\left(\frac{k}{2}x + \frac{\sqrt{3}k}{2}y\right) + 2\alpha_{13}\cos(kx)\cos\left(-\frac{k}{2}x + \frac{\sqrt{3}k}{2}y\right) \\ &+ 2\alpha_{23}\cos\left(\frac{k}{2}x + \frac{\sqrt{3}k}{2}y\right)\cos\left(-\frac{k}{2}x + \frac{\sqrt{3}k}{2}y\right)\Bigg). \end{aligned} \tag{2.11}$$

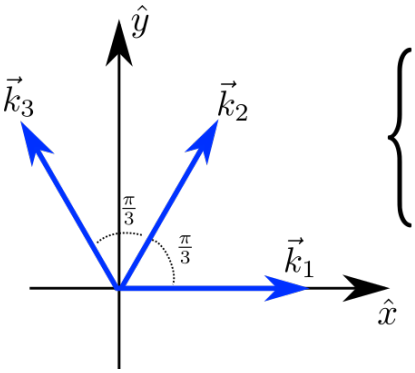

$$\begin{cases} \vec{k}_1 = k\hat{x} \\ \vec{k}_2 = \frac{k}{2}\left(\hat{x} + \sqrt{3}\hat{y}\right) \\ \vec{k}_3 = \frac{k}{2}\left(-\hat{x} + \sqrt{3}\hat{y}\right) \end{cases}$$

Figure 7: Schematic representation of the geometrical arrangement of the triple of wave-vectors that form the hexagonal lattice.

In the hexagonal lattice, the potential form 2.11 now presents three coupling coefficients α_{ij}, increasing the amount of control parameters to analyze. It is then convenient to reduce them. Figure 8 shows potential surfaces obtained for different values of α, notably for cases where the coupling value is the same for all wave pairs ($\alpha_{12} = \alpha_{13} = \alpha_{23} = \alpha$). For this condition, some equilibrium points alter their stability but still remaining at the same position, displaying its hexagonal symmetry and justifying the suggestive alternative name of honeycomb lattice. In this way, as α varies, the potential surface changes in a similar way to that seen for the square lattice, where points may change their energy, or stability, but not their position. Although restrictive and arbitrary, this simplification is justified by the parameter space reduction and the preservation of symmetry required for the purposes of this study, as will be made clear when discussing the island myriad phenomenon.

Nonetheless, although there is no algebraic restriction to the condition $\alpha_{ij} = \alpha$, it is important to validate if physically this choice is reasonable. Indeed, since the orientation of one wave-vector alters its coupling with all the other waves, the couplings α_{ij} constrain each other. It can be found that there is a limit to α in which the single coupling condition holds, and that is the interval $\alpha \in [-\frac{1}{2}, 1]$. Details on the calculation of this result are provided in appendix A.

Once the single coupling condition is assumed, and with the use of the identities

$$\cos(a+b)\cos(a-b) = \frac{1}{2}(\cos(2a) + \cos(2b)),$$

and

$$\cos^2(a+b) + \cos^2(a-b) = 1 + \cos(2a)\cos(2b),$$

the potential function is slightly condensed to the form

$$V(x,y,\alpha) = 1 + \cos\left(\sqrt{3}y\right)(\alpha + \cos(x)) + \cos(x)\left(4\alpha\cos\left(\frac{x}{2}\right)\cos\left(\frac{\sqrt{3}y}{2}\right) + \alpha + \cos(x)\right), \tag{2.12}$$

where, for simplicity, space was re-scaled ($x = kx', y = ky'$) and the energy scale set as $U' = 1$, without loss of generality. As before, the full dynamical model is given by the

Hamiltonian function

$$H = p_x^2 + p_y^2 + 1 + (\alpha + \cos(x))\cos\left(\sqrt{3}y\right) + \cos(x)\left(4\alpha\cos\left(\frac{x}{2}\right)\cos\left(\frac{\sqrt{3}y}{2}\right) + \alpha + \cos(x)\right), \tag{2.13}$$

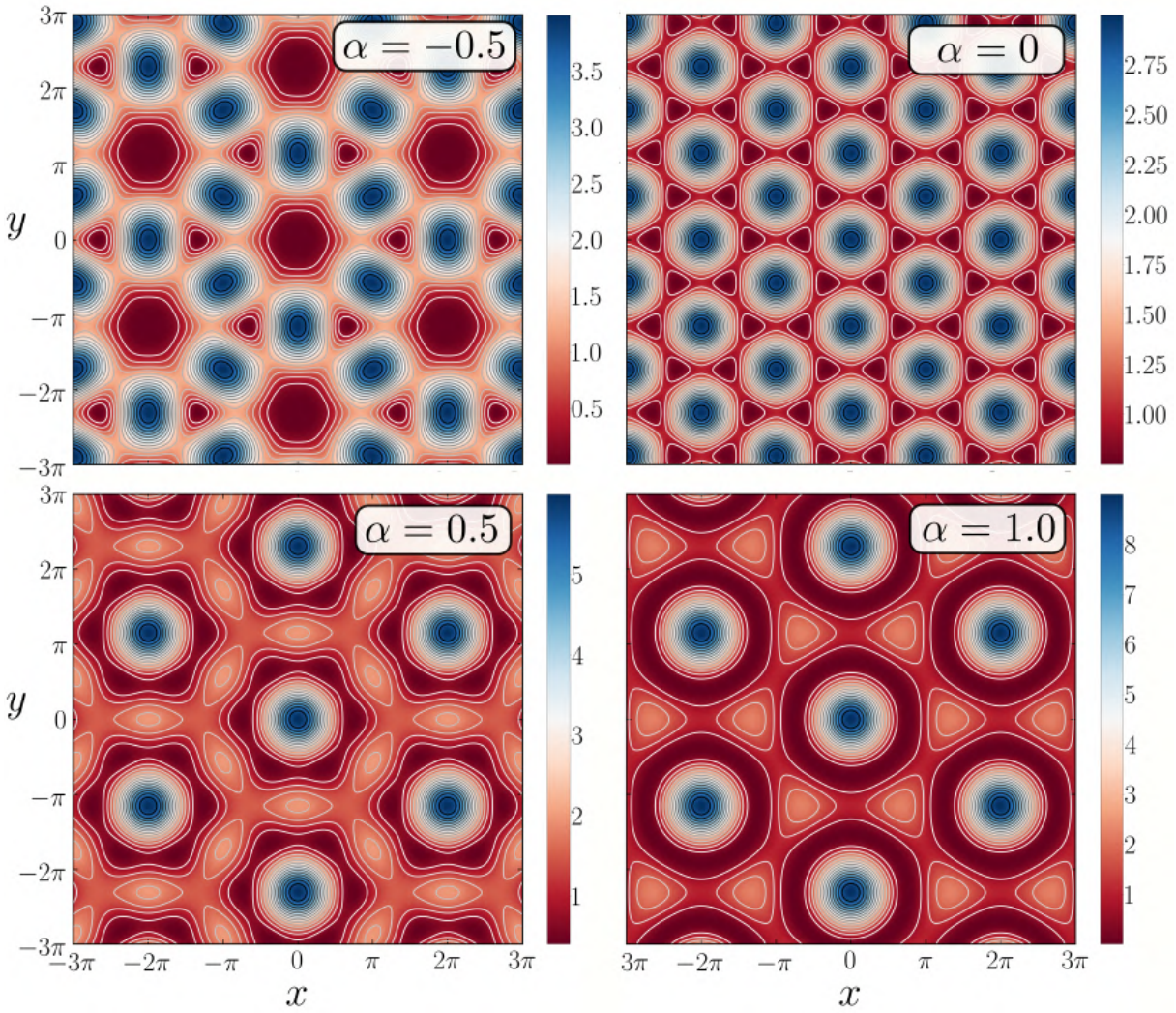

Figure 8: Topographic color map of the hexagonal lattice for different α values, inside the single parameter condition validity range $\alpha \in [-\frac{1}{2}, 1]$. For these figures $U = 1$.

For the determination of equilibrium positions, generically for free α_{ij} it is not trivial to find them analytically, and even with a single parameter, some of them are not easily obtainable. However, as aforementioned, the single parameter condition maintains symmetries that allow for the calculation with pure geometrical considerations on the potential surface. Some points with particular relevance for the analysis to be made here will be calculated in this way, as shown by the geometrical schematic in figure 9. In this schematic, distances are promptly obtained since the selected points are vertices of a regular hexagon, and other points belong to inner hexagons circumscribed to the outermost one that forms the unit cell of the honeycomb lattice. Besides, the six fold symmetry

guarantees that for any point found, any rotation of $\frac{\pi}{3}$ of its position will also be an equilibrium point of the same kind (*i.e.* same stability and energy).

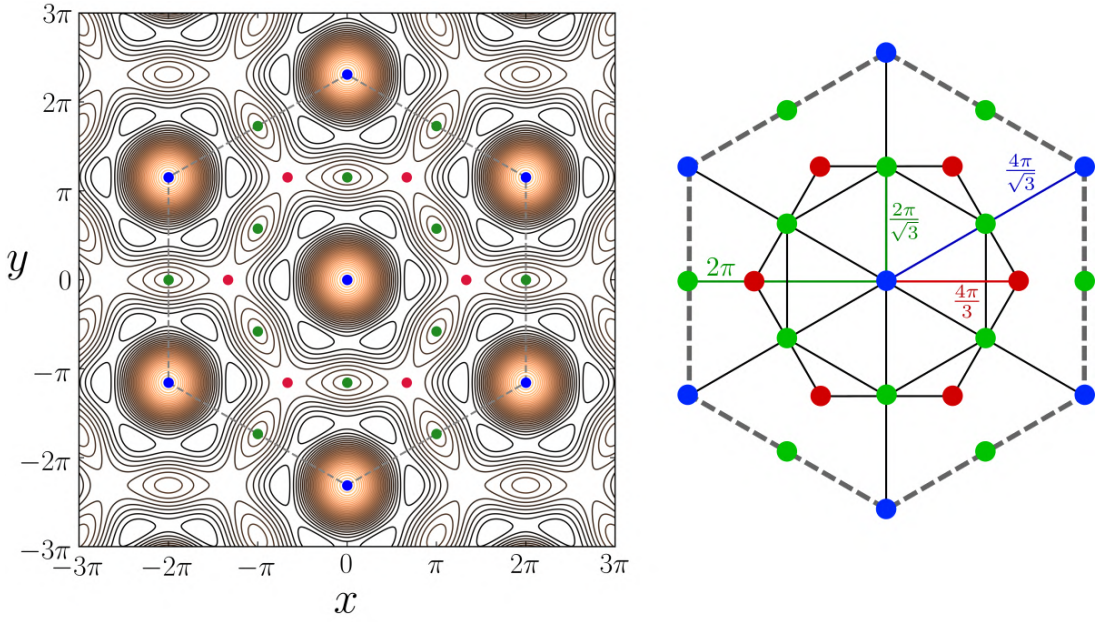

Figure 9: Geometric schematic used for equilibrium points calculation in the honeycomb lattice potential, assuming the single coupling condition. (Left) Equipotential lines (for $\alpha = 0.5$) and the selected equilibrium points. (Right) Schematization of the unit cell with the main hexagons and distances used for calculations. Equal colors indicate equal energy levels.

As summarized in table 2, the calculated points were divided in three color groups, each one made of points with same energy and stability, and arranged in accordance to its position. For reference, labels were organized as follows:

- P_p: unit cell vertices
- P_c: unit cell center
- L_o: unit cell edges (in-between P_p)
- L_i: midpoint between P_c and each P_p
- I: in-between P_c and each L_o

The two lattice topologies described here, the square and hexagonal ones, present an extra feature of symmetry that will be of interest. Both these forms and the triangle are the only regular polygons that allow for a complete and perfect tiling of the 2D space. That is, any one of these shapes can be duplicated infinitely to fill a plane with no gaps [34]. This extra periodicity condition not only allows for the use of periodic boundary conditions, but it gives rises to particular periodic solutions in the dynamical system, as will be discussed later in this work.

Eq. point	(x^*, y^*)	$V(x^*, y^*)$
• P_p	$(0, 0)$	$3\,(1 + 2\alpha)$
• P_c	$\frac{4\pi}{\sqrt{3}}\left(\cos\left(\frac{(2n+1)\pi}{6}\right), \sin\left(\frac{(2n+1)\pi}{6}\right)\right)$	$3\,(1 + 2\alpha)$
• L_i	$\frac{2\pi}{\sqrt{3}}\left(\cos\left(\frac{(2n+1)\pi}{6}\right), \sin\left(\frac{(2n+1)\pi}{6}\right)\right)$	$3 - 2\alpha$
• L_o	$2\pi\left(\cos\left(\frac{n\pi}{3}\right), \sin\left(\frac{n\pi}{3}\right)\right)$	$3 - 2\alpha$
• I	$\frac{4\pi}{3}\left(\cos\left(\frac{n\pi}{3}\right), \sin\left(\frac{n\pi}{3}\right)\right)$	$\frac{7}{4} + \frac{\alpha}{2}$

Table 2: Equilibrium positions (x^*, y^*) and their energy $V(x^*, y^*)$ for some reference points in the hexagonal unit cell (fig. 9). In the indexes above, $n = 0, 1, 2, 3, 4, 5$, with the periodic itentification $n = 6 \rightarrow n = 0$. Information on the labels is given in the text.

3

Methods

"Il peut arriver que des petites différences dans les conditions initiales en engendrent de très grandes dans les phénomènes finaux."
Poincaré, *La Science et l'Hypothèse* (1903)

For the execution of this theoretical work, we start by briefly introducing dynamical systems and how they are numerically evolved in time (sec. 3.1). Then, with initial focus on the spatial diffusion of particles throughout the square lattice, the diffusion calculation methodology is described (sec. 3.2). Once the main interest was to understand the system as its main parameters change, *i.e.* the coupling α and energy $E = H(t)$, a series of numerical methods for phase-space diagnostics are described in sections 3.3 to 3.5. The employed techniques are not only relevant for the particular investigation made here, but they have generic applicability to arbitrary conservative Hamiltonian systems, enabling automated analysis as the system parameters change 'continuously'. The motivation for the use of each one will be mentioned in the results chapter.

3.1 Dynamical systems and numerical integration

Generically, a dynamical system can be regarded as any set of equations, or rules, defining the evolution of the current state of a system, described by a set of variables $\vec{s} = (s_1, \dots, s_N)$, into a future state [35]. For continuous systems, this evolution is achieved in the form of differential equations

$$\dot{\vec{s}} = \vec{f}(\vec{s}, t) \implies \dot{s}_i = f_i(\vec{s}, t) \qquad \text{for } i \in [1, N], \tag{3.1}$$

with the dot denoting derivative in respect to the evolution variable, here exclusively set as the time t.

The dynamical system considered here belongs to the particular class of the conservative Hamiltonian ones, where the Hamiltonian function (H) itself is a constant along the time. In this case, states are represented by a vector $\vec{s} = (x,\ y,\ p_x,\ p_y)$ comprising the particle position $\vec{q} = (x, y)$ and its conjugate momenta $\vec{p} = (p_x, p_y)$. The system evolution (eq. 3.1) is then given by a vector field $\vec{f}$ from Hamilton's equations of motion

$$\vec{f}(\vec{s}) = \left(\frac{\partial H}{\partial p_x},\ \frac{\partial H}{\partial p_y},\ -\frac{\partial H}{\partial x},\ -\frac{\partial H}{\partial y} \right). \tag{3.2}$$

For the square lattice Hamiltonian (eq. 2.9), they yield

$$\dot{\vec{s}} = \vec{f}(\vec{s}) \quad \longrightarrow \quad \begin{cases} \dot{x} = 2p_x \\ \dot{y} = 2p_y \\ \dot{p}_x = 2U \sin(x) \left(\cos(x) + \alpha \cos(y)\right) \\ \dot{p}_y = 2U \sin(y) \left(\cos(y) + \alpha \cos(x)\right) \end{cases} \tag{3.3}$$

If one has knowledge of all possible solutions, for all the allowed initial conditions $\vec{s}_0 = \vec{s}(t = 0)$, then one has a complete description of a system dynamics. However, generally for

non-linear systems, solutions may not be easily obtainable due to cumbersome algebraic difficulties, or even impossible, due to the presence of chaos, where non-integrability makes it unfeasible to obtain solutions for arbitrary initial conditions and time intervals [36]. As for the square lattice model considered here, it will be integrable (fully solvable) only for $\alpha = 0$, case in which the system is reduced to two uncoupled pendula. In this case an analytical solution can be obtained via action-angle variables, as shown in appendix B. For any other $\alpha \neq 0$, the coupling term in the Hamiltonian acts as a perturbation and induces chaos in the system, as will be extensively shown along this work.

Nevertheless, in order to solve the motion equations (eqs. 3.3) and obtain trajectories for any given initial state, one can rely on numerical integration methods. A variety of such techniques are widely present in the literature and only the well-grounded Runge-Kutta (RK) family will be briefly described here, with no details on the error theory behind it [37]. Particularly, for all numerical integrations carried along this work, the Runge-Kutta-Cash-Karp (RKCK) variant was used [38].

In generic form, any RK method sequentially evolves (integrates) a state point by discretizing the equations of motion. Then, each time instant is advanced in discrete steps of δt in the following way

$$\vec{s}_{n+1} = \vec{s}_n + \delta t \sum_{i=1}^{m} b_i \vec{k}_i, \tag{3.4}$$

where m partial steps are taken for a single δt increment. Each partial step term $\vec{k}_i$ is evaluated by the vector field $\vec{f}$ at intermediary points as

$$\begin{aligned}
\vec{k}_1 &= \vec{f}(t_n, \vec{s}_n) \\
\vec{k}_2 &= \vec{f}(t_n + c_2 \delta t, \vec{s}_n + \delta t \; a_{21} \vec{k}_1) \\
&\vdots \\
\vec{k}_m &= \vec{f}(t_n + c_m \delta t, \vec{s}_n + \delta t (a_{m1} \vec{k}_1 + a_{m2} \vec{k}_2 + \cdots + a_{m,m-1} \vec{k}_{m-1})).
\end{aligned} \tag{3.5}$$

The coefficients b_i, c_i and a_{ij} are to be selected obeying the following relations:

$$\sum_{i=1}^{m} b_i = 1 \qquad \text{and} \qquad \sum_{j=1}^{i-1} a_{ij} = c_i \quad \text{for} \quad i = 2, ..., m. \tag{3.6}$$

Different RK methods consider different number m of partial steps (also referred to as integration order), thus requiring particular choices for the coefficients. The RKCK variant also includes an adaptive step-size control, increasing δt if the error committed in integration is small, or decreasing it if it is too large, requiring more precision. Figuratively, "many small steps should tiptoe through treacherous terrain, while a few great strides should speed through smooth uninteresting countryside" [37]. This feature allows

for great increase in CPU time performance. In RKCK method, the error is estimated as the difference between steps made in 5th and 4th order (thus considered a 5-4 order method), given by $e_{n+1} = |\vec{y}^{\,5\text{th}}_{n+1} - \vec{y}^{\,4\text{th}}_{n+1}| = |h\sum_{i=1}^{m}(b_i - b_i^*)\vec{k}_i|$. The coefficients for the RKCK method construction can be found in the original reference [38].

Despite the high accuracy of the RKCK method, as asserted by its energy deviation being smaller than order 10^{-9} (for total time $t = 10^3$), the method is not symplectic, thereby not preserving the symplectic area invariant. In view of that, an alternative symplectic algorithm, developed by Molei Tao [39], was considered for comparison with the RKCK, as described in appendix C. Briefly, with Tao's method, although conserving symplectic area up to order 10^{-7} (for integrable orbits), energy conservation is only of order 10^{-7}. This indicates that RKCK can provide good statistical results, keeping trajectory ensembles in a narrower energy interval, thus requiring a more careful use only when particular analyses depend on the symplectic property. Moreover, the CPU time efficiency for RKCK, given its adaptive control of step size, was more than 20 times faster than Tao's method, regarding the implementations available.

Once trajectories are numerically obtained, their four dimensional structure requires the use of Poincaré surface sections (PSS) for visualization. This surface will define a map for the crossings of an orbit with a given section Σ in phase-space, mapping one intersection point into the next (fig. 10). For all phase-space portraits presented along this work, we built a PSS map $T : \Sigma \to \Sigma : (x(t_i), p_x(t_i)) \to (x(t_{i+1}), p_x(t_{i+1}))$ by marking the x and p_x coordinates whenever the plane $y = \frac{\pi}{2}$ is crossed in the positive y direction, that is, if $p_y > 0$, ensuring the surface orientation.

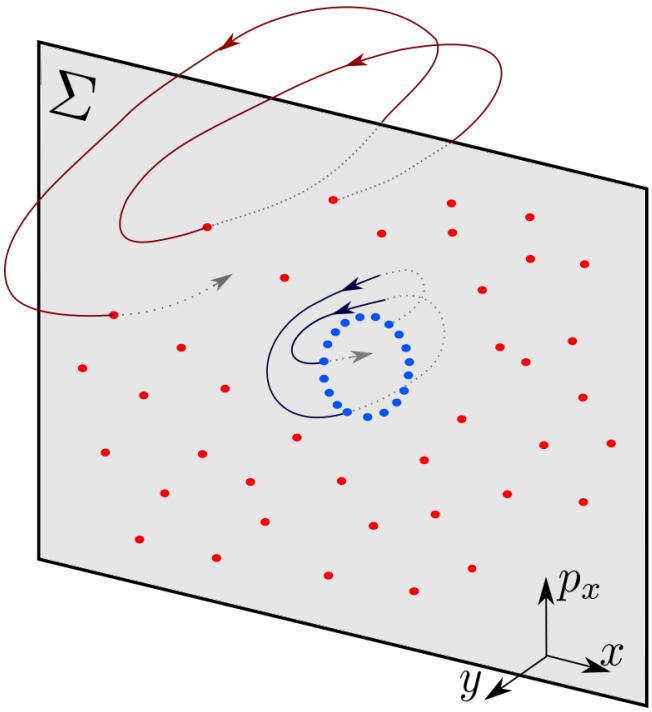

Figure 10: Representation of a Poincaré Surface Section (PSS). The intersection points between an orbit and the oriented surface Σ for $y = \text{const}$, define a 2D map T on the plane (x, p_x). Red dots correspond to a chaotic orbit, densely filling a 2D area, whereas blue dots represent a regular (non-periodic) orbit, densely filling an invariant curve.

In general for area-preserving dynamical systems (thereby including conservative Hamiltonians), Liouville's theorem implies the nonexistence of sources (repellers) or sinks (attractors) points. Consequently, trajectories in phase-space can be thought as forming an incompressible fluid, where any given volume can change its shape regarding that its inner volume remains constant [40]. Furthermore, the Liouville-Arnold theorem on integrability states that for any N-degrees-of-freedom system, there may be at most N independent functions F_i that are constants of motion [1]. When the N functions exist, the system is integrable and its orbits are restrained to an invariant torus of dimension N (or to any homeomorphic form) for each set of values of $(F_1, ..., F_N)$. These theorems will not be demonstrated here but they provide the arguments on why, in our 4-dimensional model, regular orbits appear as lines in a PSS whereas chaotic orbits densely fill an area, since in the latter case at least one of the F_i are not constant, thus not constraining the orbit to surfaces where $F_i = \text{const}$ (fig. 10).

3.2 Diffusion

In order to evaluate the spatial diffusion of particles throughout the lattice, an ensemble of them is evolved for long periods of time and we compute the 'scattering' of each one as the displacement $R_i(t)$ from its initial position (x_0, y_0)

$$R_i(t) = \sqrt{(x_i(t) - x_{0,i})^2 + (y_i(t) - y_{0,i})^2}. \tag{3.7}$$

The global dispersion then is evaluated as the average $\langle R_i(t) \rangle$ over particles in the ensemble. One may note that for this calculation the periodic boundary conditions over the unit cell are ignored, allowing particles to travel freely in the lattice. Classical diffusion theory [15] thus indicates that for long times, the average displacement asymptotically follows a power law

$$\langle R^2 \rangle \propto t^{\mu}. \tag{3.8}$$

The parameter μ in equation 3.8, named as diffusion exponent, provides a quantitative measure of how fast and far particles travel through the lattice. Fitting $\langle R^2 \rangle(t)$ as a function of time, for a given ensemble and a series of fixed pairs of energy and coupling, numerically yields the diffusion exponent μ as a function of the control parameters (E, α). The value of μ may indicate if the diffusion regime is normal ($\mu = 1$), as in the case of brownian motion or the classical random walk; free, or ballistic ($\mu = 2$), as in the case of free particles; anomalous ($1 < \mu < 2$) or sub-diffusive ($\mu < 1$). Superdifusivity ($\mu > 2$) is not possible in the system considered here due to its conservative nature and the lower boundedness for the potential function, preventing the kinetic energy to increase beyond

[1] By independent it is meant that their Poisson bracket is $\{F_i, F_j\} = \sum_k^N \left(\frac{\partial F_i}{\partial q_k} \frac{\partial F_j}{\partial p_k} - \frac{\partial F_i}{\partial p_k} \frac{\partial F_j}{\partial q_k} \right) = 0$.

the upper limit $|\vec{p}| \leq \sqrt{2mE}$.

It is worth mentioning that the ensemble of particles, here modeled as a high number of initial conditions, is generated for constant energy and coupling, which remain fixed in time. Besides, in order for diffusion to occur in the system, we must have $E > V_{\text{saddle}}$, providing enough kinetic energy for particles to surpass the saddle points between lattice pits. Moreover, since $V_{\text{saddle}} = U\,(1 - \alpha^2)$, the higher the value of α (closer to 1) the lower is the energy for diffusion onset.

For the creation of an ensemble with fixed energy that covers all phase-space, a Monte Carlo approach was used. In detail, for each particle, a position (x_0, y_0) is randomly generated in the space domain $[0, \pi] \times [0, \pi]$ around a lattice minimum. If the position satisfies the energy constraint $E > V(x_0, y_0)$, then the momentum vector $\vec{p} = (p_{x,0}, p_{y,0})$ is calculated directly from the energy equation

$$|\vec{p}| = \sqrt{p_{0,x}^2 + p_{0,y}^2} = \sqrt{E - V(x_0, y_0)}, \tag{3.9}$$

with its direction randomly generated by a uniformly distributed angle $\theta \in [0, 2\pi)$. An example of the resulting set of initial points can be seen in figure 11.

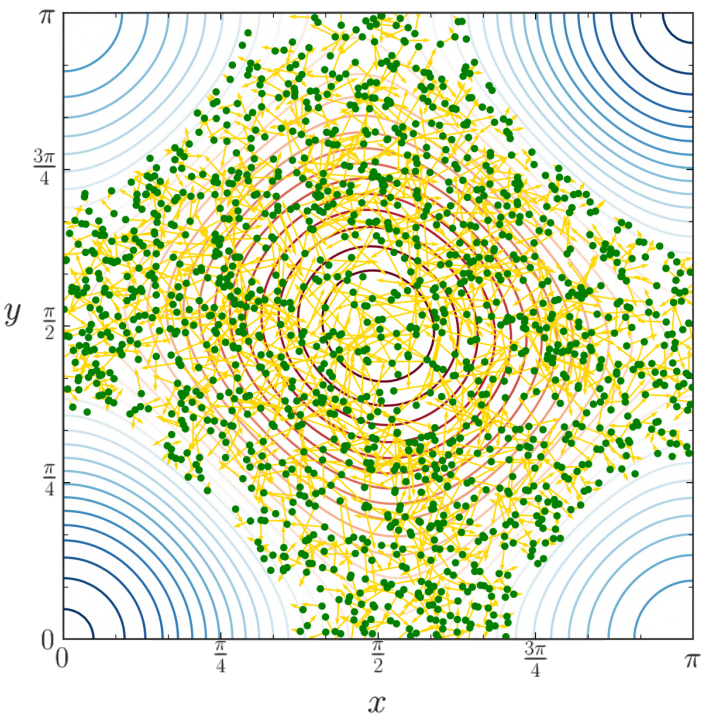

Figure 11: Ensemble of initial condition space distribution for diffusion calculation. Each green point is a random position (x_0, y_0) in an allowed region where $V(x_0, y_0) < E$. The momentum vectors, shown as yellow arrows, have modulus $|\vec{p}| = \sqrt{p_x^2 + p_y^2} = \sqrt{E - V(x_0, y_0)}$ and direction given by an angle randomly generated in $\theta \in [0, 2\pi)$.

For this work, a total of $N = 2 \times 10^4$ particles were used and all evolved for a total time of $t = 3 \times 10^3$. It is important to mention that the average used for the diffusion exponent fitting (eq. 3.8) is taken over phase-spaces that often present simultaneously regular and chaotic behavior. This may be out of the original scope of brownian diffusion, which commonly considers only chaotic movement, but still provides an indirect measure of how much particles spread throughout the lattice. Moreover, the presence of regular orbits

with high diffusivity (ballistic) may alter the global average, even with chaotic regions in a slower diffusion regime. Therewith, smaller amounts of particles and shorter integration times were tested in order to check how much statistical fluctuation the calculation may present, as will be discussed further in the results chapter.

3.3 Periodic orbits and monodromy theory

Amidst all the infinite solutions to the motion equations, the set of periodic orbits (PO) is of special importance. Formally, these are orbits that after some time $t = \tau$ return to a previous state, such that: $\vec{s}(t, \vec{s}_0) = \vec{s}(t + \tau, \vec{s}_0)$. Given that POs are closed curves in the 4D space, it is helpful to picture them from a Poincaré map framework. In the intersection surface Σ, POs correspond to fixed points of the PSS map (or of its m-th iterate), *i.e.* for the map $T^m : \Sigma \to \Sigma$, evolving one crossing of the PO with Σ into its next one, any fixed point $P^* = (x^*, p_x^*)$ would satisfy: $T^m P^* = P^*$, with m as the number of map iterations (map period). Visually in the PSS, POs appear neither as densely filled lines nor densely filled areas, but as m discrete points.

These fixed points present stability depending whether small displacements $\delta\vec{s}$ from P^* remain close to it, if the point is stable, or diverge from it exponentially, if it is unstable. Consequently, stable fixed points correspond to the center of stability islands in a PSS whereas unstable ones are immerged in chaotic regions [36]. As will be detailed in section 3.4 on manifolds, the unstable fixed points mold the dynamics within chaotic regions.

In order to numerically find POs and their stability, one can rely on monodromy theory. Its core concept is resumed from its etymology, as quoted from M. Baranger *et al.* [41]: "'monodromy' can be loosely translated as 'Once-around-the-trajectory', from the Greek *μονος*, meaning *one* or *single*, and *δρομος*, meaning *racecourse*". In practice, for small displacements $\delta\vec{s}$ around a given PO point, after one period τ its deviation will be linearly given by the so-called monodromy matrix [42]:

$$\delta\vec{s}(\tau) = \mathbf{M}\, \delta\vec{s}(0). \tag{3.10}$$

The evaluation of $\mathbf{M}$ will be described further in this chapter, but for now we anticipate without proof some of its main properties. The monodromy $\mathbf{M}$ is a $2n$-order square matrix, with n as the number of degrees of freedom of the system. It obeys the symplectic relation

$$\mathbf{M}^T \mathbf{J} \mathbf{M} = \mathbf{J}, \quad \text{with} \quad \mathbf{J} = \begin{pmatrix} \mathbf{0}_n & \mathbf{I}_n \\ -\mathbf{I}_n & \mathbf{0}_n \end{pmatrix}, \tag{3.11}$$

and $\mathbf{I}_n$ as the n-th order identity matrix. This symplecticity implies that the $2n$ eigenvalues

of $\mathbf{M}$, ρ_i, will come in pairs of unitary product [43], that is

$$\begin{cases} \text{if} \quad \rho_i \in \mathbb{R} \implies \rho_i \leftrightarrow \frac{1}{\rho_i} \\ \text{if} \quad \rho_i \in \mathbb{C}\backslash\mathbb{R} \implies \rho_i \leftrightarrow \rho_i^* \quad \text{and} \quad ||\rho_i|| = 1. \end{cases} \tag{3.12}$$

Furthermore, the Floquet-Lyapunov theorem [44] connects the eigenvalues ρ_i with the critical exponents λ_i, as $\rho_i = e^{\lambda_i \tau}$, thus providing information on the PO's stability. For 4D systems, this connection allows the determination of stability directly from the trace of $\mathbf{M}$, without the need to compute eigenvalues. Firstly, one may notice that $\rho_i = \rho_i^{-1} = 1$ are two immediate eigenvalues of $\mathbf{M}$, since displacements of the orbit along its own direction will follow the orbit path and return precisely at the same point. Then, the two remaining eigenvalues yield different results for each stability scenario:

$$\begin{aligned} \text{Stable:} \quad & (\lambda = i\theta) \longrightarrow \text{tr}(\mathbf{M}) = 2 + e^{i\theta\tau} + e^{-i\theta\tau} = 2\left(1 + \cos(\theta\tau)\right) \in [0, 4] \\ \text{Unstable:} \quad & (\lambda = \theta) \longrightarrow \text{tr}(\mathbf{M}) = 2 \pm \left(e^{\theta\tau} + e^{-\theta\tau}\right) = 2\left(1 \pm \cosh(\theta\tau)\right) \in (-\infty, 0] \cup [4, \infty) \end{aligned}$$

with $\theta \in \mathbb{R}$. Therefore, stable orbits will have $\text{tr}(\mathbf{M}) \in (0, 4)$ whilst unstable ones will have any other value for $\text{tr}(\mathbf{M})$. Particular situations when bifurcations occur to higher order periodic orbits may present trace equal to 0 or 4.

The linear property in equation 3.10 motivated an algorithm for the numerical search of POs, as developed by Baranger [41] and further detailed by Simonovic [45]. Considering an n-degree of freedom Hamiltonian system, with separable kinetic and potential energies

$$H(\mathbf{q}, \mathbf{p}) = \sum_{i=1}^{n} \frac{p_i^2}{2m_i} + V(\mathbf{q}),$$

any numerical solution $\mathbf{s}(t)$ will be a set of points evaluated at discrete times $k\Delta t$, for $k \in [0, K]$ and total integration time $t = K\Delta t$:

$$\mathbf{s}(t_k) = \mathbf{s}_k = \left(q_{1,k},\ \cdots,\ q_{n,k},\ p_{1,k},\ \cdots,\ p_{n,k}\right).$$

When linearizing the equations of motions around a periodic solution, the k-th local displacement (or correction) $\delta\mathbf{s}_k$ will be locally written as

$$\delta\mathbf{s}_{k+1} = \mathbf{\Lambda}_{k+1}\delta\mathbf{s}_1 + \mathbf{\Gamma}_{k+1}, \tag{3.13}$$

where the matrix $\mathbf{\Lambda}_{k+1}$ and the vector $\mathbf{\Gamma}_{k+1}$ are cumulatively calculated as the orbit is followed as:

$$\begin{aligned} \mathbf{\Lambda}_{k+1} &= \mathbf{U}_k\mathbf{\Lambda}_k \qquad \text{with} \quad \mathbf{\Lambda}_0 = \mathbf{I}_{2n} \\ \mathbf{\Gamma}_{k+1} &= \mathbf{U}_k\mathbf{\Gamma}_k + \mathbf{c}_k \quad \text{with} \quad \mathbf{\Gamma}_0 = \mathbf{0}_{2n} \end{aligned}$$

for $\mathbf{U}_k$ and $\mathbf{c}_k$ given by

$$\mathbf{U}_k = \begin{pmatrix} \mathbf{I}_n & \Delta t\ \mathbf{Q} \\ -\Delta t\ \mathbf{P}_{k+1} & \mathbf{I}_n - \Delta t^2 \mathbf{P}_{k+1}\mathbf{Q} \end{pmatrix}; \qquad \mathbf{c}_k = \begin{pmatrix} c'_{1,k} \\ \vdots \\ c'_{n,k} \\ -\Delta t \sum_i^n V_{1i}(\mathbf{q}^0_{k+1}) c'_{i,k} + c'_{n+1,k} \\ \vdots \\ -\Delta t \sum_i^n V_{ni}(\mathbf{q}^0_{k+1}) c'_{i,k} + c'_{2n,k} \end{pmatrix}.$$

The auxiliary quantities $\mathbf{Q}$, $\mathbf{P}_k$, $c'_{i,k}$ and $c'_{i+n,k}$ in turn are

$$\mathbf{Q} = \begin{pmatrix} m_1^{-1} & \cdots & 0 \\ \vdots & & \vdots \\ 0 & \cdots & m_n^{-1} \end{pmatrix},$$

$$\mathbf{P}_k = \begin{pmatrix} V_{11}(\mathbf{q}_k) & \cdots & V_{1n}(\mathbf{q}_k) \\ \vdots & \ddots & \vdots \\ V_{n1}(\mathbf{q}_k) & \cdots & V_{nn}(\mathbf{q}_k) \end{pmatrix} \qquad \text{for} \qquad V_{ij} = \frac{\partial^2 V(\mathbf{q})}{\partial q_i \partial q_j},$$

$$c'_{i,k} = q^0_{i,k} - q^0_{i,k+1} + \Delta t\ \frac{p^0_{i,k}}{m_k},$$

$$c'_{i+n,k} = p^0_{i,k} - p^0_{i,k+1} - \Delta t\ V_i(\mathbf{q}^0_{k+1}) \qquad \text{for} \qquad V_i = \frac{\partial V(\mathbf{q})}{\partial q_i} \qquad \text{and} \qquad i \in [1, n].$$

Variables (q_k, p_k) with superscript 0 correspond to the orbit $\mathbf{s}(t_k)$ points. At this moment, imposing the closure condition ($\delta\mathbf{s}_{K+1} = \delta\mathbf{s}_1$) into equation 3.13, in order to force a periodic solution, returns a linear system to calculate the corrections $\delta\mathbf{s}_i$:

$$(\mathbf{I}_{2n} - \mathbf{\Lambda}_{K+1})\, \delta\mathbf{s}_1 = \mathbf{\Gamma}_{K+1} \tag{3.14}$$

Therefore, the method algorithm consists in integrating an arbitrary initial condition until time τ; calculating $\mathbf{\Lambda}_{K+1}$ and $\mathbf{\Gamma}_{K+1}$ as the orbit evolves; solving the linear system 3.14 for corrections $\delta\mathbf{s}_i$; applying them for each orbit point; and re-submitting the corrected orbit to the same procedure iteratively until convergence is reached. Here convergence is evaluated as $||\mathbf{\Gamma}|| \to 0$, or in practice, when it gets smaller than a precision limit $||\mathbf{\Gamma}|| < \epsilon_\Gamma$.

The algorithm works similarly to a Newton-Raphson method, and, when converged, equation 3.14 becomes a discretized version of the monodromy equation 3.10, with $\mathbf{\Lambda}_{K+1}$ the numerically calculated monodromy matrix, from which stability is obtained from its trace.

As shown above, the algorithm can only converge to a PO with period equal to the initial one proposed, τ. However, it is common that one desires to find a PO for a given

fixed energy, letting the period be arbitrary. For this purpose, in addition to the orbit points, the time step Δt must also become a variable to be corrected and a new equation (the conservation of energy) is added into the linear system. The final system to be solved then is a modification of 3.13:

$$\left(\mathbf{I}_{2n} - \mathbf{\Lambda}_{K+1} + \frac{1}{\epsilon_0}\{\mathbf{\Delta}_{K+1}, \Theta\}\right)\delta\mathbf{s}_1 = \mathbf{\Gamma}_{K+1} + \frac{\eta}{\epsilon_0}\mathbf{\Delta}_{K+1}, \tag{3.15}$$

where the new parameters η and ϵ_0 are given by:

$$\eta = E_1 - \sum_{i=1}^{n}\frac{\left(p^0_{i,1}\right)^2}{2m_i} - V(\mathbf{q}^0_{3/2}) \qquad \text{and} \qquad \epsilon_0 = \sum_{i=1}^{n}\frac{p^0_{i,1}}{2m_i}V(\mathbf{q}^0_{3/2}), \tag{3.16}$$

calculated at the half step position

$$\mathbf{q}^0_{3/2} = \frac{\mathbf{q}^0_1 + \mathbf{q}^0_2}{2} = \mathbf{q}^0_1 + \frac{\Delta t_0}{2}\,\mathbf{Q}\,\mathbf{p}^0_1$$

and new vector $\mathbf{\Theta}$ given by:

$$\Theta = (\epsilon_1, \cdots, \epsilon_{2n}) \quad \longrightarrow \begin{cases} \epsilon_i = V_i(\mathbf{q}^0_{3/2}) \\ \epsilon_{i+n} = \frac{p^0_{i,1}}{m_i} + \frac{\Delta t}{2m_i}V_i(\mathbf{q}^0_{3/2}) \end{cases} \quad \text{for} \quad i = 1, ..., n$$

for $V_i \coloneqq \frac{\partial V}{\partial q_i}$. The new matrix $\mathbf{\Delta}_{K+1}$ is cumulatively calculated as:

$$\mathbf{\Delta}_{k+1} = \mathbf{U}_n\mathbf{\Delta}_k + \mathbf{d}_k \qquad \text{for} \qquad \mathbf{\Delta}_1 = \mathbf{0}_{2n}$$

and

$$\mathbf{d}_k = \begin{pmatrix} \frac{p^0_{1,k}}{m_1} \\ \vdots \\ \frac{p^0_{n,k}}{m_n} \\ -\Delta t\sum_i^n V_{1i}(\mathbf{q}^0_{k+1})\frac{p^0_{i,k}}{m_i} - V_1(\mathbf{q}^0_{k+1}) \\ \vdots \\ -\Delta t\sum_i^n V_{ni}(\mathbf{q}^0_{k+1})\frac{p^0_{i,k}}{m_i} - V_n(\mathbf{q}^0_{k+1}) \end{pmatrix}$$

The term in brackets $\{\mathbf{\Delta}_{K+1}, \Theta\}$ indicates a dyadic product, *i.e.* a matrix $\mathbf{D}$ with elements $D_{ij} = (\mathbf{\Delta}_{K+1})_i\Theta_j$. The system in equation 3.15 is now considered converged if both $|\eta|$ and $||\mathbf{\Gamma}_{K+1}||$ are null or smaller then the given precision thresholds $(\epsilon_\eta, \epsilon_\Gamma)$; usually set close to machine precision, around 10^{-12}.

With such an algorithm to search for periodic orbits at hand, one can visualize bifurcations as the system's main parameters E and α change. In general, for both parameters

variation, POs may bifurcate into more POs of the same period, into higher period POs or even change their stability. The latter is particularly relevant when stable orbits become unstable, for we have the onset of chaos around the new unstable point, whence we can also calculate its manifolds, since the monodromy matrix provides us the eigenvectors for the manifold's branches (as shown in the next section 3.4).

3.4 Manifolds

Despite its stereotypical random nature, chaotic behavior in conservative systems is established over a deterministic geometry given by the invariant manifolds. Since most of the phase-space analyses are made from Poincaré surface sections, they will be presented within this context.

For a given saddle fixed point p^* of a PSS map, although unstable, there are two particular directions in which particles tend to approach it [46]. Analogously, if one considers the reversed dynamics (from the inverse map), iterating orbits backwards in time, the unstable directions become approximative. Therewith, the particular set of points p that approach (leave) p^* will form an invariant set named stable (unstable) manifold [47]

$$\begin{aligned} W_s(p^*) &:= \{p \in \Sigma : T^n(p) \to p^*, \text{ as } n \to \infty\} \\ W_u(p^*) &:= \{p \in \Sigma : T^{-n}(p) \to p^*, \text{ as } n \to \infty\} \end{aligned} \tag{3.17}$$

where $W_s(p^*)$ ($W_u(p^*)$) is the label for the stable (unstable) manifold branch; as mentioned in section 3.3, T is the map for the successive crossings of an orbit with a PSS, and T^{-1} its reverse form.

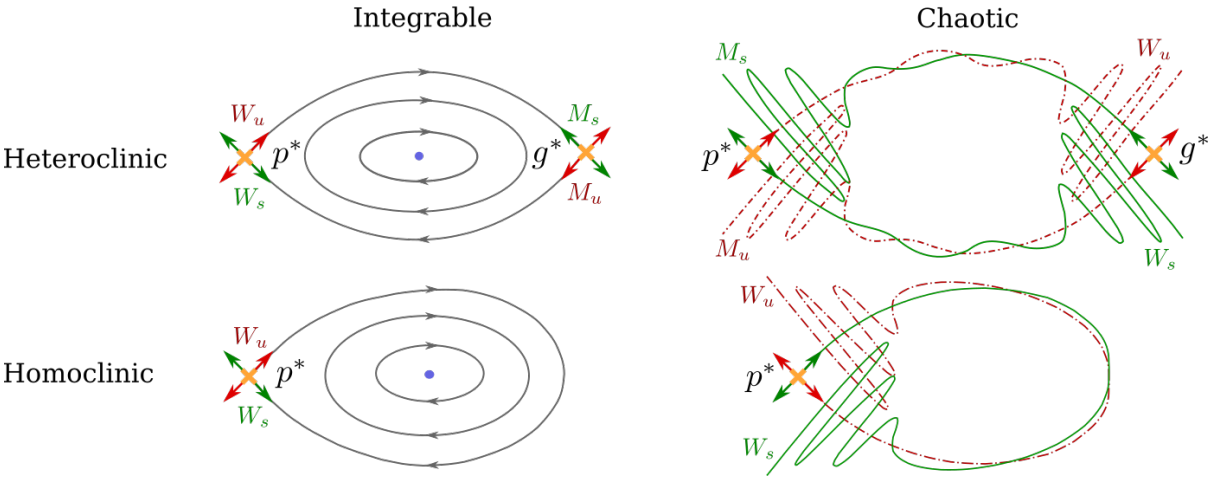

Figure 12: Homoclinic and heteroclinic manifolds for integrable and chaotic scenarios. (Top row) Heteroclinic connection, with invariant lines linking fixed points p^* to g^* (orange crosses). (Bottom row) Homoclinic connection, where the manifold branch loops back towards p^*. Figure adapted from [46].

When integrable, both manifold branches, stable and unstable, appear as invariant curves forming the contour (separatrix) of stability islands. When integrability is broken, these lines tangle with each other, giving rise to a chaotic layer. As illustrated in figure 12, this tangling mechanism, referred to as Smale horseshoe, is due to the crossing between unstable and stable manifolds, where any crossing point belongs simultaneously to both branches. Therefore, due to the uniqueness of orbits, this point shall be mapped into another intersection of the branches, forcing both curves to fold and intersect each other infinitely many times [36]. As the curves fold and tangle in a fractal way, they densely fill a finite-area of the map, destabilizing this region where nearby points are quickly separated due to the tangled geometry, giving rise to the fundamental chaotic property of sensitivity to initial conditions. Two scenarios are more commonly found for this phenomenon, one where branches can loop and connect back to p^* (homoclinic), or extend to a different unstable fixed point g^* (heteroclinic), as illustrated in figure 12.

The numerical calculation of such manifolds can be made from the monodromy matrix described in section 3.3. For an unstable fixed point $p^* = (x^*, p_x^*)$, the matrix $\mathbf{M}$ obtained from the periodic orbit related to p^* yields the eigenvectors that provide the linear approximate manifold branches directions (fig. 13).

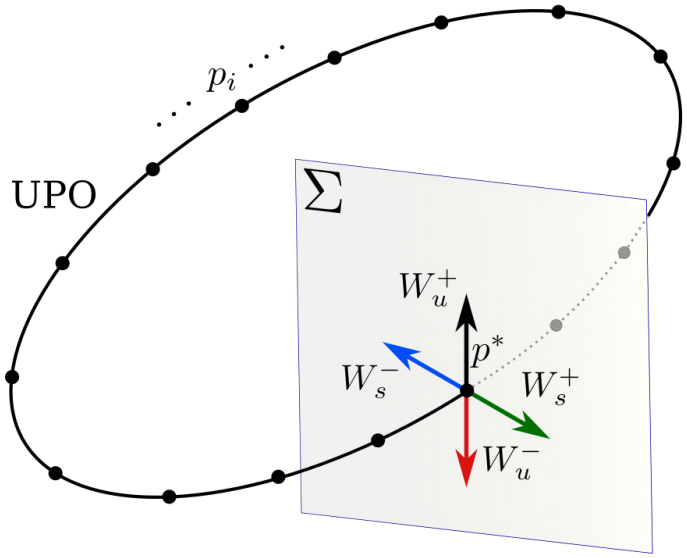

Figure 13: Manifold unstable $W_u^{\pm}(p^*)$ and stable $W_s^{\pm}(p^*)$ branches directions given by the monodromy eigenvectors. The plus and minus signs indicate that for each one, its opposite counterpart will also be an eigenvector. All vectors $W_{u,s}^{\pm}$ and the fixed point p^* are placed in the surface Σ, while the other UPO points p_i are in the 4D space.

Thus, setting a line of initial conditions close to p^* and along the eigenvector direction, the dynamical evolution of these points will follow the manifold (see fig. 14). Evolving these points in time and taking the intersections of this line with Σ reproduce the manifolds tangled structure and how it shapes the dynamics within a chaotic region.

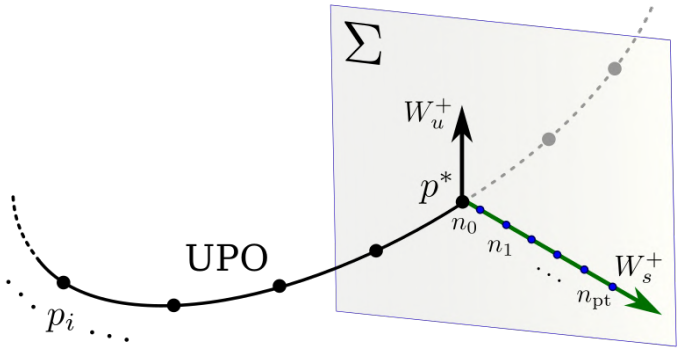

Figure 14: Initial points n_i set along an eigenvector direction (here shown for W_s^+) for manifold calculation. The points are placed along the line starting at p^* and following the eigenvector direction.

One may point out that for a 4D system, manifolds will be tubes in the 4D space, since each point of it acts as an unstable fixed point, as opposed to the 2D lines shown in figure 12. The curves shown in figure 12 are indeed the intersection of such tubes into the 2D PSS map. However, in some cases the crossing of the manifold tube with a PSS can happen to produce closed loops (if the tube is intersected transversely), as studied by Ozorio [48]. Although this behavior was not seen yet in this work, it is an important difference between Hamiltonian flows and pure 2D symplectic maps not oftenly mentioned.

3.5 Chaotic/Stable area calculation – SALI method

Whenever chaos emerges in a Hamiltonian system, it starts by appearing around unstable fixed points and separatrices, further eroding the invariant island and eventually spreading and forming a chaotic sea, possibly dominating the whole phase-space. Along this process, it is thus interesting to evaluate how much area or volume of phase-space is filled by chaos, therefore requiring a fast algorithm capable of numerically distinguishing between chaotic and regular orbits.

For this purpose, the Smaller Alignment Index (SALI) method can be used, as developed by G. Skokos [49]. Briefly, the core idea behind SALI is that, for a given orbit ϕ, small displacement vectors ω_1 and ω_2 will align to each other in case ϕ is chaotic while remaining at a finite angle if ϕ is stable. This method is valid for any finite-dimensional conservative dynamical system or symplectic map, and although it holds for an arbitray number of degrees of freedom, for simplicity it will be exposed here for the 2 degrees case.

In detail, given the initial point $\phi(0) = (x_0, y_0, p_{x0}, p_{y0})$, to determine whether ϕ is chaotic or regular, one can take two vectors slightly displaced from it, namely $\omega_1 = (dx_1, dy_1, dp_{x1}, dp_{y1})$ and $\omega_2 = (dx_2, dy_2, dp_{x2}, dp_{y2})$, and evolve them in time. The initial point $\phi(0)$ is evolved with the standard equations of motion, while ω_1 and ω_2 are calculated simultaneously with variation equations, *i.e.* they are evolved in tangent space as

$$\frac{d\omega_i}{dt} = D\mathbf{f}(\phi(t)) \cdot \omega_i \qquad \text{for} \quad i = 1, 2, \tag{3.18}$$

where $D\mathbf{f}(\phi(t))$ is the system's Jacobian matrix evaluated at the orbit point $\phi(t)$. These deviation vectors will then behave differently whether the orbit is chaotic or regular. When chaotic, the tangent space will be elongated along the unstable manifold direction, and compressed along the stable one, thereby aligning ω_1 and ω_2 to each other in a parallel or anti-parallel way (figure 15).

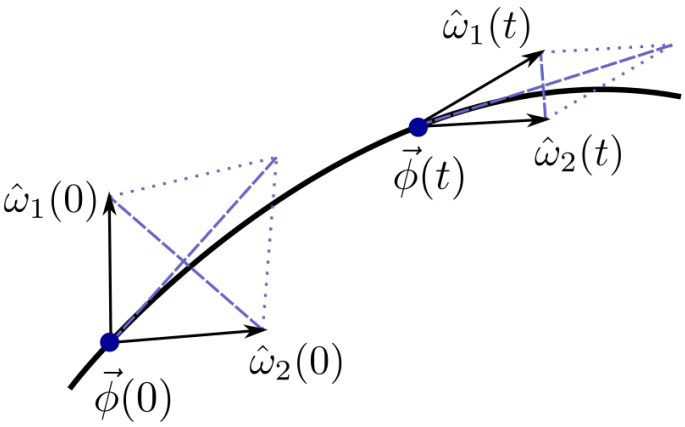

Figure 15: Diagram for the alignment of deviation vectors for a chaotic orbit from initial point $\phi(0)$ to a point $\phi(t)$. The parallelogram formed by the deviation unitary vectors $\hat{\omega}_{1,2}$ is flattened along the stable manifold direction and stretched in the unstable direction, making the vectors align (or anti-align) to each other. Figure adapted from [49].

On the other hand, in case $\phi(t)$ is a regular orbit, its movement is restrained to a torus, where the tangent space tends to keep angles limited. Consequently, the two deviation vectors will align to the tangent plane but not to each other, keeping a fixed angle between them (figure 16).

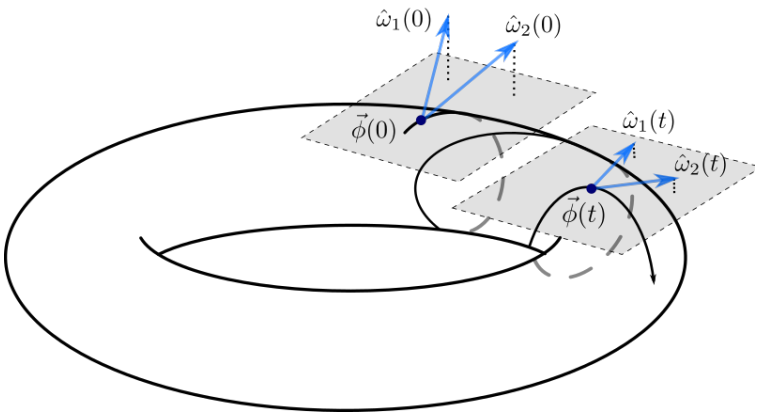

Figure 16: Diagram of an orbit over a stable torus from initial point $\phi(0)$ to a point $\phi(t)$. The gray semi-planes show the tangent space to ϕ and the unitary displaced vectors $\hat{\omega}_{1,2}$ moving towards it while keeping their angle limited (not aligned). Figure adapted from [49].

Therefore, any measurement of the vectors angle can be indicative of the stability of an orbit. Skokos then proposes the Smaller Alignment Index (SALI) as a quantity to evaluate the alignment between vectors ω_i, defined as:

$$\text{SALI}(t) := \min\left(\|\hat{\omega}_1 + \hat{\omega}_2\|, \|\hat{\omega}_1 - \hat{\omega}_2\|\right), \tag{3.19}$$

where the hat indicates normalized unitary vectors. Thus, in accordance to the above reasoning, in case of chaotic motion the ω_i vectors will become aligned parallel or anti-parallel, making $\text{SALI}(t) \to 0$ as $t \to \infty$, while keeping at a finite non-zero value for a regular one ($\text{SALI}(t) \in (0, \sqrt{2}]$).

It is important to point out that, due to shear between nearby torus layers, it is possible that even for regular orbits ω_1 and ω_2 still align, although this may occur for algebraically rather than exponentially times, much longer than the one required for the alignment of chaotic orbits. Besides, it is recommended to select orthogonal initial deviations, ensuring that SALI is not immediately null. In practical simulations, the convergence of SALI is ensured once it gets smaller than a precision threshold (*e.g.* 10^{-18}, the standard machine precision). Then, for an arbitrary orbit, one can evolve it for a sufficiently long time until the index drops below the threshold, case in which it is considered chaotic, or otherwise it is assumed to be regular.

Since only the direction of ω_i matters for the evaluation of SALI(t), the deviation vectors are normalized to $\hat{\omega}_{1,2}$ at regular time intervals, also preventing their divergence due to their exponential growth. As shown by Skokos in [50], the SALI index for chaotic orbits goes to zero exponentially, at a rate depending on λ_1 and λ_2, the two biggest Lyapunov exponents of the system: SALI(t) $\propto e^{-(\lambda_1-\lambda_2)t}$. Indeed, Lyapunov exponents themselves can be used as numerical indexes for the orbits stability, such as in the maximum Lyapunov exponent method (mLE), although usually requiring longer convergence times and therefore demanding a higher computational cost.

With such a tool at hand, one can mesh the phase-space in tiny cells (area tiles or volumetric cubes) and run the dynamics for an initial condition inside each one, whence all tiles (cubes) can be summed, providing an estimate for the chaotic/regular portion of area (volume) of phase-space. The estimate is as good as the smaller the size of the cell and number of initial conditions taken.

4

Results: Diffusion and Phase-space

"Prediction is very difficult, especially if it's about the future."
Niels Bohr

The square lattice system investigation was initiated with the measure of the spatial diffusion of particles and of how it changes as a function of the control parameters (sec. 4.1). Then, inspecting the chaotic area (sec. 4.2), a particular transition amidst all the sudden changes underwent by the diffusion exponent, namely that for $\alpha = 0.1$ and $E = 36$, is found to correlate with an island myriad phenomenon. This transition is further detailed by inspection of the system's phase-space (sec. 4.3) and its main periodic solutions (sec. 4.4).

4.1 Diffusion exponent

When looking at the diffusion exponent μ for varying parameters, *i.e.* the total energy ($E = H$) and lattice coupling (α), one expects variations due to the widening of channels between cells in the potential, as either α or E increases (as seen in sec. 2.2), and to changes in phase-space, due to bifurcations of orbits and emergence of chaos.

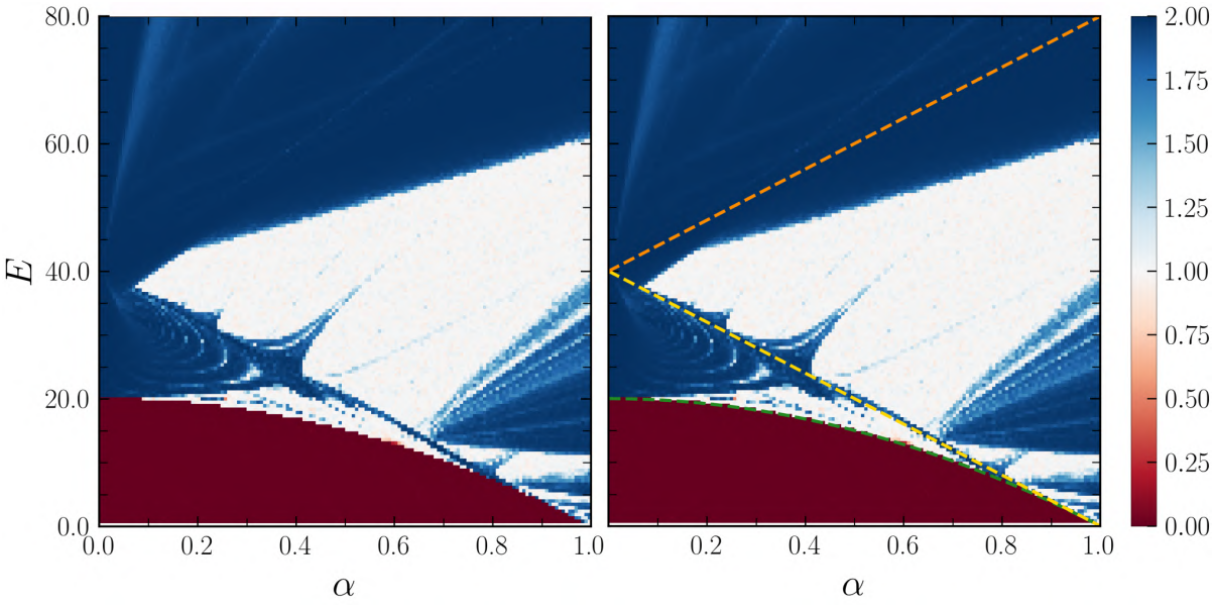

Figure 17: Diffusion exponent μ color map over the parameter space ($E \times \alpha$). The panel on the right displays the energy lines for equilibrium points: $V_{\text{saddle}} = U(1-\alpha^2)$ in green; $V_{\text{l-max}} = 2U(1-\alpha)$ in yellow and $V_{\text{g-max}} = 2U(1+\alpha)$ in orange. Grid size is 150×150.

In fact, the color map of μ in figure 17, calculated over the whole parameter space, presents a rather complex and intricate behavior. At first glance, one could expect the diffusion exponent to vary smoothly with E and α once the system's Hamiltonian is a smooth function of these parameters. Instead, it is found that diffusion regimes drastically and suddenly change in a non-trivial way, as shown by the complex shading from dark blue (free diffusion) to white shades (normal diffusion), along different regions of parameter space, either by varying E or α.

In the right frame of figure 17, the same portrait from the left is shown with the energy lines for equilibrium points highlighted. Saddle points, shown in green, correspond to the

diffusion onset threshold, where particles have enough energy to travel to neighboring lattice cells, thus presenting null exponent below it (red shaded area). The yellow and orange lines correspond to the local and global maxima energies, respectively; for them, while the global maxima line does not correlate with any particular structure in parameter space, the local maxima line superposes with a line with free diffusion regime, notably around $\alpha \in [0.4, 0.8]$.

Since energies above the local maxima line indicate that particles can surpass these points, one could expect diffusion to be predominantly free in this region. However, for energies above it, frequently a normal diffusion behavior is seen correlating with a diffusion suppression in the system. This apparently counter-intuitive aspect will be shown in the next sections to be related to peculiar bifurcations of stability islands in phase-space.

In general, despite the expected increase in transport with the increase of α, due to the pathway 'opening' between lattice cells as the local maxima energy diminishes, what is found is mixed behavior. As an example, one may note for $\alpha \in [0.1, 0.4]$ and $E \in [20, 35]$, in between the lines for saddle and local maxima, a rippled alternation between free and normal regimes; or around $\alpha \in [0.8, 1]$ and $E \in [10, 40]$, above the local maxima line, dark and light shades of blue over the whole range. Even for the highest energy regions, where free diffusion dominates, some fluctuations are seen to slightly slower diffusion rates. These of course occur due to changes in the dynamics, particularly to the coexistence of regular and chaotic orbits and how they are altered with the control parameters.

Figure 18 portrays some diffusion profiles lines, considering fixed values for α, from null perturbation ($\alpha = 0$), when the system is integrable, to low ($\alpha = 0.1$), medium ($\alpha = 0.5$) and maximum ($\alpha = 1.0$) coupling. When integrable, the system dynamics is reduced to two uncoupled pendula along x and y. In this case, above diffusion onset, a particle will travel along each axis direction unobstructed in almost straight trajectories through space, with no trapping of particles in lattice minima and thus keeping diffusion at free-regime (fig. 18 for $\alpha = 0$).

One may note no predominant sub-diffusion ($\mu < 1$) for any case of α, regardless of small fluctuations of μ around normal regime. This is an indication, although not a proof, that stickiness, *i.e.* the property of chaotic orbits to follow regular orbits for longer transient times, does not play a significant role in the system global dynamics. At least not for times as long as $t = 10^3$.

Despite the general fluctuations observed in μ, all cases of α present a free diffusion plateau for energies close to the potential's global maxima level. This is explained since in this case particles have a wider access to spatial regions where their velocity is not abruptly deviated due to the 'boundaries' where $V(x, y) = E$. The smoother deviations and a wider space for flights then allow for a higher diffusivity. Also, for energies above global maximum, unstable points in the lattice that could scatter orbits can be regarded as small perturbations, being less relevant as the higher the particle energy is.

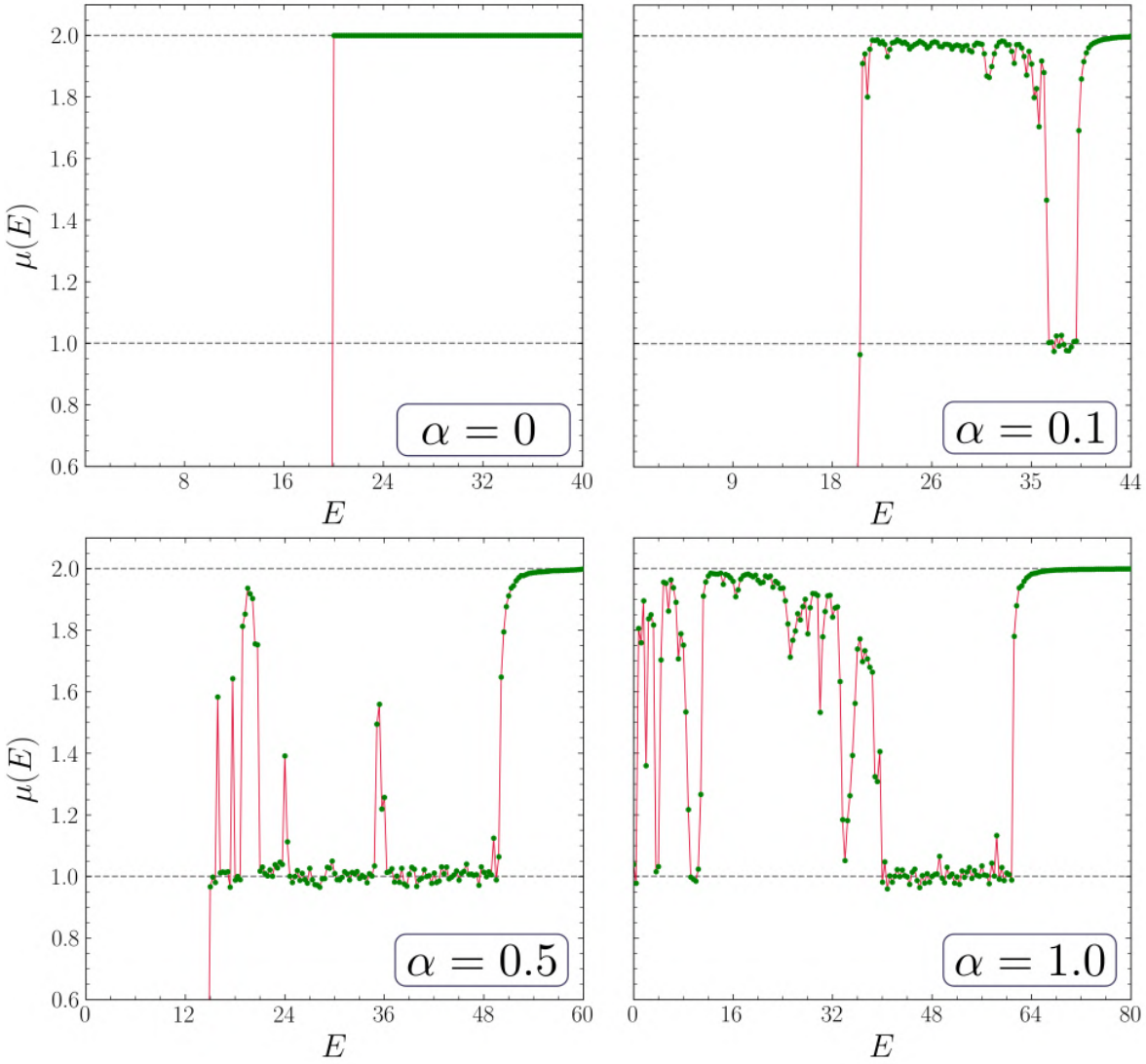

Figure 18: Diffusion exponent μ as a function of the energy E for different α. The dashed gray horizontal lines denote the normal diffusion ($\mu = 1$) and free diffusion ($\mu = 2$) limits.

In the presence of chaos, one could expect it to always suppress direct straight flights through the lattice and thereby to induce diffusion to be normal, as in a random walk. However, even chaotic orbits can present different spread behavior, being more restricted and keeping particles trapped for long times in lattice pits or allowing for longer straight displacements, the so-called Lévy flights, as illustrated in figure 19. It is interesting to note the range of displacements for each case, with flights summing up to thousands of cells, whereas in a random walk the particle journey is mostly restrained to only tens or hundreds of cells.

As described in section 3.2, the exponent $\mu(E, \alpha)$ was numerically obtained by fixing a pair (E, α) and calculating the average square displacement $\langle R^2(t) \rangle$ along the time over an ensemble of trajectories covering the whole available phase-space. For every parameter pair, an ensemble of $N = 2 \times 10^4$ points were used, each being integrated for a total time $t = 3 \times 10^3$. Since the power law behavior for $\langle R^2(t) \rangle$ stands for asymptotically

long times, the data fitting is made only on the last 25% of the time series. Lower times ($t = 10^2$) and particle number ($N = 10^4$) were also considered in order to check how sensitive the results are to statistical fluctuations, as shown in appendix D. Briefly, it was found that differences on μ did not exceed 10% for time or ensemble sizes of at least one order of magnitude lower than the ones used, indicating good statistical convergence for the values of t and N selected. Moreover, since long integration times are required, the diffusion profile for $\alpha = 0.1$ was also calculated with a symplectic integration method, where differences no greater than 15% were found, as shown in appendix E.

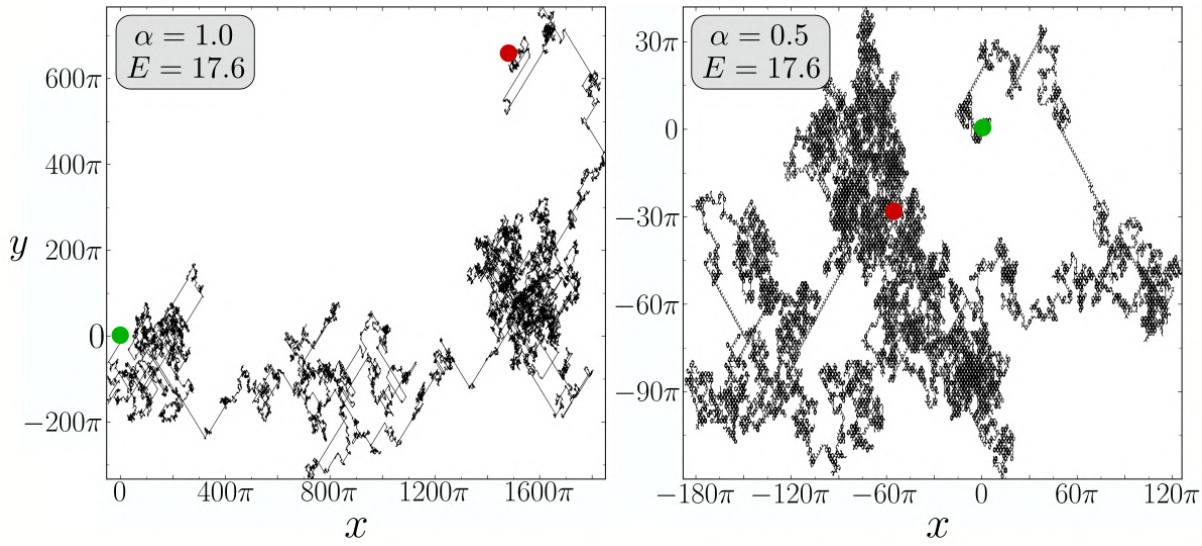

Figure 19: Chaotic trajectories with different spatial spread. (Left) Lévy flights with long displacements amidst short periods of restricted motion. (Right) Almost fully restricted motion. Green (red) dots mark the start (end) point of the trajectory. Integration time is $t = 10^5$.

For a deeper look into the diffusion transitions found, from now on a particular case will be brought into focus, namely that for coupling $\alpha = 0.1$ and energy $E = 36$, as shown in figure 18. In this case, as energy increases and surpasses the local maxima level at $E = 36$, diffusion undergoes a sudden drop from free to normal regime (fig. 20). As aforementioned, this behavior is rather unexpected since when particles have a wider space for transport, their diffusion is suppressed. The investigation procedure will rely on an analysis of how phase-space changes by inspecting it for energy values below, around and above transition. Other transitions unrelated to local maxima points will be briefly mentioned in section 4.2.

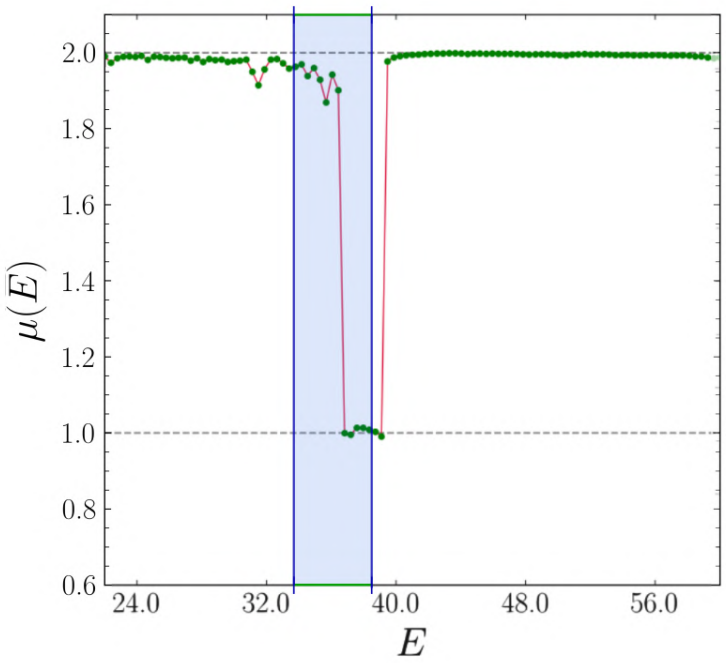

Figure 20: Diffusion exponent transition selected for analysis depicted inside the blue column region, for $\alpha = 0.1$ and energy around $E = 36$. As energy increases, diffusion undergoes a sudden drop from free ($\mu = 2$) to normal ($\mu = 1$) regime.

4.2 Chaotic area

In order to explore the diffusion transition selected, we first examined the portion of regular and chaotic solutions in phase-space. As described in section 3.5, the SALI algorithm allows one to mesh a phase-space area (here over the PSS Σ) and calculate the chaotic/regular areas by summing up over all grid cells. As a demonstration of this procedure, figure 21 shows how clear is the discrimination between chaotic (in black) and stable (in yellow) regions, with only thin layers of intermediate colors seen in between them.

It is worth mentioning that the calculated area is taken over phase-space, whereas the diffusion exponent μ is evaluated over orbits in position space. Thus, we compare two quantities regardless of their direct connection, expecting to see whether they correlate or not. Nevertheless, it is reasonable to expect some correlation since the emergence of chaotic orbits replacing trajectories composed of long flights through the lattice could be responsible for the diffusion suppression observed.

For the area calculation, as done for the diffusion exponent, a simulation is carried for each point on parameter space (E, α). Figure 22 shows the result as a color map for the chaotic area A, *i.e.* the fraction of the total area $A_{\text{total}} = A_{\text{chaos}} + A_{\text{regular}}$ that is chaotic. This normalization hides the fact that the total phase-space volume, and therefore the total transversal area of the PSS, grows with the energy, but nonetheless providing the desired information. To save CPU time, two features were used: first, all the crossings of an orbit with the grid were set with the same SALI value as its initial condition, thus avoiding the redundancy of calculating these crossings as new orbits, since they are

already known to be chaotic or regular; second, the integration of an orbit that achieves a cut SALI value of 10^{-12} is interrupted and considered chaotic, saving the extra time required to reach machine precision (10^{-18}).

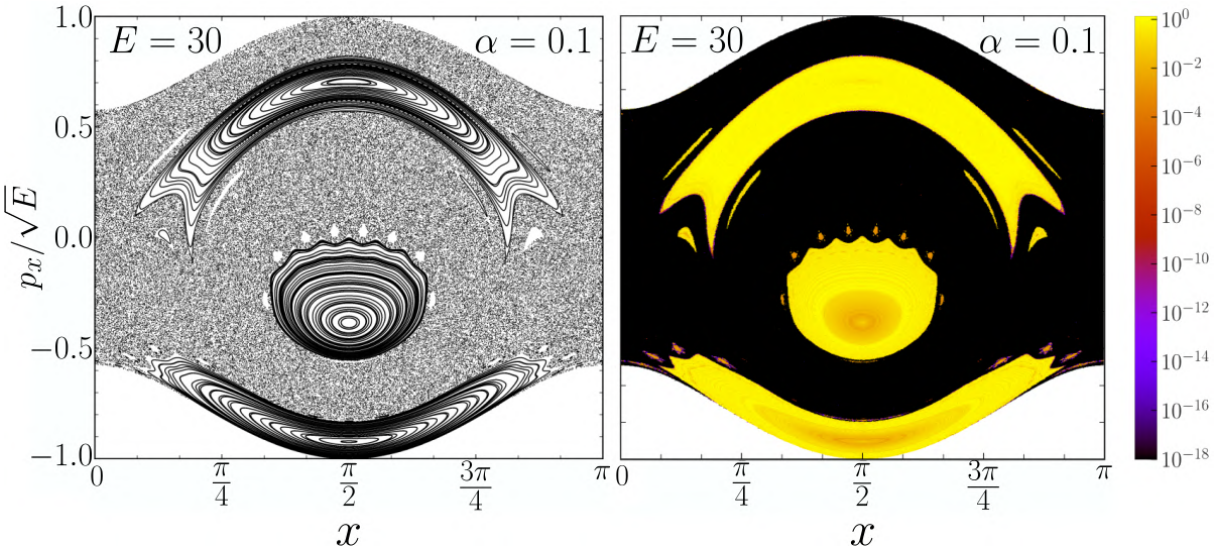

Figure 21: Example of SALI method application over a PSS for orbits discrimination. In the left panel, orbits intersections with the PSS Σ (black points). In the right panel, the color map with the SALI value for each grid cell (log scaled); in black (yellow), initial points for chaotic (stable) orbits. Grid resolution is $N_x \times N_{p_x} = 600 \times 1050$ and maximum integration time $t = 2 \times 10^3$.

Just as seen for the diffusion exponent (fig. 17), the chaotic area presents non-trivial, intricate fluctuations. Specifically, the energy lines displayed in the right panel now show that both the global and local maxima lines correlate with a clear white line, indicating the emergence of stability structures when these points are accessed. As will be extensively described in the following sections, this relates to the appearance of a multitude of islands in phase-space, associated to orbits approaching maxima equilibrium points, a phenomenon named here as island myriad bifurcation. The fact that these lines appear also for global maxima is due to the topological similarity when compared to local maxima.

Besides, the chaotic area color map (fig. 22) indicates that maxima energy lines are thresholds for an ergodic limit, that is, regions where chaos dominates the entirety of phase-space (shown as the dark region in between the green and yellow curves). Furthermore, system integrability is generally limited by the saddle energy line (in magenta), even though chaos appears for energies slightly below it, showing that it can emerge even without the access to unstable points directly. Also, integrability is seen for the $\alpha \to 0$ limit for arbitrary energies, as expected.

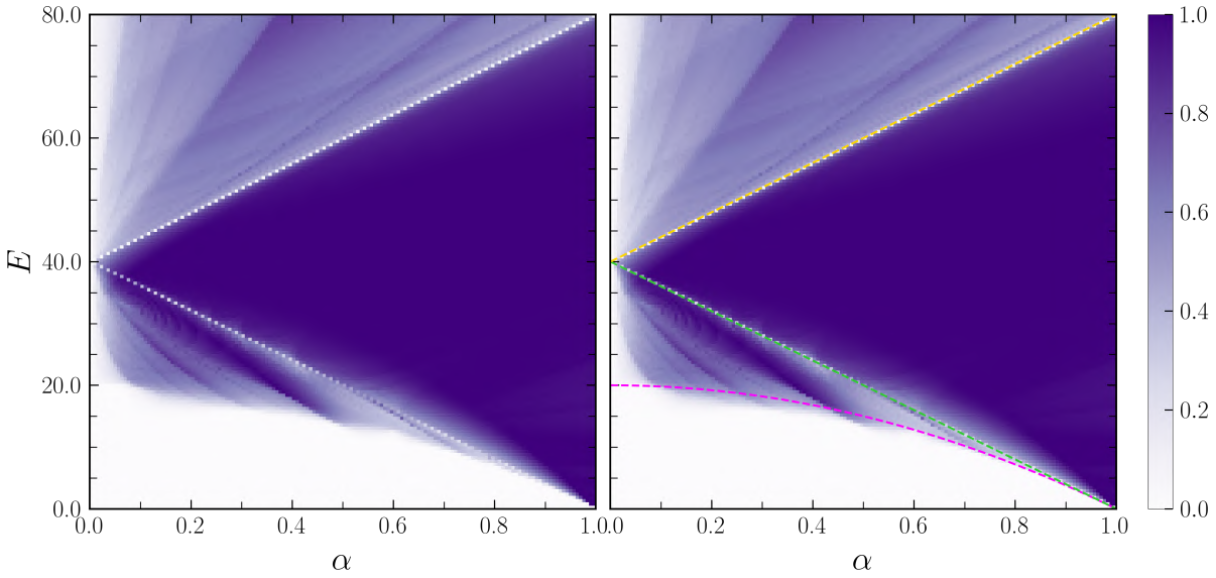

Figure 22: Color map of the chaotic area portion in parameter space. Total chaos is indicated by $A = 1$ and total regularity by $A = 0$. In the right frame, energy lines for equilibrium points are displayed as: $V_{\text{saddle}} = U(1-\alpha^2)$ in magenta; $V_{\text{l-max}} = 2U(1-\alpha)$ in green and $V_{\text{g-max}} = 2U(1+\alpha)$ in yellow. Grid size is 250×250.

Particularly within the ergodic region, a difference to the diffusion exponent diagram was found, where multiple diffusion fluctuations take place, whereas the chaotic area diagram does not present any whatsoever. As better detailed in appendix F, these diffusion fluctuations are more likely to be related to the appearance of small islands comprising orbits with long flights through the lattice, increasing the global diffusion exponent towards free regime but without altering the global phase-space structure.

Regarding the particular coupling value related to the transition selected previously, figure 23 shows the area profile for the case $\alpha = 0.1$. We firstly point out that even below diffusion onset at $E = 19.8$, despite the predominance of regular area, chaos is already noticeable, as seen from the growth in chaotic area starting at $E \approxeq 15$. The presence of this first chaotic layer will be detailed in section 4.4. With the diffusion onset follows an increase in chaos, as expected due to the saddle point effect on orbits, inducing instability in motion.

However, as observed for the diffusion transition of interest, where a suppression from free ($\mu \approxeq 2$) to normal regime ($\mu = 1$) takes place exactly at $E = 36$, one can notice a prominent sharp peak of decrease (increase) of chaotic (stable) area at this energy value. This indicates that a sudden appearance of stability structures marks the transition, as will be shown with portraits of phase-space displaying the previously mentioned myriad of islands (sec. 4.3).

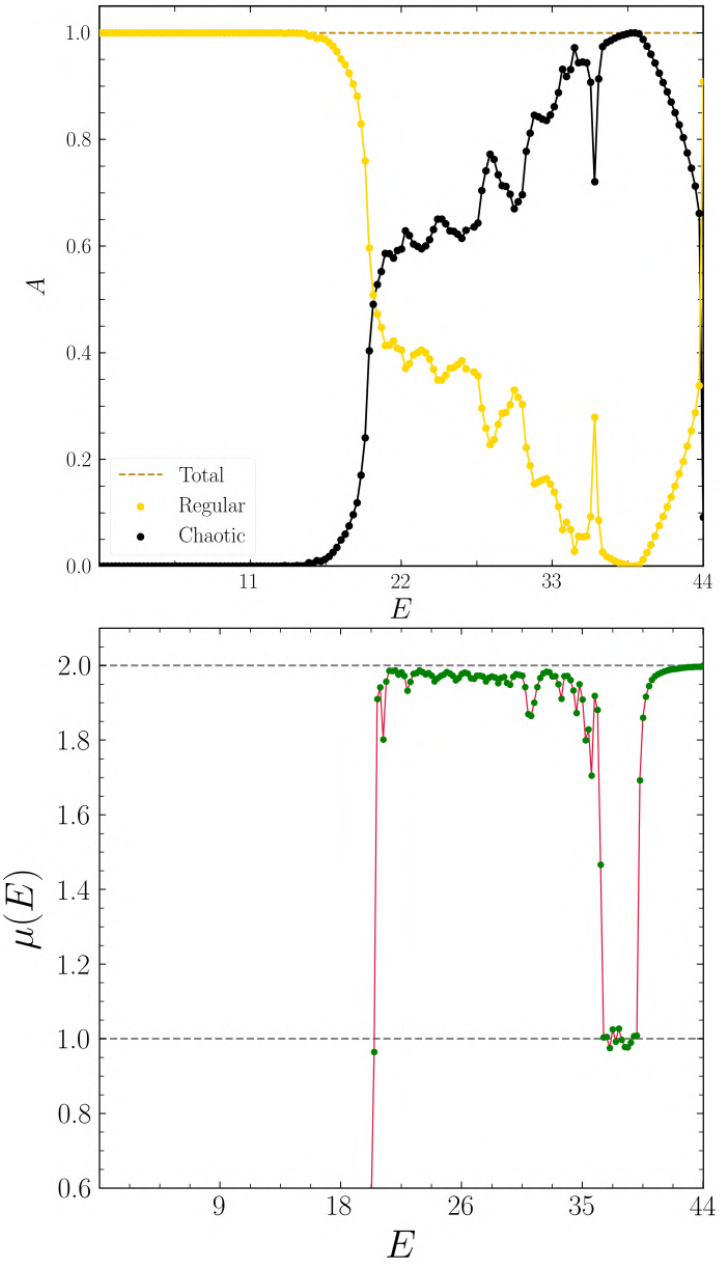

Figure 23: (Top) Normalized area ratios A of chaotic and regular orbits as a function of the energy E for $\alpha = 0.1$, calculated over the PSS Σ. Since A is normalized to total area ($A_{\text{total}} = A_{\text{chaos}} + A_{\text{regular}}$), the maximum value $A = 1.0$ is marked with a dashed yellow line. At each simulated point of E, a grid of 450×350 was used over the PSS, and the maximum running time was of $t = 2 \times 10^3$ time units. (Bottom) The selected diffusion profile for $\alpha = 0.1$ (fig. 20).

4.3 Phase-space

As anticipated, the diffusion transition selected for study is related to the increase of stability area associated to the appearance of a multitude of islands. Thus, we inspect the phase-space as the transition occurs by portraying it via the PSS Σ (sec. 3.1) for energy values below the transition ($E = 32$, where $\mu(E) \approxeq 2.0$), at transition ($E = 36.1$, where $\mu \approxeq 1.4$) and above it ($E = 38$, where $\mu = 1.0$).

In order to extract information from these portraits, three diagnostics were applied, they are the PSS map, an escape time color map and the manifolds. The PSS map simply shows the orbits intersections with the oriented section chosen at $y = \frac{\pi}{2}$; the escape time map colors a grid over the PSS corresponding to the time required for an initial condition to escape a given box limit. The escape box used was of ten neighbor cells, corresponding

to the square $\mathrm{Box}(n) = [-n\pi, (n+1)\pi] \times [-n\pi, (n+1)\pi]$ for $n = 10$. The maximum escape time allowed for particles was $t = 2 \times 10^2$, after which an orbit is considered to be trapped.

As described in chapter 3.4, manifolds can be calculated from a given unstable periodic orbit (UPO); here the one located along the stable direction of the saddle point at $(x_{\mathrm{sad}}, y_{\mathrm{sad}}) = (0, \arccos(-\alpha))$ was used (fig. 24). The fixed point related to it is located in the PSS Σ at $(x, p_x) = (0, 0)$.

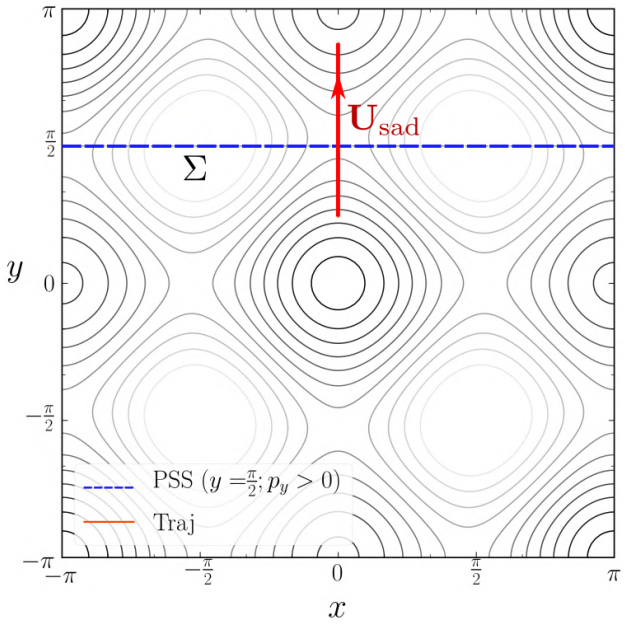

Figure 24: Unstable periodic orbit $\mathbf{U}_{\mathrm{sad}}$ used for manifold calculation along the stable direction of the saddle point located at $(x_{\mathrm{sad}}, y_{\mathrm{sad}}) = (0, \arccos(-\alpha))$. The dashed horizontal blue line indicates the Poincaré section used (Σ). Black solid lines are the equipotentials of $V(x, y)$ for $\alpha = 0.1$.

Therewith, figures 25, 26 and 27 show the phase-space portraits for the energy values selected: $E = 32$, $E = 36.1$ and $E = 38$, respectively. Below transition, when the system presents free diffusivity, the dynamics is divided into three main stability islands surrounded by a chaotic sea (fig. 25, top). One may note an immediate correspondence amidst the chaotic sea between the escape time color map and the manifold alone (fig. 25 center and bottom panels). This is a generic behavior for conservative systems and is explained by the fact that chaotic orbits will follow the stable manifold along time, approaching the saddle point and thus jumping from one lattice pit to another. The manifold's invariant lines thus indicate a route for chaotic orbits to escape cells and travel faster through the lattice.

For $E = 32$, a finger-like structure from the manifolds is found around the central and bottom islands. The low escape time (in black) in these islands is understood from the SPO at the center of each one, which are straight flights through lattice cells, as shown in figure 28. However, one may also note that these channels emanate from the islands boundaries, merging between the manifold finger-like structure, already within the chaotic sea.

When the transition occurs at $E = 36$, the two previous stability islands vanish and a myriad of large period chains of islands emerge from the chaotic sea (fig. 26, top panel),

giving rise to the aforementioned island myriad phenomenon. These structures last for a narrow interval of energy, approximately of $E \in [36, 36.3]$. The escape time for this case (fig. 26, center panel) reveals that all chains have even period, alternating between high escape time (in yellow) and low escape time (in purple). Figure 29 shows an example of a period 3 orbit from the myriad (orbit 1) and the particular orbit connecting two local maxima (orbit 2). Differently from the chains SPOs, the latter is unstable and its fixed point forms the center of the island myriad structure, around which all chains are concentric. The second part of this chapter will be dedicated to more details on this phenomenon.

The stable manifold from $\mathbf{U}_{\text{sad}}$ in its turn shows a web-like structure folding between the myriad chains (fig. 26, bottom panel), well showing that movement becomes more restrained, as confirmed by the reddish tones in the chaotic region seen in the escape time panel. Also, a great portion of orbits with higher escape time are concentrated around the upper stability island, which presents its own set of islands around itself.

When diffusion is suppressed to normal regime ($\mu = 1$), the myriad of islands completely vanishes and the phase-space becomes mostly chaotic, with only the upper island still remaining with reduced size (fig. 27, top panel). The escape time map in this case shows that the web-like tangled structure disappears, being replaced with a swirling pattern within a more uniform chaotic space (fig. 27, center and bottom panels). Furthermore, no significant low escape channels are seen, opposed to the scenario before the transition occurs.

In summary, it was identified that as particles reach the energy level of local maxima points, two major islands composed of long flights are suppressed as the manifold structure folds into itself, forming a web-like pattern amidst which a myriad of islands appear, thus increasing the stable areas observed. This myriad quickly disappears as the energy increases, leaving behind itself a uniform chaotic sea with normal diffusion transport.

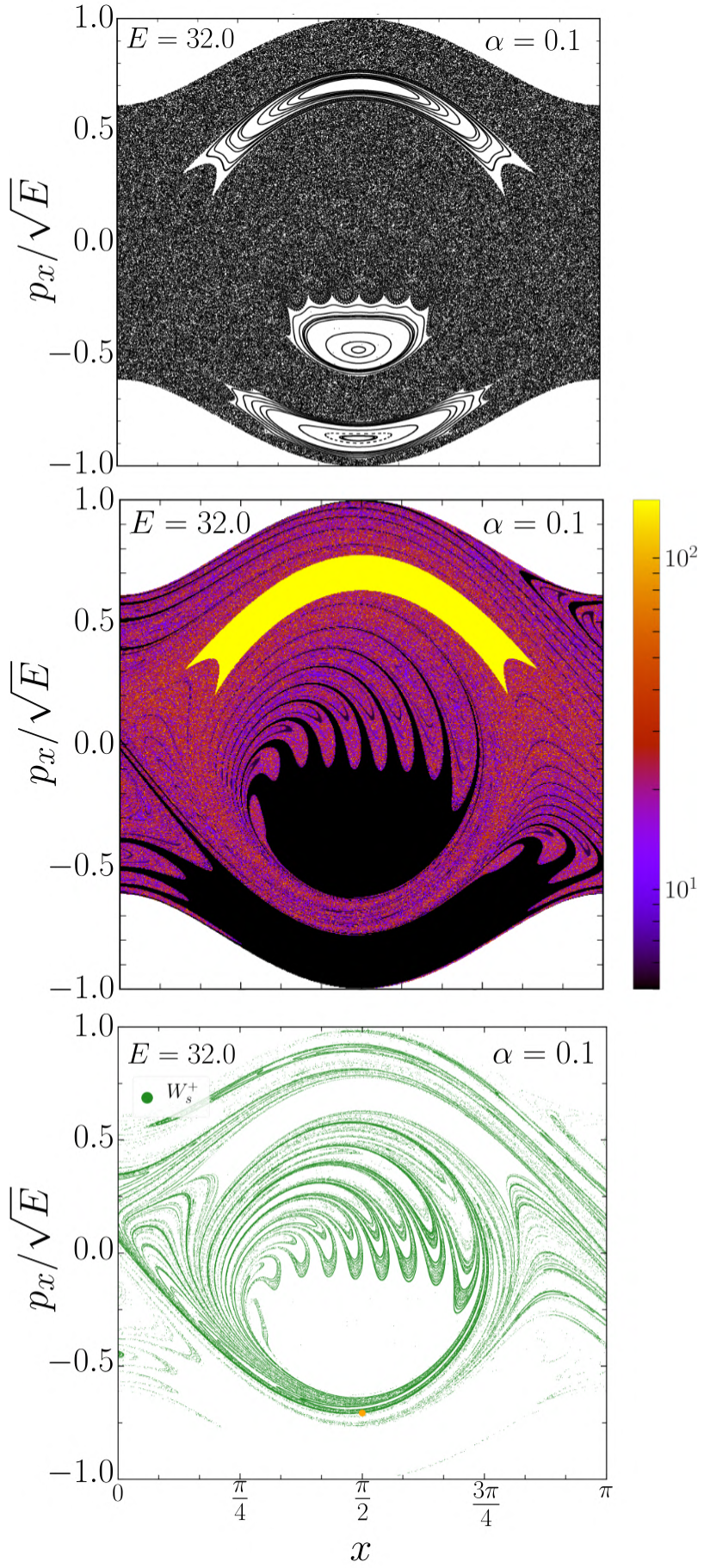

Figure 25: Phase-space portraits for $(E, \alpha) = (32, 0.1)$. (Top) PSS with orbits crossing points. (Center) Escape time color map. (Bottom) Stable manifolds from $\mathbf{U}_{\text{sad}}$.

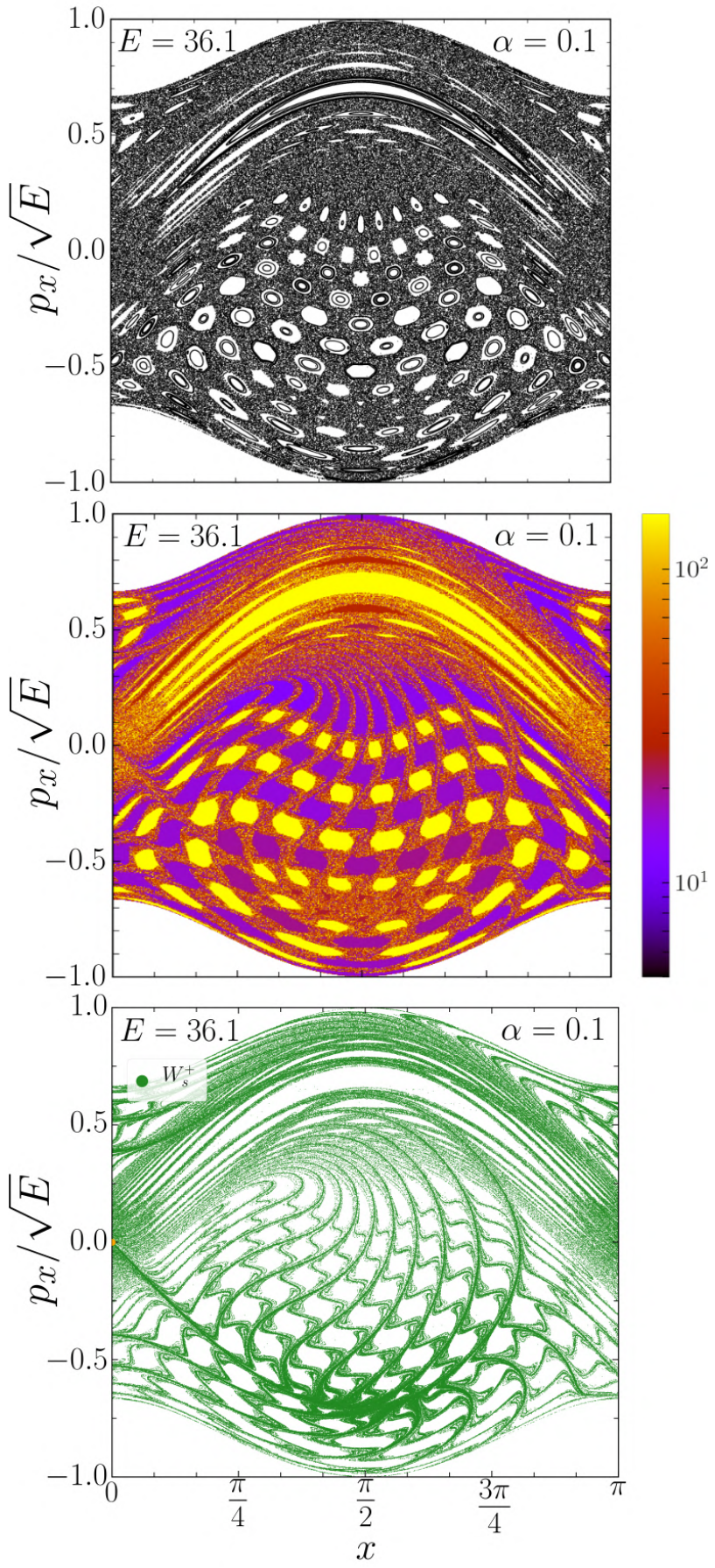

Figure 26: Phase-space portraits for $(E, \alpha) = (36.1, 0.1)$. (Top) PSS with orbits crossing points. (Center) Escape time color map. (Bottom) Stable manifolds from $\mathbf{U}_{\text{sad}}$.

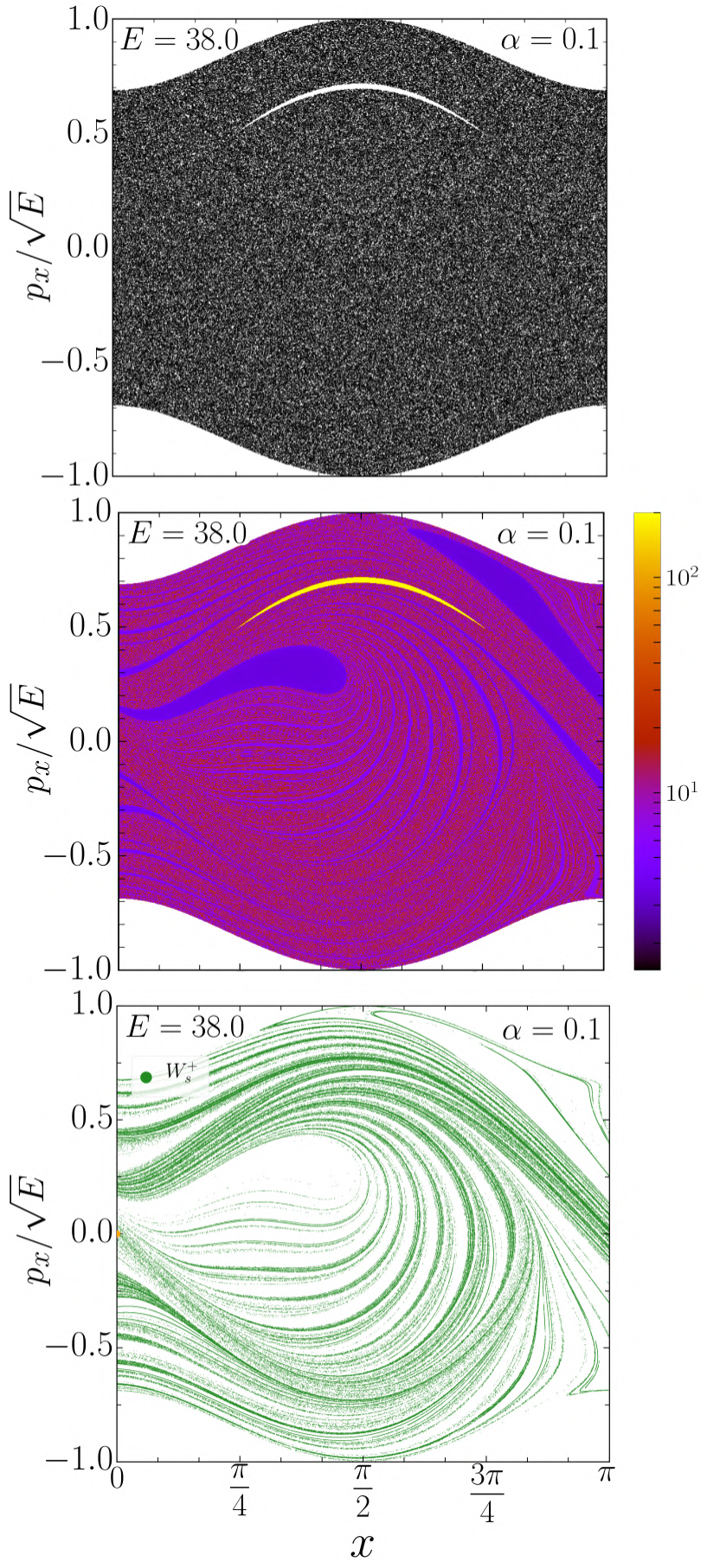

Figure 27: Phase-space portraits for $(E, \alpha) = (38, 0.1)$. (Top) PSS with orbits crossing points. (Center) Escape time color map. (Bottom) Stable manifolds from $\mathbf{U}_{\text{sad}}$.

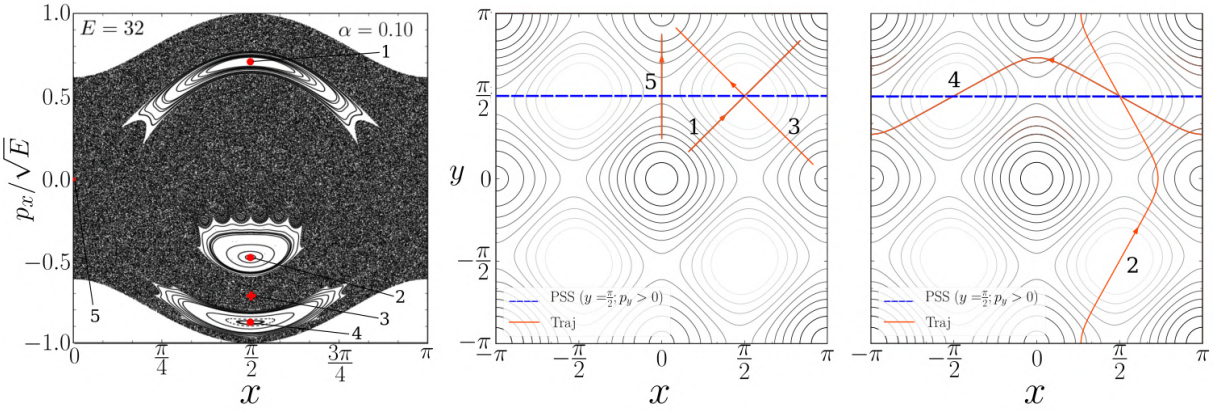

Figure 28: Periodic orbits for $E = 32$, $\alpha = 0.1$. In the left panel, the PSS with fixed points highlighted. The center and right panels show the respective spatial trajectories. The horizontal dashed blue line marks the PSS position.

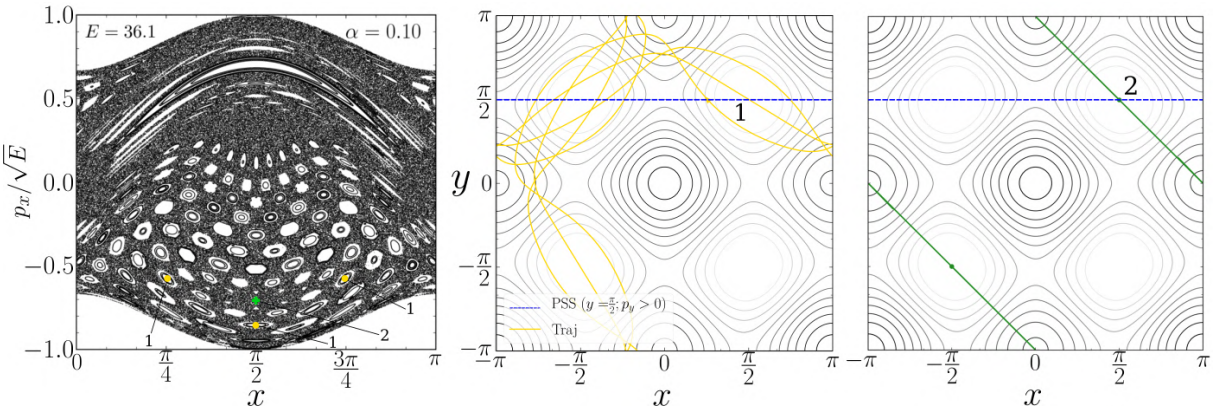

Figure 29: Periodic orbits for $E = 36.1$, $\alpha = 0.1$. In the left panel, the PSS with fixed points highlighted. The center and right panels show the respective spatial trajectories. The horizontal dashed blue line depicts the PSS Σ section.

4.4 Periodic orbits and time-period diagram

Complementary to the visual inspection of phase-space, it is interesting to discriminate how periodic orbits (PO) themselves change. Since stable periodic orbits (SPO) relate to stability islands and unstable ones (UPO) rule the chaotic dynamics by means of their manifolds, the set of periodic solutions provides a blueprint of the global dynamics – see section 3.3.

We start by showing the first main orbit bifurcation taking place in the system (for $\alpha = 0.1$), occurring for small energies below diffusion onset. Figure 30 displays this process as seen from the PSS Σ, where the initially stable orbit S_b undergoes a pitchfork bifurcation at $E \approx 7.6$, becoming unstable ($S_b \to U_b$) while two new SPOs, S_y and S_r, split from it. On further increasing the energy ($E = 17.6$), a thin chaotic layer becomes visible around U_b, surrounding the bottom and central islands in which S_y and S_r are at the center. For energies above saddle points (*i.e.* the diffusion onset at $E = 19.8$), the

SPOs S_y and S_r overpass them and therefore reach neighbor cells, forming the first main paths for particles diffusion, as seen for the two main islands in figure 25.

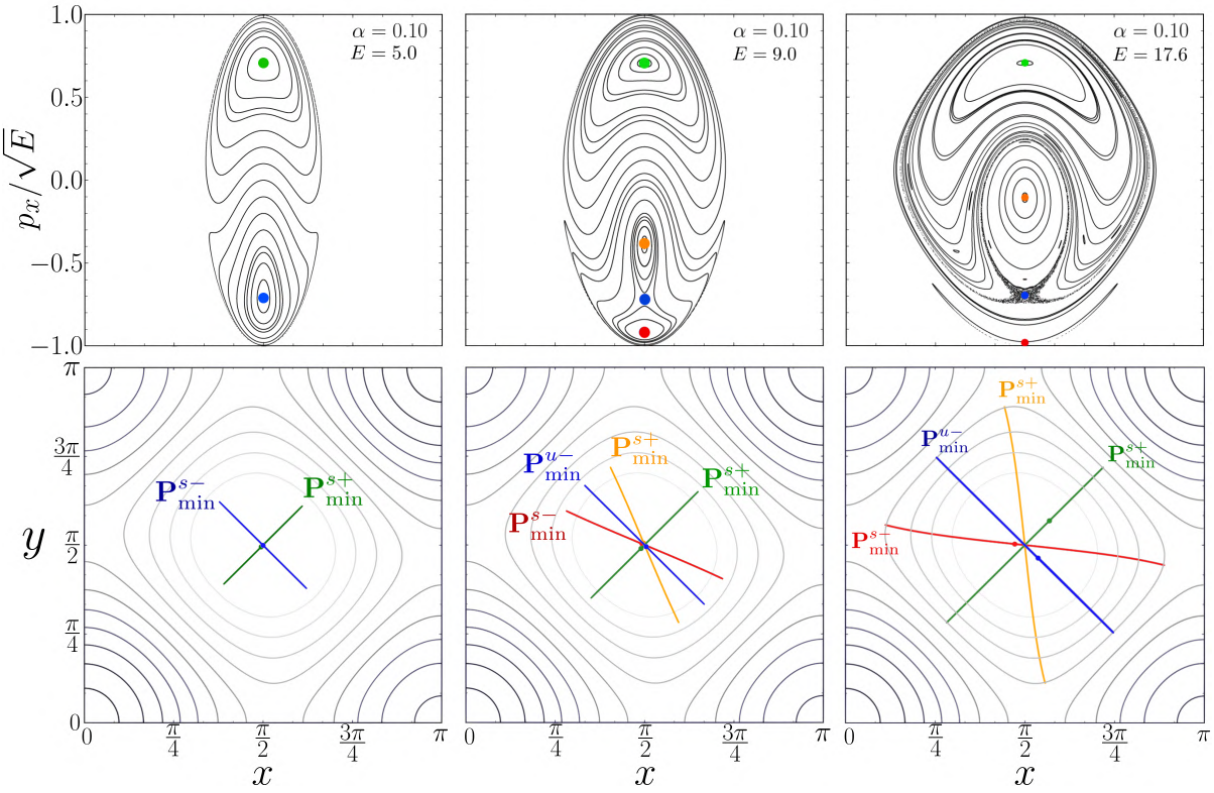

Figure 30: Pitchfork bifurcation for increasing energy as seen from the PSS Σ (top row) along with the corresponding trajectories (bottom row) and their respective highlighted fixed points (colored dots). Unstable (Stable) orbits are indicated by U (S) with a subscript for their color.

Soon after the diffusion onset, the system initially presents a free diffusion regime, as presented in section 4.1 for $\alpha = 0.1$. We thus look at the manifolds for this initial scenario considering three UPOs, shown in panel B from figure 31, namely one over the lattice minimum point ($\mathbf{U}_b$), and two along the stable direction of the saddle points at $(x_{\text{sad}}, y_{\text{sad}}) = (0, \arccos(-\alpha))$ ($\mathbf{U}_y$) and $(x_{\text{sad}}, y_{\text{sad}}) = (\arccos(-\alpha), 0)$ ($\mathbf{U}_x$), for an energy value slightly above diffusion threshold ($E = 22$). The resultant manifolds are shown in panels C and D.

Even though these manifolds belong to the same compact chaotic domain (fig. 31, panel A, one can notice in panel C that the dynamics in this region presents two transitory regimes. An outer layer, with higher momentum values, is shown by the unstable branch of $\mathbf{U}_y$ and indicates transport between lattice cells, as it connects unit cell minima regions at $x = 0$ and $x = \pi$, whereas an inner layer, shown by the stable branch of $\mathbf{U}_b$, is responsible for chaotic motion around lattice pits. Besides, although these branches will eventually cross each other infinitely many times, their turnstiles, *i.e.* the area between manifold lobes crossings, are small, indicating weak mixing. When looking at the stable branch from $\mathbf{U}_b$ along with the unstable one from $\mathbf{U}_x$, one sees the same separation, with the central island surrounded by the unstable branch.

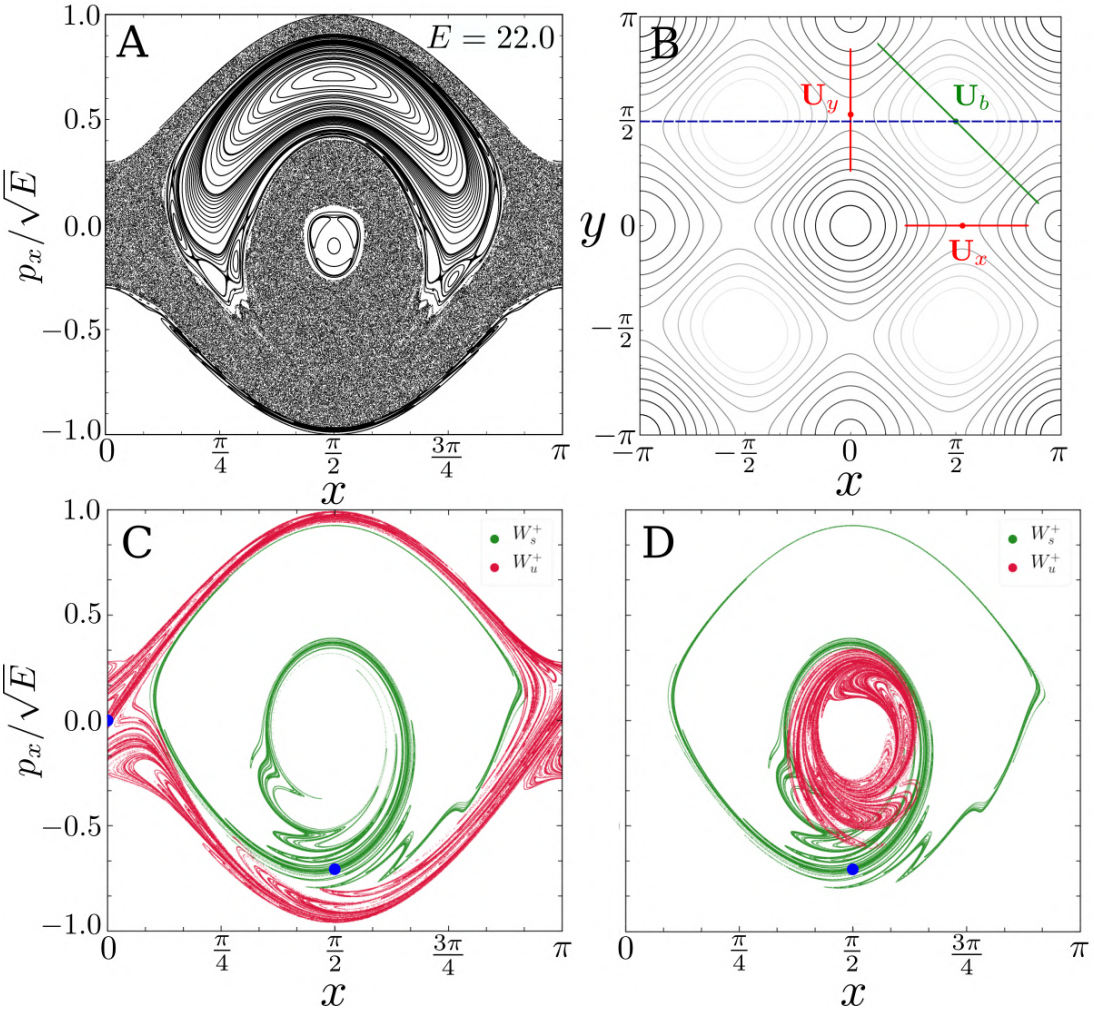

Figure 31: A) PSS Σ for $E = 22$. B) UPOs used for the calculation of the manifolds displayed at frames C and D. C) Stable (green) and unstable (red) manifold for U_g (U_y). D) Stable (green) and unstable (red) manifolds for U_g (U_x). In frame B, the blue dashed line marks the surface Σ and the blue dots in the remaining frames the fixed points from UPOs within it.

In order to provide a wider picture of POs as the energy varies, one can make use of the monodromy algorithm (sec. 3.3) and construct a diagram, with the period τ of the orbits found in one axis, and their energy on another. This diagram can thus depict orbits bifurcations and period increases along transitions. It is worth emphasizing that the period considered for this calculation here is the dynamical one, *i.e.* the time evolved until POs close themselves, instead of the integer period related to its fixed points in a PSS map. Figure 32 shows such a diagram for $\alpha = 0.1$. The algorithm was run by exhaustively searching for periodic orbits with discrete period 1 and 2 in the PSS. Note that, analogously to a Newton-Raphson method, the algorithm may not converge to the desired PO for every initial condition given, thus being dependent on an 'attraction basin'.

The two horizontal dashed lines in figure 32 mark the energy for diffusion onset, at $E = 19.8$ and the transition selected for study here, at $E = 36$. One immediately notices that a set of orbits diverge in period while reaching each of these lines, as though as approaching the line asymptotically. These are homoclinic orbits, such as orbit 2 in figure

29, that when approaching unstable equilibrium points take an infinite amount of time to reach it, slowing down the dynamics. This phenomenon in commonly exemplified by the pendulum model when it has enough energy to reach its unstable equilibrium position, taking an infinite 'period' to complete a revolution. Here, this behavior is expected for the set of orbits approaching either the saddle point, the local or global maxima.

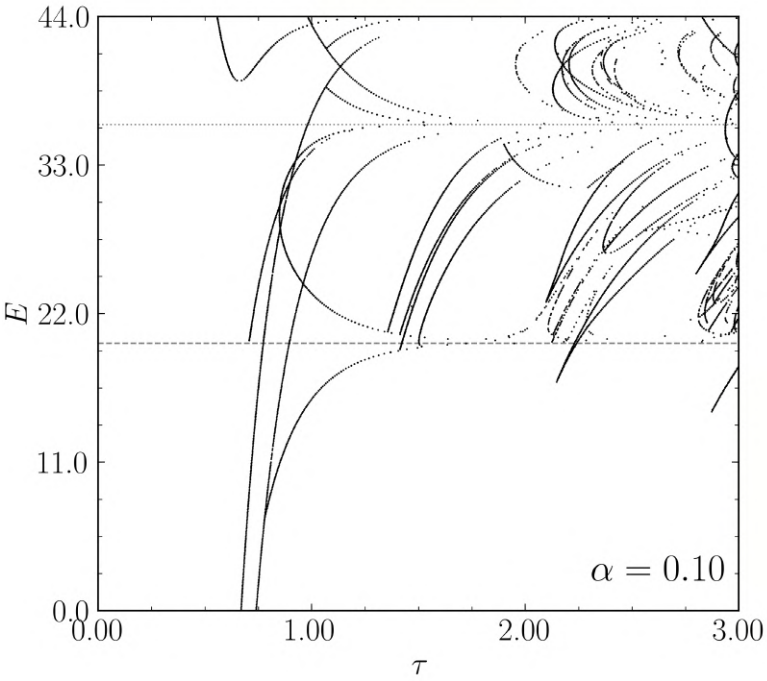

Figure 32: Period-energy diagram for $\alpha = 0.1$. The dynamical period τ corresponds to the time required for orbit completion. In this case, only orbits with map period of 1 and 2 are considered. The horizontal dashed gray lines mark the energy of saddle equilibrium points $E = 19.8$ and local maxima $E = 36$, where the diffusion transition studied occurs.

It is worth pointing out that, since the potential function for the square lattice has symmetry for rotations of $\frac{\pi}{2}$ and translations of $2m\pi$, for $m \in \mathbb{Z}$, for any given trajectory, its symmetrical counterpart will also be a solution; thus implying that identical periodic orbits always occur by changing $x \rightleftarrows y$. Therefore, symmetric pairs of POs end up having the same dynamical period τ, thus appearing as a single overlapped point in the $E \times \tau$ diagram. This can be seen in figure 32 for the pitchfork bifurcation described in figure 30, where the points relative to the new bifurcated orbits S_y and S_r correspond to a single position in the diagram at $E > 7.6$.

5

Results: Island Myriad

"The chief forms of beauty are order and symmetry and definiteness, which the mathematical sciences demonstrate to a special degree."
Aristotle, *Metaphysics*

From the previously identified island myriad phenomenon, a thorough investigation and description of its features is given. Starting with the island chains organization, the main periodic orbits are shown to reflect the potential function symmetries, explaining its isochronous nature and the difference of transport rate between chains (sec. 5.1). Beyond the particular transition previously studied (that for $\alpha = 0.1$ and $E = 36$), the evolution of the myriad is analyzed along with the changes on local maxima points with the control parameters (sec. 5.2). Based on the properties observed, the existence of the phenomenon is also verified for a hexagonal lattice (sec. 5.3).

5.1 Island myriad

In what follows for the remaining sections, we turn to the investigation of the island myriad found. Initially, it was seen that its structure is composed of multiple island chains with even period, all of them concentric around the fixed point related to the UPO along the line connecting two local maxima – orbit 2 in figure 29, forming an onion-like structure. Figure 33 shows a colored map of the phase-space for the myriad. One can notice that in between chains, smaller ones appear, displaying a clear fractal structure, as it is expected for bifurcations of islands in accordance to the KAM theorem [36], although not always as clearly seen as in this case.

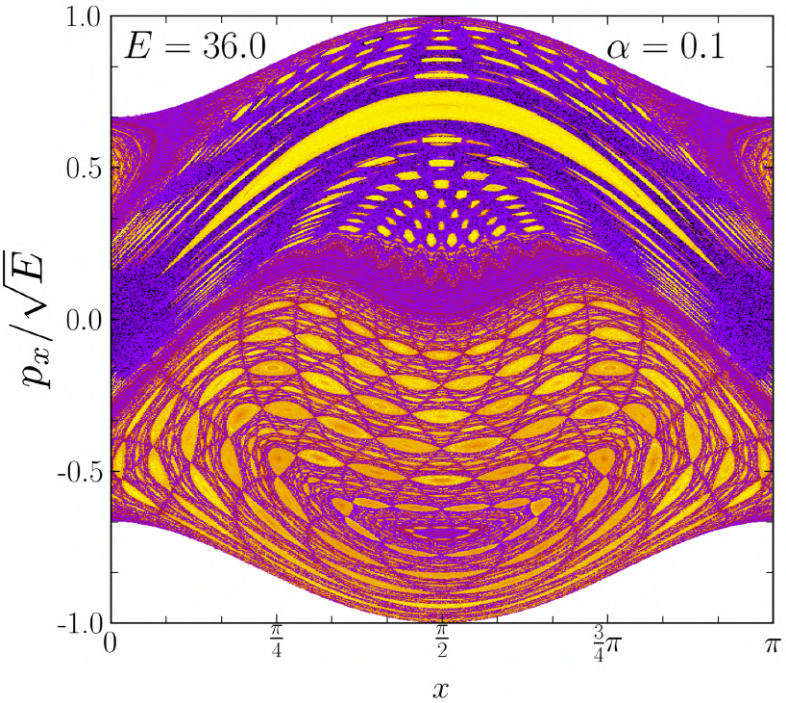

Figure 33: Colorized phase-space portrait of the island myriad for $\alpha = 0.1$ and $E = 36$, exactly at the local maxima energy level. Colors were set using the SALI index value to emphasize island regions.

In detail, each chain is actually formed not by a single SPO with map period $2n$, for $n \in \mathbb{Z}$, but instead by two orbits of period n, thus being referred to as isochronous islands (fig. 34). The orbits that form each chain are symmetric pairs, translated by $(n\pi, m\pi)$ or rotated by $(n+1)\pi/2$ in space, for $n, m \in \mathbb{Z}$. This condition is only possible due to the square lattice symmetries and in particular to its 'tiling' closure property, the same

that allows for the use of periodic boundary conditions (PBC). Consequently, these orbits appear in the same chain since they have the same rotation number[2]. It is also possible that an isochronous chain may be formed by more than two twin orbits, in case the fixed point period of a PO is the same when rotated more than two times by $\frac{\pi}{2}$. Appendix G shows an example of this feature for a period 12 chain within the myriad.

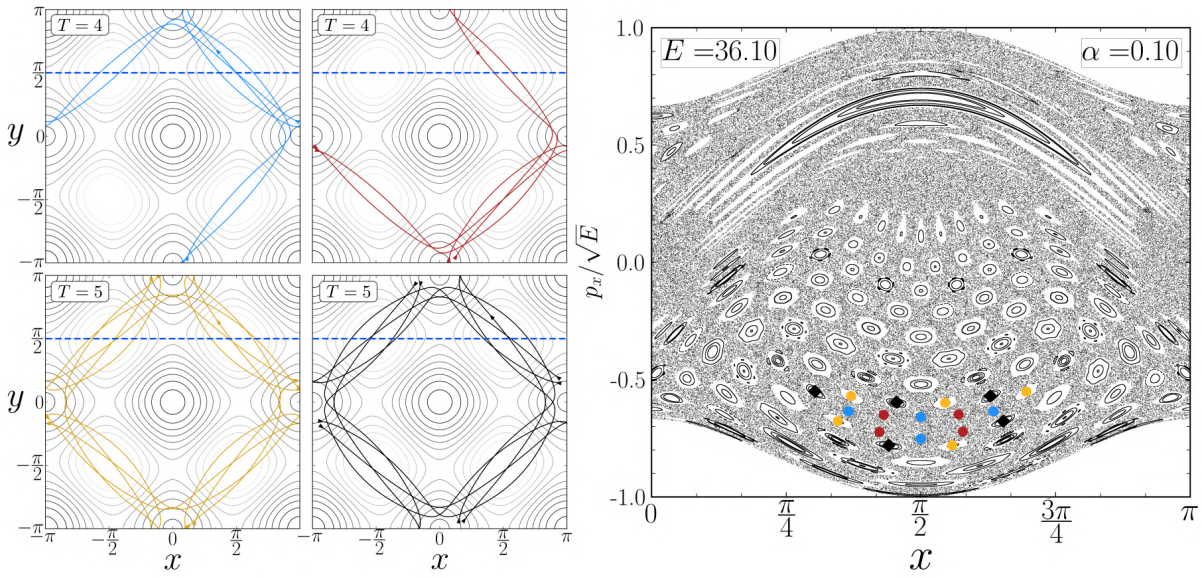

Figure 34: Isochronous orbits composing island myriad chains. The colored dots indicate the fixed points of the trajectories relative to the PSS Σ (blue dotted line). The innermost period 8 chain is formed by the blue and red orbits while the immediate next one, with period 10, by the yellow and black ones.

For clarity, it is worth emphasizing that the trajectories shown here take into account PBC, in such a way that they are 'cut' and placed into the opposite boundary when passing over the lattice unit cell limits ($x, y \in [-\pi, \pi]$). This aspect is particularly relevant to understand the alternate escape time behavior observed in figure 26 (middle panel). In it, some chains present the limit escape time, thus not escaping at all, whereas others escape quickly.

When inspecting the SPOs associated to each kind of chain, it is found that some return to their exact initial position, even when disregarding PBC (fig. 35), whereas others only do so with PBC (fig. 36). Therefore, the former are closed loops and have limited range, thereby never escaping, whereas the latter travel in almost direct flights through the lattice, as shown in figure 37. Such a feature is only possible due to the 'tiling' periodicity property of the potential function, once that a translated position $(x, y) \to (x \pm 2n\pi, y \pm 2m\pi)$, for $n, m \in \mathbb{Z}$, will correspond to an identical site inside a neighbor unit cell, thus allowing for periodic behavior without return to the exact position where the trajectory starts.

[2]Among different applications, the winding number ω can be calculated as the average ratio of angular growth for a variable $\theta(t)$ as $\omega = \lim_{n\to\infty} \frac{\theta_n - \theta_{n-1}}{n}$. The angle variable can be defined from the canonical space coordinates or over a PSS map, relative to the center of an island.

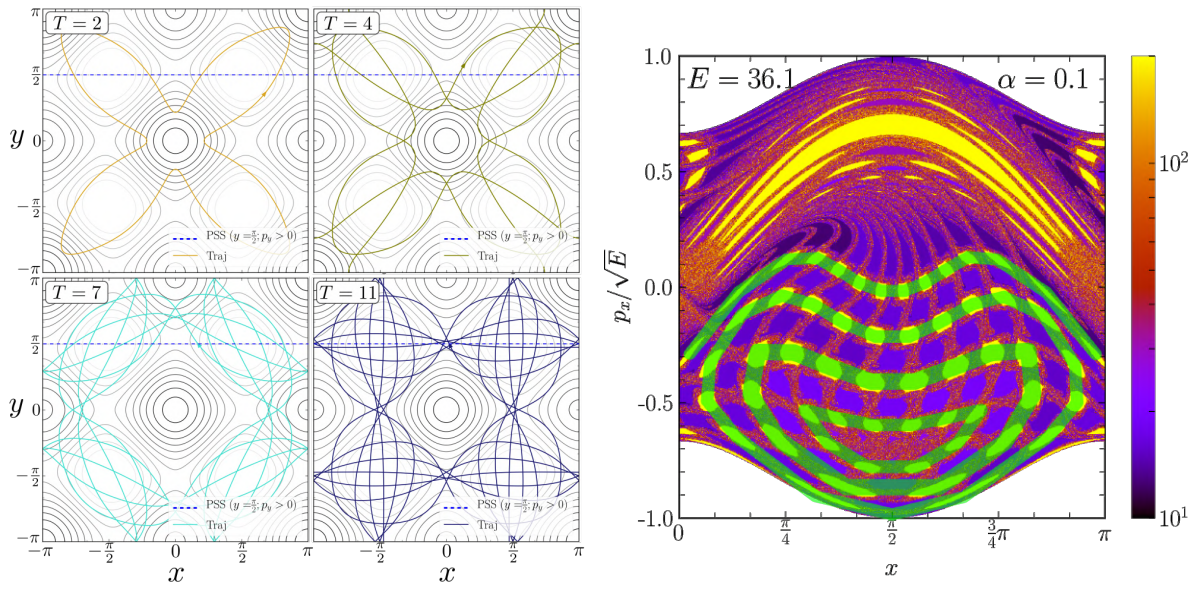

Figure 35: Periodically closed orbits from island chains with high escape time (from the highlighted green layers).

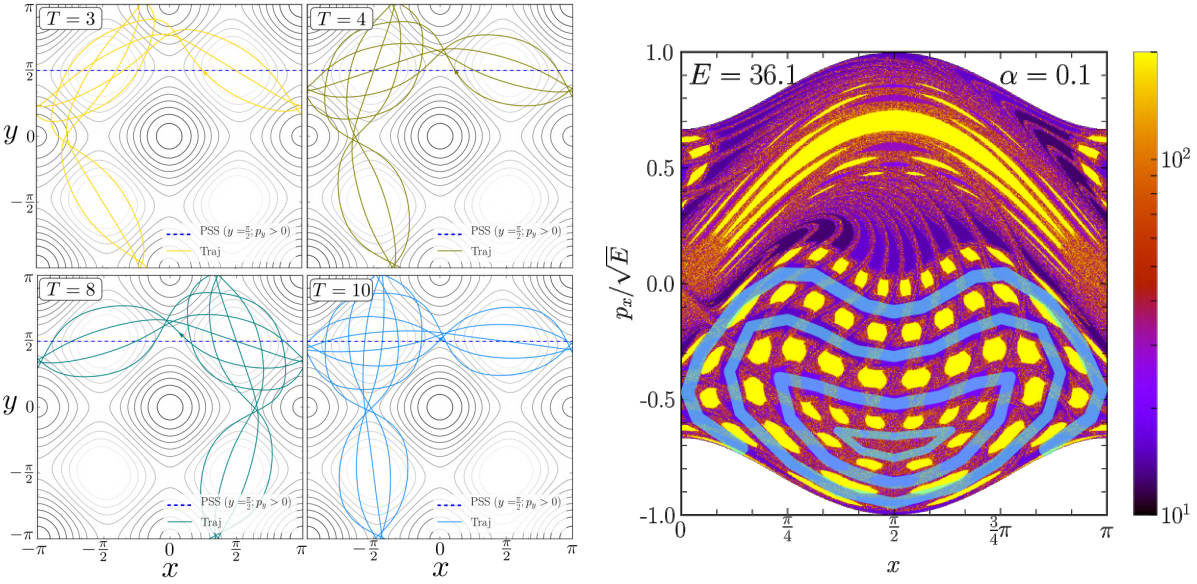

Figure 36: Periodically open orbits from island chains with low escape time (from the highlighted blue layers).

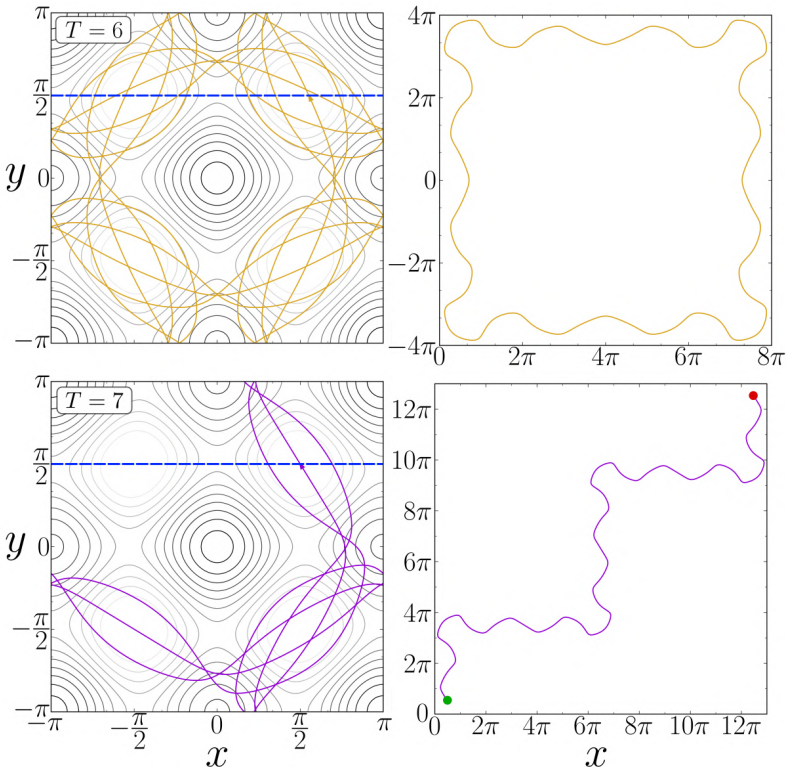

Figure 37: Examples of periodic orbits with different spatial closure. On the left column, trajectories within the unit cell and PBC applied. On the right column, trajectories without PBC, ranging through all space.

5.2 Separatrix reconnection

As asserted initially, the island myriad is expected to emerge anytime orbits reach the energy level of unstable equilibrium points (see for example appendix H, showing the island myriad for global maxima). However, the energy of these points changes with the coupling α, thereby raising the possibility of analysing the myriad evolution as the unstable points change themselves. For this purpose, figure 38 compiles phase-space portraits for energy values along the local maxima energy $V_{\text{l-max}} = 2U(1-\alpha)$, corresponding to the white line in the chaotic area color map profile in figure 22.

For increasing α, the fractal structure of the myriad is well apparent until $\alpha \approx 0.5$, as seen for $\alpha = 0.105$ to $\alpha = 0.430$ in figure 38. On further increasing the coupling, the myriad innermost structure (centered at $x = \frac{\pi}{2}$ and $\frac{p_x}{\sqrt{E}} \approx -0.75$) bifurcates into two main islands (see $\alpha = 0.637$ in fig. 38), with a more uniform chaotic layer surrounding it. For even higher values of α, the myriad region furthers diminishes in area while the phase-space is dominated by the uppermost stability island and secondary chains.

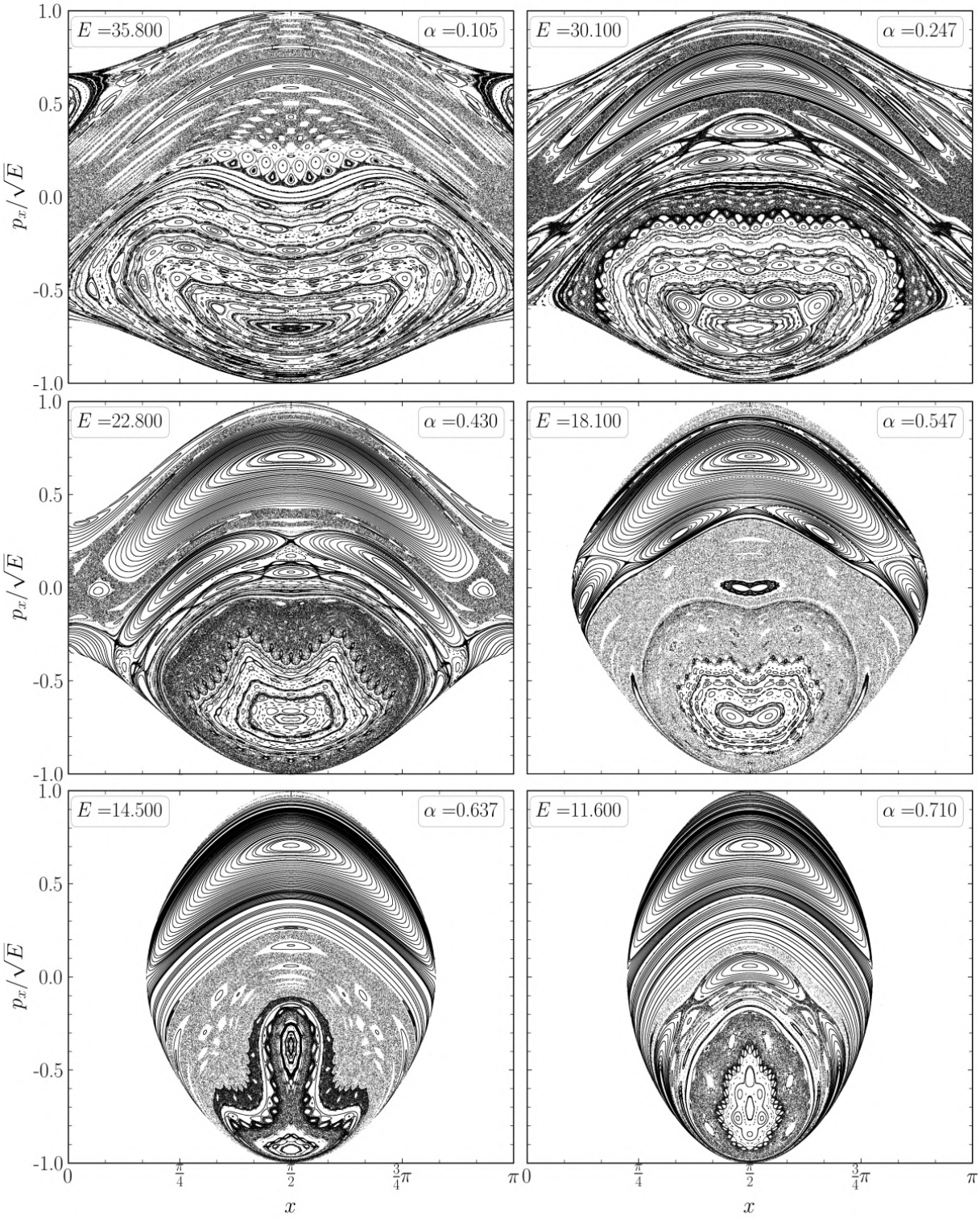

Figure 38: Phase-space portraits for α values along the local maxima line.

A particular feature occurring when increasing the control parameters α and E over the local maxima line is the bifurcation and further disappearance of the islands chains. Within the myriad, one may note the central concentric layering of chains but also an outer thin ring of islands right beyond a chaotic region, surrounding the whole myriad. As the control parameters increase, the innermost chains move outwards and eventually meet

with the outer ones that move inwards, relative to the fixed point center. The process of collision of these chains is a phenomenon called separatrix reconnection [51], as illustrated in figure 39, for two period 6 chains and in figure 40 for period 4 chains.

In this case, the outer and inner chains are interdigitated relative to each other, in the sense that the stable centers of islands from one chain align with the saddles (unstable points) of the other. When they meet, the separatrix is divided and changes its shape and topology, with the previous outermost chain now inside the center myriad structure and the former inner chain immersed in the chaotic area. This process keeps on going continuously and sequentially as the inner chains move outwards, always in an interdigitated configuration relative to the outer ones, then reconnecting and further disappearing, eroding the myriad with chaos until it vanishes for $\alpha = 1 \implies E = 0$.

Commonly, the scenario of separatrix reconnection is seen in non-twist systems, more widely studied in the standard form [51]. In such systems, the twist property, *i.e.* the monotonic increase of the winding number with the action variable, is violated, presenting minimum or maximum points. These extreme points further indicate the existence of shearless curves, forming transport barriers between chaotic regions, and the interdigitated island chain pair are resonances occurring for equal winding number, above and below the shearless curve. Here, this arrangement is seen when considering the local winding number relative to the island myriad center. The related shearless curve would thus be expected to occur between the interdigitated islands that reconnect; however, the constant presence of the chaotic layer between them prevents a direct verification via winding number calculation.

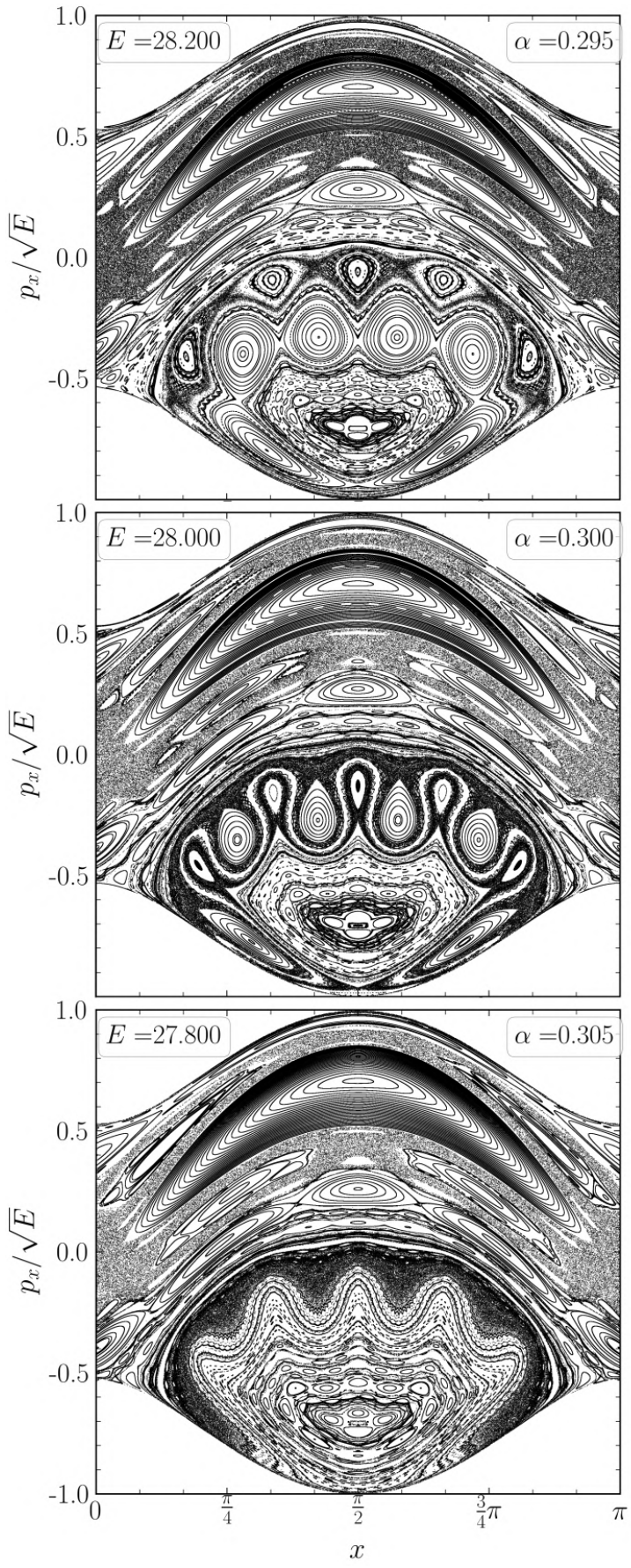

Figure 39: Separatrix reconnection of islands within the myriad as (α, E) vary on the local maxima line. The coupling increases from top to bottom, $\alpha = 0.295 \to 0.305$ and $E = V_{\text{l-max}}(\alpha)$.

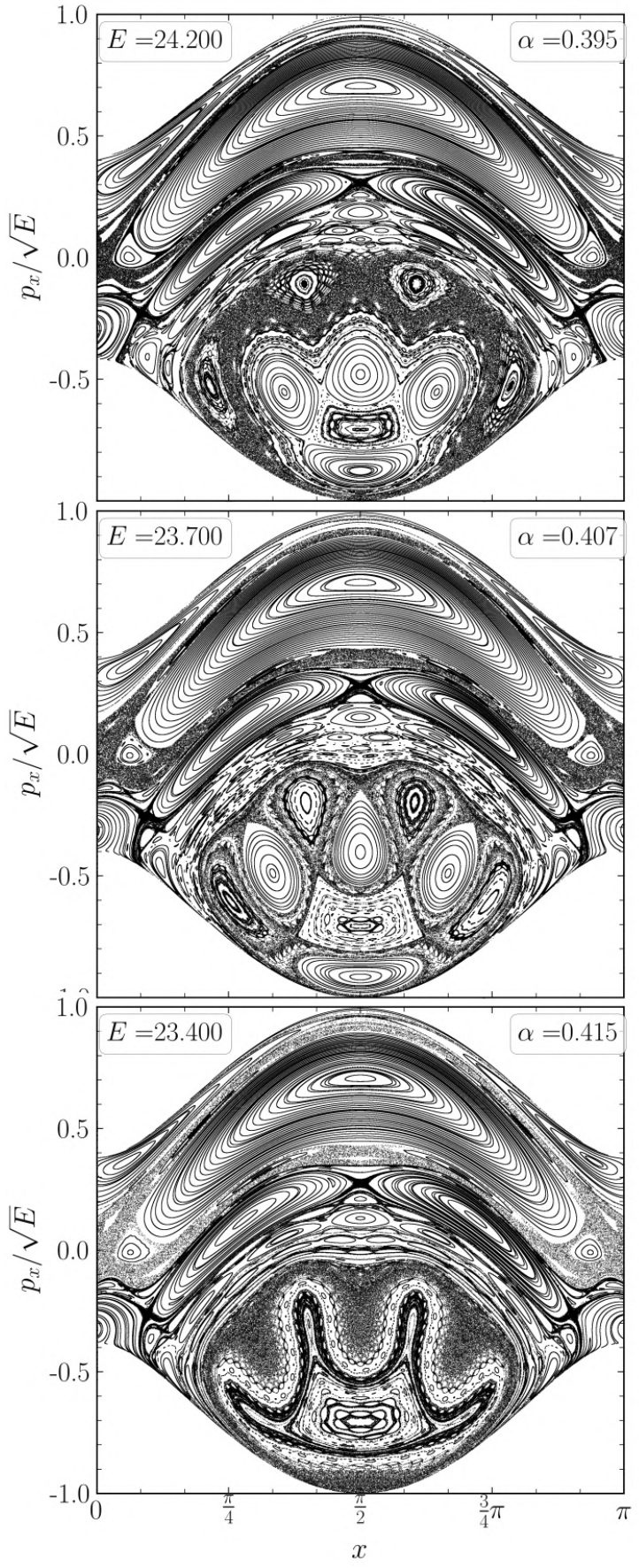

Figure 40: Separatrix reconnection of islands within the myriad as (α, E) vary on the local maxima line. The coupling increases from top to bottom, $\alpha = 0.395 \to 0.415$ and $E = V_{\text{l-max}}(\alpha)$.

5.3 Hexagonal lattice

As conjectured, the island myriad phenomenon is expected to occur in any periodic potential system when particles reach the energy level of unstable equilibrium points. Furthermore, the tiling periodicity property is necessary to obtain solutions that have both rotational and translational symmetries allowing for twin pairs, with identical winding number and thereby forming isochronous chains. Therefore, based on these premises, one immediately expects that lattices with triangle, square and hexagonal symmetries, that is, the only regular convex polygonal shapes with such a feature, will present the myriad phenomenon.

Thus, the case of a hexagonal lattice was investigated in order to assert the existence of the myriad. As described in the model chapter (sec. 2.3), a single parameter scenario was assumed; in this case, some equilibrium points are symmetrically arranged in space and were selected as reference for the energy lines related to unstable equilibrium points. Figure 41 shows how these reference points change their energy and stability in the single coupling scenario. For clarity of notation, the coupling parameter for the hexagonal lattice will be labeled as β.

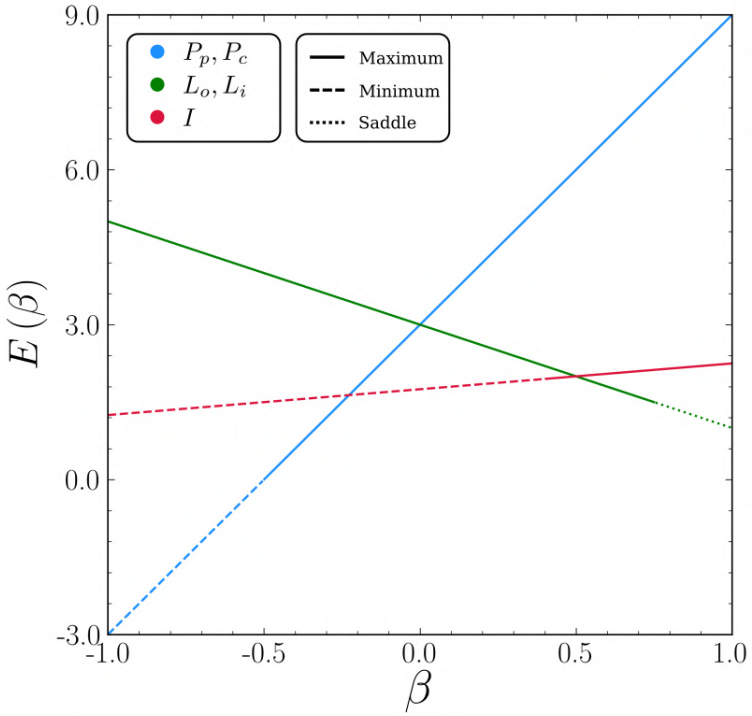

Figure 41: Energy lines and stability for the selected equilibrium points for the hexagonal lattice. See table 2 for reference on the legend.

Before turning to the energy lines, we anticipate that the myriad was found for the hexagonal lattice only for $\beta \approx 0$, and in less pronounced form, as shown in figures 42 and 43 for $\beta \gtrsim 0$ and $\beta \lesssim 0$, respectively. As seen for $\beta \gtrsim 0$, two clear sets of islands appear around a central major island and on the rightmost section of the PSS ($\beta = 0.02$ in fig. 42). Despite its small size, the myriad is notably visible due to a strong stickiness effect, forming a permeable barrier between the chaotic region surrounding the central

island and the remaining chaotic sea. As the coupling increases, islands increase in size as well but decrease in number, although still preserving a semi-barrier effect (fig. 42 for $\beta = 0.04$ and $\beta = 0.06$). For negative values of β, a different configuration is found in the PSS but still presenting a semi-barrier ($\beta = -0.03$ in fig. 43), diminishing along with the coupling until it completely vanishes, preserving only a few sparse islands amidst the chaotic sea ($\beta = -0.2$ in fig. 43).

The presence of the myriad in attenuated form, with smaller islands and surrounded by chaos, is credited to the presence of extra sources of instability, mostly due to unstable points in the potential (not among the selected ones, as seen in figure 8). In this way, the presence of the myriad only for $\beta \approx 0$ must hold from the similar energy level that points $P_{p,c}$ and $L_{o,i}$ have, as shown in the energy line diagram (fig. 41), and therefore act as symmetrical scatterers, enabling periodic trajectories to be stable. For other values of β along any of the energy lines shown, the presence of other saddles or maxima may perturb these orbits and turn them unstable, thus preventing the myriad appearance.

Nonetheless, the same leveling of local maxima energy is seen for $L_{o,i}$ and I equilibrium points at $\beta = 0.5$, thus suggesting the phenomenon to occur at this coupling value also, although the same was not observed. In fact, in this case, the energy level may be too low, as compared to what is seen for the square lattice for $\alpha \gtrsim 0.5$, where the myriad structure becomes less visible for higher coupling. From a mathematical perspective, one could argue that the potential in the Hamiltonian for the hexagonal lattice will always be non-linearly coupled, even for null β, given that it is formed by three wave-vectors over a plane, thereby making one of them linearly dependent of the others. This non removable perturbation is then a source of instability that at the energy level of $L_{o,i}$ and I for $\beta = 0.5$ is non negligible.

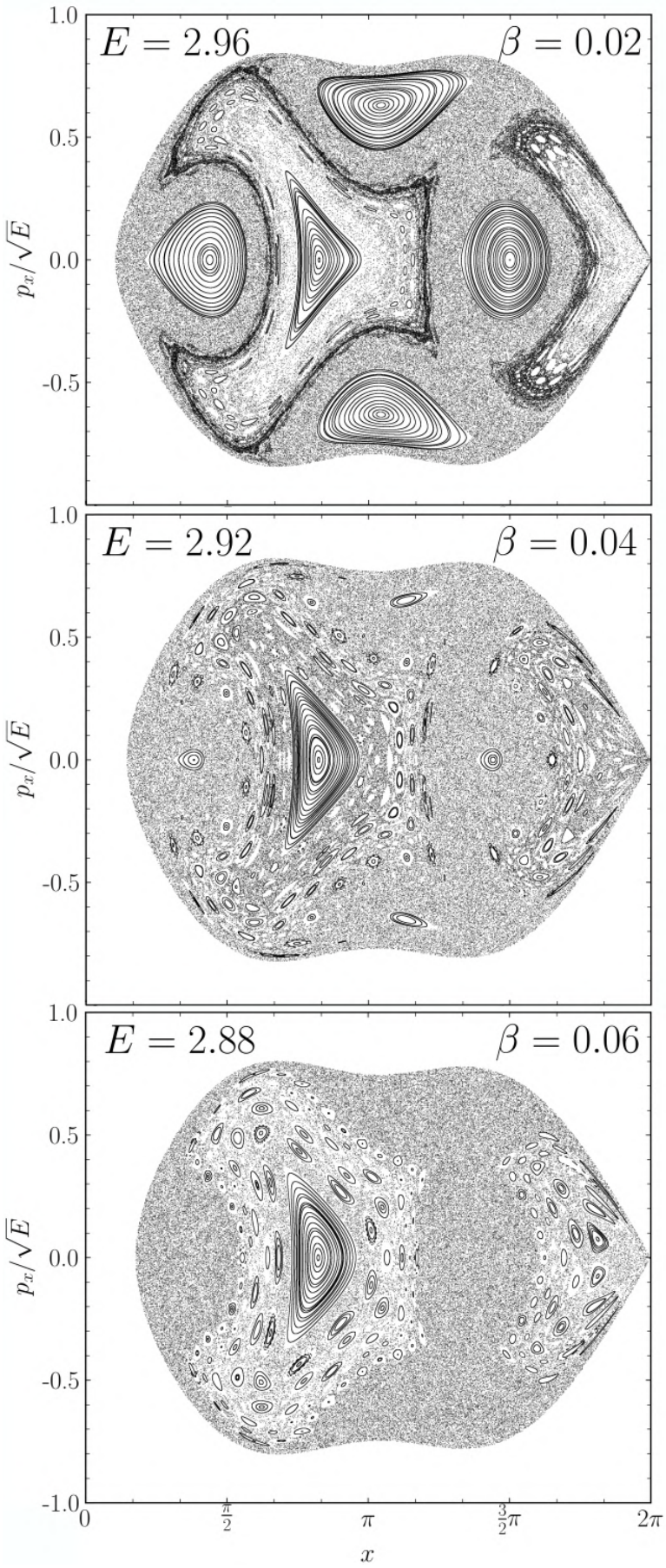

Figure 42: Phase-space portraits showing island myriads for the hexagonal lattice for coupling values for $\beta \gtrsim 0$. In this case, the PSS is set for $y = 0, p_y > 0$.

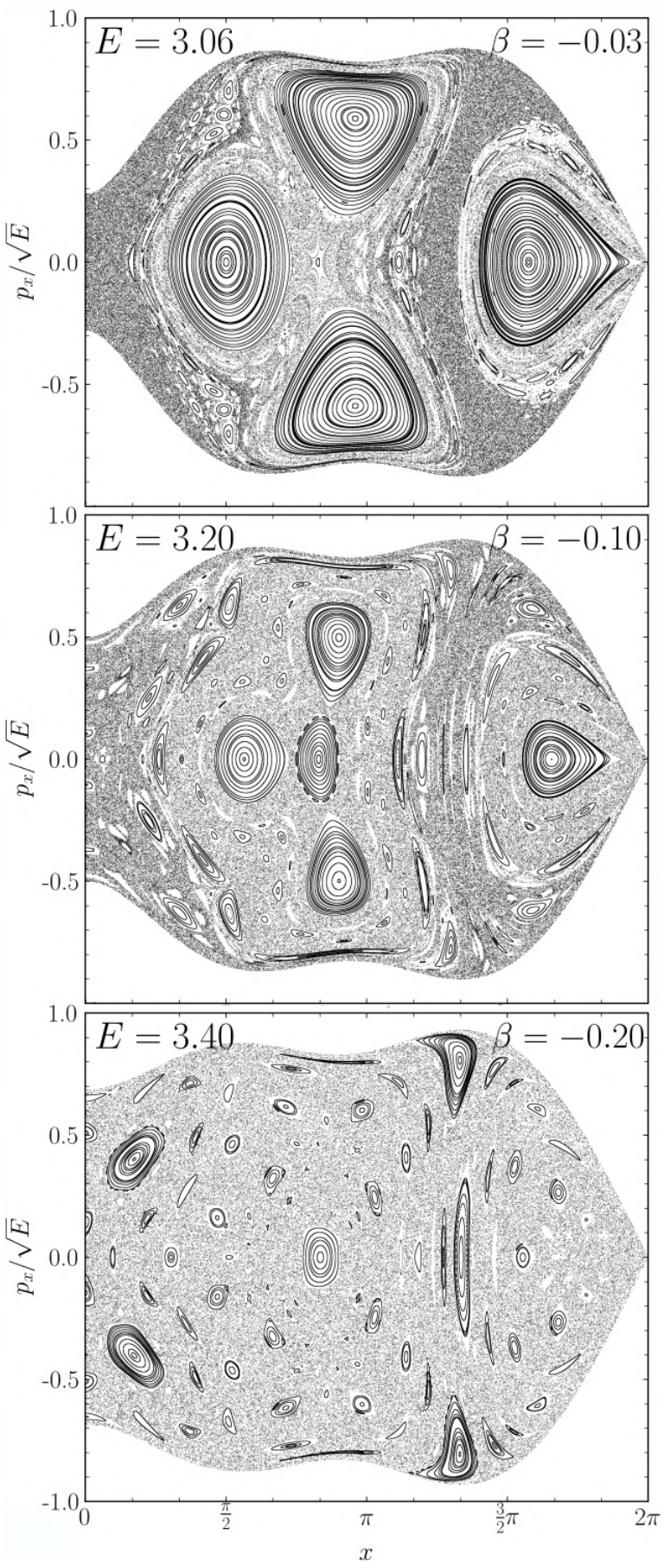

Figure 43: Phase-space portraits showing island myriads for the hexagonal lattice for coupling values for $\beta \lesssim 0$. PSS set for $y = 0, p_y > 0$.

6

Conclusions

"Good judgement is the result of experience; experience is the result of bad judgement"
Mark Twain

The study presented here initially focused on the spatial diffusion of particles in a square lattice potential, as modeled by a classical Hamiltonian with periodic potential. With the main interest of understanding how particles' movement through the lattice changes as its main parameters vary (*i.e.* the energy E and coupling α), a diffusion exponent μ measure was carried on. When measuring μ, sudden and unexpected transitions between normal and free (ballistic) regimes were found to occur over all parameter space ($E \times \alpha$) (sec. 4.1). Regarding system control, the global map obtained for μ allows one to discriminate whether particles remain more or less confined within the lattice, based on the existence of different transport regimes.

In a first inquirement, calculations of the chaotic area revealed the emergence of stability structures in phase-space for particular transitions in diffusion regimes when local maxima points of the potential become accessible (sec. 4.2). A particular coupling value, namely $\alpha = 0.1$, was then selected for a in depth analysis to describe this kind of transition. In this case, as the energy E varies, the diffusion exponent undergoes a sudden suppression, dropping from free to normal regime, while correlating with a sharp peak where stability area increases.

This suppression in transport can be regarded as counter-intuitive, for even though local maxima are surpassed, thus widening the path for transport between lattice cells, long flights vanish during the process. For an in deep description, a variety of numerical techniques were employed to characterize the dynamics in phase-space (sec. 4.3). For the particular case selected, it was found that previous to diffusion, two main stability islands promote the transport of particles, as seen from their low escape time, with extensions to the chaotic sea.

As the manifolds that delineate these islands fold and collapse, a web-like pattern is formed from within which the emergence of stability structures appear as a myriad of island chains. This island myriad lasts only for a narrow energy window during the moment of transition, after which a chaotic sea with uniform normal diffusion rate dominates the phase-space. Besides the myriad appearance and long flights suppression, at the energy level of local maxima points homoclinic orbits reaching them diverge in period, promoting a slow down of the dynamics (sec. 4.4). This first part of results (chapter 4) was published under the reference: 'M. Lazarotto, I. L. Caldas and Y. Elskens; "Diffusion transitions in a 2D periodic lattice', CNSNS, 112 (2022)" [52].

When focusing on the myriad structure found, it appears as a highly fractal layering of island chains with even period, concentrically organized around the UPO fixed point from the homoclinic orbit connecting local maxima (sec. 5.1). Due to the square lattice translational and rotational symmetries, these chains are isochronous, being formed by symmetric (twin) orbits with same winding number. As seen from escape time measurements, different chain layers in the myriad present orbits that can either remain trapped in the lattice or escape quickly. Each case relates to the property of SPOs to return to their

initial position regardless of periodic boundary conditions, either forming closed loops when they return or instead forming open curves when they do not, thereby promoting unrestricted transport of particles.

For energy and coupling parameters varying over the local maxima energy line, the concentric island chains are seen to undergo separatrix reconnection, being sequentially destroyed by colliding with external chains in an interdigitated configuration, as commonly seen in non-twist scenarios (sec. 5.2). It is interesting to note that the isochronous effect and separatrix reconnection seen here arise from features in the potential function, being rather intuitive to understand dynamically, opposed to mathematical scenarios where a physical interpretation of these phenomena is lacking.

Complementarily, the island myriad was also observed for a hexagonal lattice, in order to assert the hypothesis that the phenomenon is exclusive to potentials with tiling symmetry (sec. 5.3). Indeed, the phenomenon was found but in attenuated form and for a smaller coupling parameter window, since extra sources of instability in the potential surface for the hexagonal lattice prevent the existence of stable orbits to form the myriad. It is still an open problem if potentials with alternative tiling properties, such as Penrose tilings [53], could present the same phenomenon.

Appendix

Software and tools

All numerical simulations done for this work were carried on `C/C++` programming language [37] with particular use of GSL (GNU Scientific Library [54]) ordinary differential equation library (`gnu.org/software/gsl/doc/html/ode-initval.html`) for the RKCK integration method.

The analysis methods presented were based on the references cited throughout the text but manually implemented, including Tao's symplectic integration method, which is made available at the online repository `github.com/matheuslazarotto/SymplecticTao`. Also, the code for chaotic/regular area calculation is openly available at the Oscillation Control Group repository page at: `yorke.if.usp.br/OscilControlData/Chaotic-Stable-area/`. An application for dynamical systems analysis and exploration was developed along the thesis work in collaboration with V. Oliveira and M. Palmeiro, and is made available at `github.com/segmentation-chaos/dynamical_systems`.

A Single coupling condition for the hexagonal lattice

When assuming the single coupling condition for the hexagonal lattice, it is required to check whether it is feasible physically, once the couplings α_{ij} can be related to each other geometrically. Following Porter *et al.* [25], by assuming the first wave polarization versor $\hat{e}_1$ along the $\hat{z}$ direction, the remaining ones can be written in terms of spherical angles (θ_j, ϕ_j) as

$$\begin{cases} \hat{e}_1 = \hat{z} \\ \hat{e}_2 = \cos(\phi_2)\sin(\theta_2)\ \hat{x} + \sin(\phi_2)\sin(\theta_2)\ \hat{y} + \cos(\theta_2)\ \hat{z} \\ \hat{e}_3 = \cos(\phi_3)\sin(\theta_3)\ \hat{x} + \sin(\phi_3)\sin(\theta_3)\ \hat{y} + \cos(\theta_3)\ \hat{z}, \end{cases}$$

with $\phi_j \in [0, 2\pi)$ and $\theta_j \in [0, \pi]$. The couplings are

$$\begin{cases} \alpha_{12} &= \hat{e}_1 \cdot \hat{e}_2 = \cos(\theta_2) \\ \alpha_{13} &= \hat{e}_1 \cdot \hat{e}_3 = \cos(\theta_3) \\ \alpha_{23} &= \hat{e}_2 \cdot \hat{e}_3 = \sin(\theta_2)\sin(\theta_3)\left(\cos(\phi_2)\cos(\phi_3) + \sin(\phi_2)\sin(\phi_3)\right) + \cos(\theta_2)\cos(\theta_3) \end{cases}$$

With the imposition of the same value for any α_{ij}, it must hold that $\theta_2 = \theta_3 = \theta$, further implying the equation

$$\sin^2(\theta)\cos(\phi_2 - \phi_3) + \cos^2(\theta) = \alpha,$$

and therefore

$$\cos(\phi_2 - \phi_3) = \frac{\alpha}{1+\alpha},$$

which will have real solutions if and only if $\left|\frac{\alpha}{1+\alpha}\right| < 1$, thereby restraining the coupling value to $\alpha \in \left[-\frac{1}{2}, 1\right]$. In short, it will only be possible to set $\alpha_{ij} = \alpha \ \forall i, j$ by selecting $\theta_2 = \theta_3 = \theta$, such that $\cos(\theta) = \alpha$, and selecting values of ϕ_2, ϕ_3 such that $(\phi_2 - \phi_3) = \cos^{-1}\left(\frac{\alpha}{1+\alpha}\right)$, for $\alpha \in \left[-\frac{1}{2}, 1\right]$.

B Action-angle variables

Considering the Hamiltonian in equation 2.9 without coupling ($\alpha = 0$), the dynamics is separated into two symmetrical pendulum-like systems along each cartesian axis

$$H(x, y, p_x, p_y, \alpha = 0) = H_x + H_y = E_x + E_y \tag{6.1}$$

with

$$H_i = E_i = p_i^2 + U\cos^2(q_i) \qquad \text{for} \qquad i = x, y. \tag{6.2}$$

Consequently, the transformation to action angle variables $(x, y, p_x, p_y) \to (\theta_x, \theta_y, J_x, J_y)$ can be carried separately and identically for each unperturbed Hamiltonian H_i.

From its definition, the action J_i is proportional to the area enclosed by a trajectory in phase-space

$$J_i = \frac{1}{2\pi}\oint p_i dq_i = \frac{2}{\pi}\sqrt{E_i}\int_{\frac{\pi}{2}}^{q^*}\sqrt{1 - \bar{k}^2\cos^2(q_i)}dq_i \tag{6.3}$$

with $p_i = \sqrt{E_i - U\cos^2(q_i)}$. In the rightmost integral, the inferior limit of integration is taken at the rest position and the superior one as as the maximum oscillation amplitude, $q^* = \frac{\pi}{2} + \arcsin\left(\bar{k}^{-1}\right)$, for $\bar{k} = \sqrt{\frac{U}{E_i}} > 1$. These limits take into account symmetry properties of the trajectory in phase-space, which can be separated into 4 equal pieces of same area and be evaluated only during a quarter of a complete oscillation. Shifting $q_i \to \vartheta_i + \frac{\pi}{2}$, the integral 6.3 is seen to be an elliptical integral of second kind

$$\begin{aligned} J_i =& \frac{2}{\pi}\sqrt{E_i}\int_0^{\arcsin(\bar{k}^{-1})}\sqrt{1 - \bar{k}^2\sin^2(\vartheta_i)}d\vartheta_i \\ J_i =& \frac{2}{\pi}\sqrt{E_i}\ \ \mathbb{E}(\phi, \bar{k}), \end{aligned} \tag{6.4}$$

where $\phi = \arcsin(\bar{k}^{-1})$ is the phase parameter and $\bar{k}$ the modulus parameter [55]. One may note that for librational trajectories, $\bar{k}$ is bigger than 1, requiring the extension relation

$$\mathbb{E}(\phi, \bar{k}) = \bar{k}_1\left[\bar{k}^2\mathbb{E}(\phi_1, \bar{k}_1) + k'^2\mathbb{F}(\phi_1, \bar{k}_1)\right] \qquad \text{for} \qquad k > 1, \tag{6.5}$$

where $\mathbb{F}(\phi, k)$ is the elliptical function of first kind and the auxiliary parameters are

$$\bar{k}_1 = \frac{1}{\bar{k}}, \qquad \sin(\phi_1) = \bar{k}\sin(\phi), \qquad k'^2 = 1 - (\bar{k})^2. \tag{6.6}$$

The extended phase ϕ_1 is easily evaluated as

$$\phi_1 = \arcsin(\bar{k}\sin(\arcsin(\bar{k}^{-1}))) = \frac{\pi}{2}, \tag{6.7}$$

thereby meaning that the elliptical functions in equation 6.5 are complete, in the sense that the phase ranges from $0 \to \frac{\pi}{2}$. The action is then written as

$$J_i = \frac{2}{\pi}\sqrt{U}\ \Big[\mathbb{E}(k_i) + (k_i^2 - 1)\mathbb{K}(k_i)\Big] \tag{6.8}$$

with new modulus parameter $k_i^2 = (\bar{k}_i)^{-2} = \frac{E_i}{U} < 1$ and $\mathbb{K}(k)$ as the complete form of the elliptical function of first kind $\mathbb{F}(\phi, k)$.

Since (θ_i, J_i) are action-angles variables, the Hamiltonian H_i will depend only on the action J_i, implying that the angle θ_i evolves linearly in time $\theta_i(t) = \omega_i t$, with frequency calculated as

$$\begin{aligned}
\omega_i &= \frac{\partial E_i}{\partial J_i} = \frac{\partial E_i}{\partial k_i}\frac{\partial k_i}{\partial J_i} \\
\omega_i &= 2Uk_i\left[\frac{\partial}{\partial k_i}\left(\frac{2}{\pi}\sqrt{U}\left(\mathbb{E}(k_i) + (k_i^2 - 1)\mathbb{K}(k_i)\right)\right)\right]^{-1} \\
\omega_i &= \frac{\pi\sqrt{U}}{\mathbb{K}}
\end{aligned} \tag{6.9}$$

where the partial derivative property $\frac{\partial k_i}{\partial J_i} = \left(\frac{\partial J_i}{\partial k_i}\right)^{-1}$ was used.

The time dependence of the cartesian position q_i can be obtained by quadrature and its dependence with $\theta_i(t)$

$$\begin{aligned}
\frac{dq_i}{dt} &= \frac{\partial H_i}{\partial p_i} = 2p_i \\
\frac{1}{\sqrt{E_i}}\int_{\frac{\pi}{2}}^{q_i(t)} &\frac{1}{\sqrt{1 - \bar{k}\cos^2(q_i')}}dq_i' = \ 2t.
\end{aligned} \tag{6.10}$$

Similar to equation 6.4, by shifting $q_i \to \frac{\pi}{2} + \varphi$ the integral becomes the first elliptical form for extended parameter $\bar{k} > 1$, thus yielding

$$\frac{1}{\sqrt{E_i}}\ \frac{1}{\bar{k}}\mathbb{F}(\phi_1, k) = \ 2t \tag{6.11}$$

with extended phase $\phi_1 = \arcsin(\bar{k}\sin(q_i(t) - \frac{\pi}{2}))$. Comparing equations 6.11 and 6.9 and noticing that $\theta_i\omega_i^{-1} = t$, one can relate $\phi_1(q_i)$ with the modulus k_i and angle θ_i

$$\mathbb{F}(\phi_1, k) = 2\frac{\mathbb{K}\theta_i}{\pi}. \tag{6.12}$$

Inverting the equation above requires the use of elliptical inverse Jacobi functions $u =$

$\mathbb{F}(\phi_1, \bar{k})$, with the correspondent inverse $\mathrm{sn}(u|k) = \sin(\phi_1)$, thus yielding $q(k_i, \theta_i)$:

$$\begin{aligned} \mathrm{sn}\left(\mathbb{F}(\phi_1, k_1)\right) &= \mathrm{sn}\left(2\frac{\mathbb{K}\theta_i}{\pi}\right) \\ \phi_1 &= \arcsin\left(\mathrm{sn}\left(2\frac{\mathbb{K}\theta_i}{\pi}\right)\right) \end{aligned} \tag{6.13}$$

$$\boxed{q_i = \frac{\pi}{2} + \arcsin\left(k_i\ \mathrm{sn}\left(2\frac{\mathbb{K}(k_i)\ \theta_i}{\pi}\right)\right)}$$

The correspondent momentum p_i in its turn is promptly calculated by its motion equation:

$$\begin{aligned} p_i &= \frac{1}{2}\dot{q}_i \\ p_i &= \frac{1}{2}\frac{1}{\sqrt{1 - \left(k\ \mathrm{sn}(\frac{2\mathbb{K}}{\pi}\theta_i)\right)^2}}\frac{d}{dt}\left(k\ \mathrm{sn}\left(\frac{2\mathbb{K}}{\pi}\theta_i\right)\right) \\ p_i &= \frac{k\mathbb{K}}{\pi}\frac{1}{\sqrt{1 - k^2\ \mathrm{sn}^2(\frac{2\mathbb{K}}{\pi}\theta_i)}}\ \mathrm{cn}\left(\frac{2\mathbb{K}}{\pi}\theta_i\right)\mathrm{dn}\left(\frac{2\mathbb{K}}{\pi}\theta_i\right)\dot{\theta}_i \\ p_i &= k\sqrt{U}\ \mathrm{cn}\left(\frac{2\mathbb{K}}{\pi}\theta_i\right) \end{aligned} \tag{6.14}$$

where the following relations for inverse Jacobi elliptical functions were used:

$$\mathrm{cn}^2 + \mathrm{sn}^2 = 1, \qquad \mathrm{cn}^2 + (1-k^2)\mathrm{sn}^2 = \mathrm{dn}^2, \qquad \frac{d}{dz}\mathrm{sn}(z) = \mathrm{cn}(z)\mathrm{dn}(z). \tag{6.15}$$

Therefore, for the unperturbed square lattice Hamiltonian, librational orbits are analytically found as

$$q_i = \frac{\pi}{2} + \arcsin\left(k_i\ \mathrm{sn}\left(\frac{2\mathbb{K}(k_i)}{\pi}\theta_i\right)\right) \qquad p_i = k_i\sqrt{U}\mathrm{cn}\left(\frac{2\mathbb{K}(k_i)}{\pi}\theta_i\right) \tag{6.16}$$

and the related action-angle variables

$$J_i = \frac{2}{\pi}\sqrt{U}\ \left[\mathbb{E}(k_i) + (k_i^2 - 1)\mathbb{K}(k_i)\right], \qquad \theta_i = \frac{\sqrt{U}\pi}{\mathbb{K}(k_i)}\ t \qquad \text{for} \quad i = x, y. \tag{6.17}$$

C Symplectic numerical integration

In order to evaluate the performance of RKCK for long integration times, a comparison was made with an alternative symplectic method developed by Molei Tao [39]. Briefly, Tao's method integrates a d-degree of freedom Hamiltonian system $H(\vec{q}, \vec{p})$ by considering a new Hamiltonian $\bar{H}$, including new copy variables $(\vec{q}_c, \vec{p}_c)$, which start from the same initial point $(\vec{q}_c(0) = \vec{q}(0),\ \vec{p}_c(0) = \vec{p}(0))$ and are evolved along with the main variables $\vec{q}$

and $\vec{p}$ from the joint Hamiltonian

$$\bar{H}(\vec{q},\vec{q}_c,\vec{p},\vec{p}_c) = H_A + H_B + \omega H_C, \tag{6.18}$$

where $H_A \coloneqq H(\vec{q},\vec{p}_c)$ and $H_B \coloneqq H(\vec{q}_c,\vec{p})$ are copies of the original Hamiltonian function written with exchanged variables; ω is a scalar coupling factor and H_C the coupling perturbation

$$H_C(\vec{q},\vec{q}_c,\vec{p},\vec{p}_c) \coloneqq \frac{||\vec{q}-\vec{q}_c||^2}{2} + \frac{||\vec{p}-\vec{p}_c||^2}{2}. \tag{6.19}$$

An integration step of δt is thus made by the map $\phi_2^{\delta t}$ from Hamiltonian 6.18 as

$$\phi_2^{\delta t} \coloneqq \phi_{H_A}^{\delta t/2} \circ \phi_{H_B}^{\delta t/2} \circ \phi_{\omega H_C}^{\delta t} \circ \phi_{H_B}^{\delta t/2} \circ \phi_{H_A}^{\delta t/2} \tag{6.20}$$

where each partial mapping is given by:

$$\phi_{H_A}^{\delta t} \coloneqq \begin{pmatrix} \vec{q} \\ \vec{p} \\ \vec{q}_c \\ \vec{p}_c \end{pmatrix} \to \begin{pmatrix} \vec{q} \\ \vec{p} - \delta t \nabla_{\vec{q}} H(\vec{q},\vec{p}_c) \\ \vec{q}_c + \delta t \nabla_{\vec{p}_c} H(\vec{q},\vec{p}_c) \\ \vec{p}_c \end{pmatrix}, \qquad \phi_{H_B}^{\delta t} \coloneqq \begin{pmatrix} \vec{q} \\ \vec{p} \\ \vec{q}_c \\ \vec{p}_c \end{pmatrix} \to \begin{pmatrix} \vec{q} + \delta t \nabla_{\vec{p}} H(\vec{q}_c,\vec{p}) \\ \vec{p} \\ \vec{q}_c \\ \vec{p}_c - \delta t \nabla_{\vec{q}_c} H(\vec{q}_c,\vec{p}) \end{pmatrix} \tag{6.21}$$

and

$$\phi_{\omega H_C}^{\delta t} \coloneqq \begin{pmatrix} \vec{q} \\ \vec{p} \\ \vec{q}_c \\ \vec{p}_c \end{pmatrix} \to \frac{1}{2} \left(\begin{pmatrix} \vec{q}+\vec{q}_c \\ \vec{p}+\vec{p}_c \end{pmatrix} + R(\delta t) \begin{pmatrix} \vec{q}-\vec{q}_c \\ \vec{p}-\vec{p}_c \end{pmatrix} \right) \quad \text{where} \quad R(\delta) \coloneqq \begin{pmatrix} \cos(2\omega\delta t)\mathbb{I}_d & \sin(2\omega\delta t)\mathbb{I}_d \\ -\sin(2\omega\delta t)\mathbb{I}_d & \cos(2\omega\delta t)\mathbb{I}_d \end{pmatrix} \tag{6.22}$$

with $\mathbb{I}_d$ as the d-dimensional identity matrix. Considerations on which value ω may have are made further in this section. As showed above, Tao's method will be 2nd order, thus meaning 3rd order error [3], and it is explicitly symplectic as opposed to the more commonly find implicit symplectic integration algorithms.

The adaptive step size RKCK method was implemented with the GSL library for C/C++ [54] programing language whereas Tao's method was implemented manually in the same programming language with fixed time step of $\delta t = 10^{-5}$.

To evaluate the integration precision, two functions for constants of the motion were calculated. The energy $E = H(t)$, which is an immediate constant for conservative systems, and the symplectic 2-form δS between the vectors $\vec{z} = (z_1^q, ..., z_d^q, z_1^p, ..., z_d^p)$ and

[3] Higher orders can be achieved by concatenating steps as $\phi_l^\delta \coloneqq \phi_{l-2}^{\gamma_l \delta} \circ \phi_{l-2}^{(1-2\gamma_l)\delta} \circ \phi_{l-2}^{\gamma_l \delta}$, for $\gamma_l = (2 - 2^{\frac{1}{l+1}})^{-1}$ and l an even positive integer.

$\vec{w} = (w_1^q, ..., w_d^q, w_1^p, ..., w_d^p)$ in a d-degrees-of-freedom space:

$$\delta S(\vec{z}, \vec{w}) := \sum_{i=1}^{d} dq_i \wedge dp_i = \sum_{i=1}^{d} \left(z_i^q w_i^p - z_p^i w_i^q \right) \tag{6.23}$$

which is expected to be numerically conserved, at least for integrable orbits, if the integration method is symplectic.

For the calculation of the 2-form δS, a given initial condition is integrated along with a second one, slightly displaced from it, with initial point: $\vec{s_0} \to \vec{s_0} + \vec{\delta}$, for $|\vec{\delta}| = 10^{-10}$. The 2-form will thus measure how close the two paths remain throughout time evolution. For chaotic orbits it is expected that this orbits diverge exponentially, but the longer it takes for them to diverge, the better. For integrable orbits a good symplectic integration is expected to keep the 2-form limited and the lowest possible.

Four orbits were arbitrarily selected, two integrable and two chaotic, all of them for system parameters $\alpha = 0.1$ and $E = 25.0$; the initial points for each one are:

- Trajectory 0 (Chaotic): $(x_0, y_0, p_{x0}, p_{y0}) = (0.00000, 1.57070, -0.100000, 2.233745)$
- Trajectory 1 (Regular): $(x_0, y_0, p_{x0}, p_{y0}) = (1.57070, 1.57070, -0.100000, 4.999000)$
- Trajectory 2 (Regular): $(x_0, y_0, p_{x0}, p_{y0}) = (1.00000, 1.57070, 2.000000, 3.893746)$
- Trajectory 3 (Chaotic): $(x_0, y_0, p_{x0}, p_{y0}) = (1.57070, 1.57070, -3.000000, 4.000000)$

The points above were integrated for a total time of $t = 10^3$, which has the same magnitude as the longest time used in analysis over the 2D lattices, specifically on the diffusion and chaotic/regular area calculation (SALI method).

Figures 44 and 46 show the space trajectories for each initial point for the RKCK and Tao's method respectively. One can notice how the chaotic orbits densely fill the available space where $V(x, y) < E$ but with different concentration of paths in some areas. The energy and 2-form values are shown in figures 45, for RKCK, and 46 for Tao's method. Lastly, performances of both methods are summarized in table 3.

	CPU time†	δH	δS
Runge-Kutta-Cash-Karp	40 sec	10^{-9}	10^{1} (All)
Symplectic Tao	16 min	10^{-7}	10^{1} (trajs 0,3) | 10^{-7} (trajs 1,2)

Table 3: Performances of integration methods for a total time $t = 1000$ for the square lattice system. The values shown are in magnitude, not exact averages. For the symplectic 2-form, the result was split between regular and chaotic orbits when they differ. (†) CPU time is approximately the same for all four orbits, the value shown is the average.

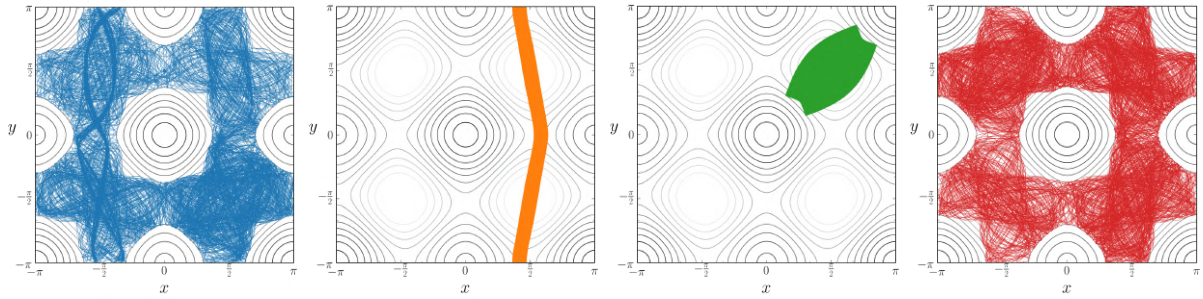

Figure 44: Spatial trajectories for the four initial conditions set integrated with RKCK for a total time $t = 1000$.

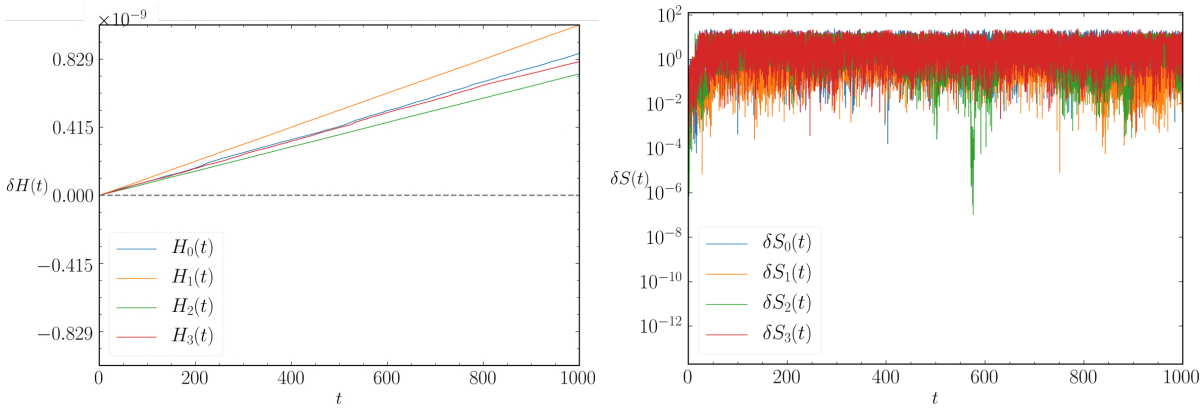

Figure 45: Energy deviation $\delta H = E_0 - H(t)$ (left) and symplectic 2-form δS (right) of trajectories integrated with the RKCK.

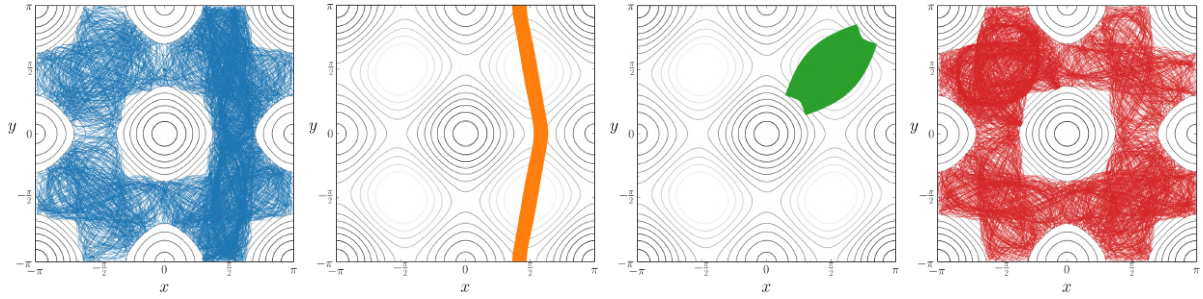

Figure 46: Spatial trajectories for the four initial conditions set integrated with the symplectic Tao method, with fixed time step $dt = 10^{-5}$ and total time $t = 1000$.

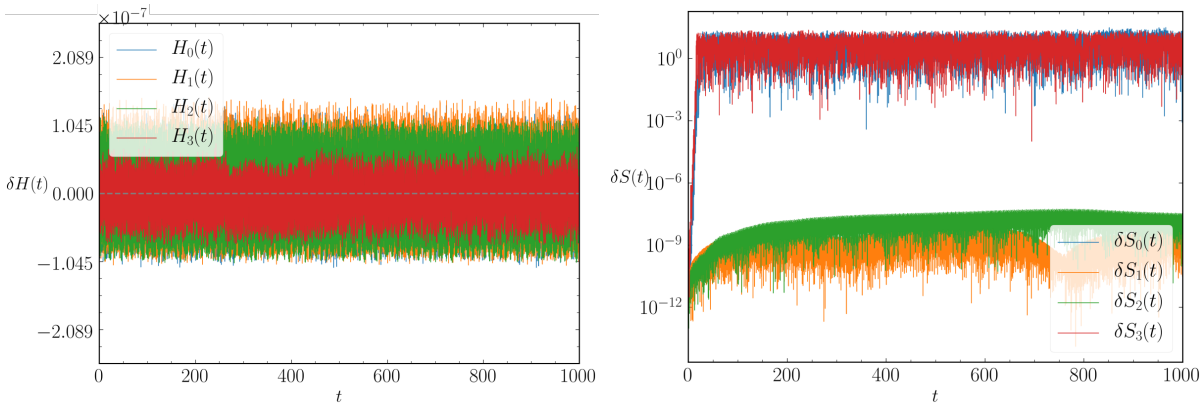

Figure 47: Energy deviation $\delta H = E_0 - H(t)$ (left) and symplectic 2-form δS (right) of trajectories integrated with the explicit symplectic Tao method with fixed time step $dt = 10^{-5}$ and total time $t = 1000$.

For the symplectic Tao method, the same coupling factor $\omega = 50$ was used for all orbits. To ensure this is a reasonable choice, a brief test on different ω values was made and the results summarized in table 4. The lowest value of $\omega = 2$ presented divergent errors, both in energy and symplectic 2-form, whereas values higher than order 10^1 kept conservation at order of magnitude 10^{-7}.

	δH	δS
Symplectic Tao ($\omega = 2$)	10^6	10^3 (all trajs)
Symplectic Tao ($\omega = 50$)	10^{-7}	10^1 (trajs 0,3) | 10^{-7} (trajs 1,2)
Symplectic Tao ($\omega = 100$)	10^{-7}	10^1 (trajs 0,3) | 10^{-7} (trajs 1,2)
Symplectic Tao ($\omega = 500$)	10^{-7}	10^1 (trajs 0,3) | 10^{-7} (trajs 1,2)
Symplectic Tao ($\omega = 2000$)	10^{-7}	10^1 (trajs 0,3) | 10^{-7} (trajs 1,2)

Table 4: Performance of symplectic Tao method for different choices of coupling factor ω for total integration time of $t = 1000$ for the square lattice system. Values are shown in magnitude, not exact averages. For the symplectic 2-form, the result was split between regular and chaotic orbits when they differ.

D Statistical convergence of the diffusion exponent

In order to ensure the statistical reliability of the calculated diffusion profiles, this section discusses the dependence of values of μ with the total integration time t and ensemble size N. This is done by comparing the simulation in the best case scenario (highest t or N, here taken as $t = 3 \times 10^3$ and $N = 3 \times 10^4$) with multiple other ones with lower values of t and N. It can be asserted then that the fluctuations and transitions found in the diffusion exponent are not due to statistical imprecision, but indeed caused by changes in the dynamics.

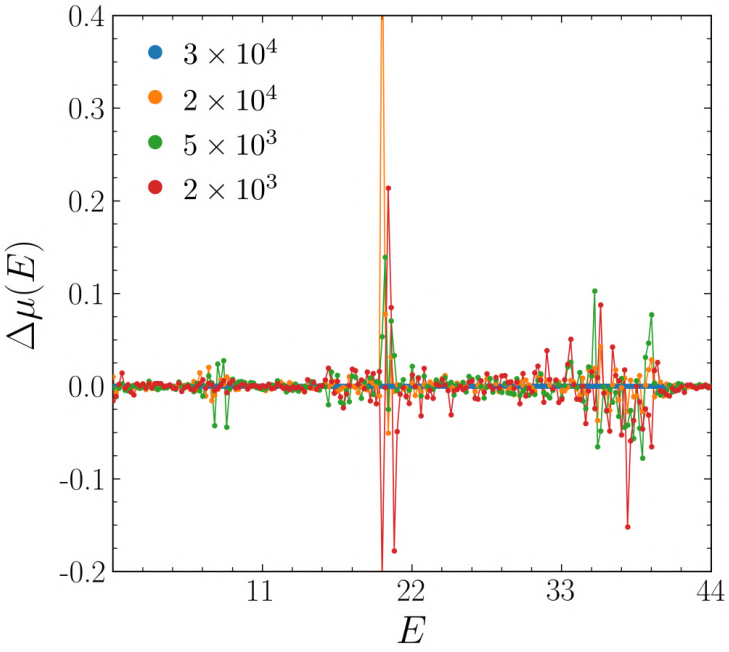

Figure 48: Diffusion exponent difference $\Delta\mu = \mu_N - \mu_n$ between different values of ensemble size n and the best case for $N = 3 \times 10^4$. For all cases: $t = 3000$ and $\alpha = 0.1$.

Figure 48 starts by showing the difference between ensemble sizes, $\Delta\mu = \mu_N - \mu_n$, with μ_N evaluated for the largest ensemble size and μ_n for a smaller one, for a series of n. In all cases, $\alpha = 0.1$ and $t = 3 \times 10^3$ are fixed. One can notice that the amplitudes of $\Delta\mu$ for different n are not large, with average difference being of order $\Delta\mu \approx 0.05$. A particularly larger deviation occurs around the energy value for diffusion onset, corresponding to $E = 19.8$ for $\alpha = 0.1$, although this is expected given the absolute amplitude variation of μ itself. Even though the test presented here comprises only a single value of α, it is expected that for other values this result still holds. One may also notice that simulations could be optimized by selecting N at least one order of magnitude smaller than the value used here, without qualitative loss on the final result.

Similarly, figure 49 shows the same procedure but for different integration times. Here the comparison is made as $\Delta\mu = \mu_T - \mu_t$, with μ_T obtained for the longest integration and μ_t for any smaller value. The results indicate a higher amplitude variation for the different t, but still below 0.15 in average. As in the case of different N, the same sensitivity is shown for energy values around transitions or high fluctuations of μ. Nonetheless, the data for different integration times present a trend of increasing values of $\mu(E)$ towards ballistic regime as the integration time increases. This is due to the presence of particles moving at ballistic rate that dominate the average displacement of the ensemble. However, the same result points out that convergence is close to the expected asymptotic limit.

In general, regardless of the sensitivity of $\Delta\mu$ around regions with high variation of μ, one can see that they occur at the same energy values. This allows us to assert that the transitions found in the exponent μ as we change the energy are not mere statistical artifacts. Also, some fluctuations become apparent just after a long transient; in fact they are not transitions properly said, in the sense that they correlate with major topological

changes in phase-space, but just a long time transient behavior due the appearance of small islands composed of long flights that dominate the ensemble average displacement (see appendix F).

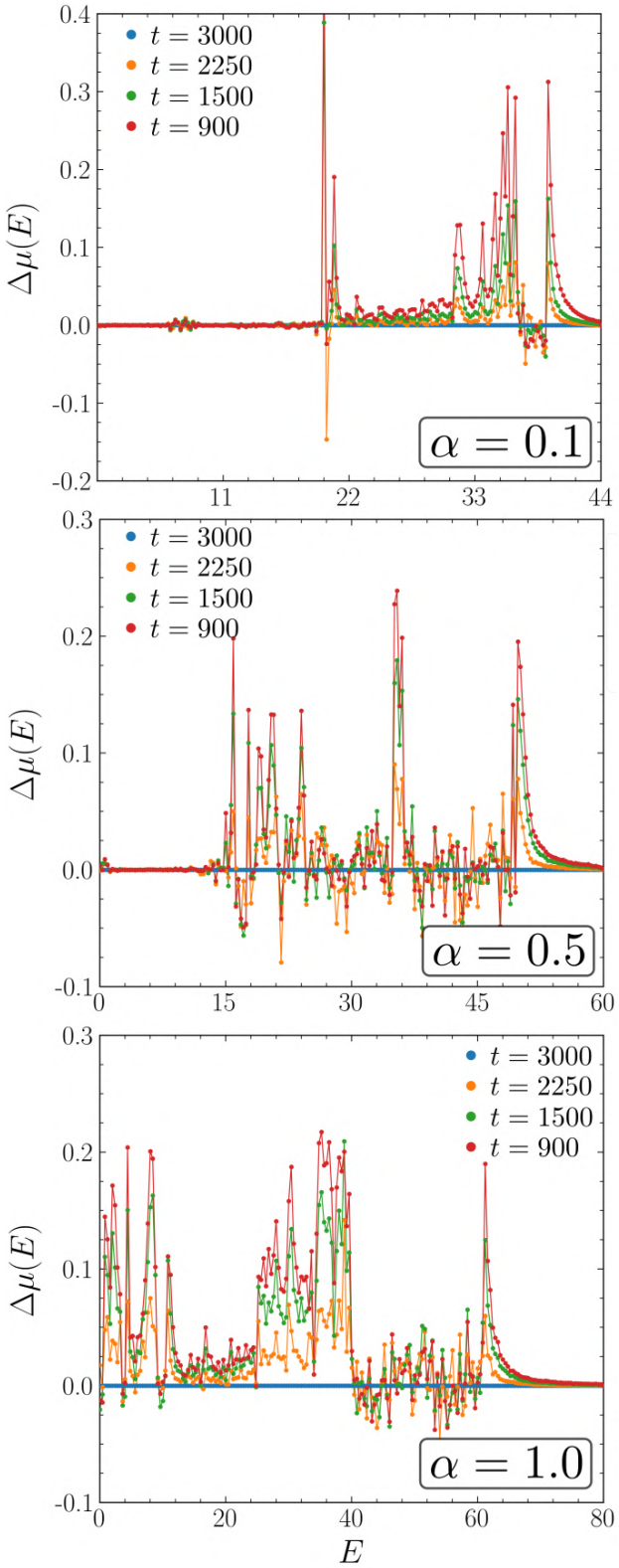

Figure 49: Diffusion exponent difference $\Delta\mu = \mu_T - \mu_t$ between different values of integration time t and the best case for $T = 3000$. In all cases, $N = 3 \times 10^4$.

E Symplectic integration performance for diffusion calculation

In order to assess the performance of integration over the long times required for diffusion exponent calculations, figure 50 compares the result between two methods: the non-symplectic RKCK and a symplectic one developed by M. Tao (appendix C). The particles ensemble is randomly generated in each simulation, but the remaining parameters are equivalent, *i.e.*, the total integration time $t = 10^3$ and ensemble size $N = 10^4$. The final values for $\mu(E)$ present a divergence of less than 0.15 when compared between the two methods. This indicates that even with the lack of symplecticity, RKCK method still provides good average results, regardless of deviations in particular trajectories, mostly due to its great energy conservation, which for the time considered is up to order 10^{-9}.

As an adaptive time-step method, the RKCK absolute and relative precisions were selected as: $\epsilon_{\text{abs}} = \epsilon_{\text{rel}} = 10^{-13}$. For Tao's method, time-step is fixed and was selected as $dt = 10^{-5}$. Also, Tao's method requires a binding factor parameter, which was set to $\omega = 100$, since it provided the best performance regarding energy conservation (up to 10^{-5}) and symplectic 2-form (up to 10^{-7}) (see appendix C).

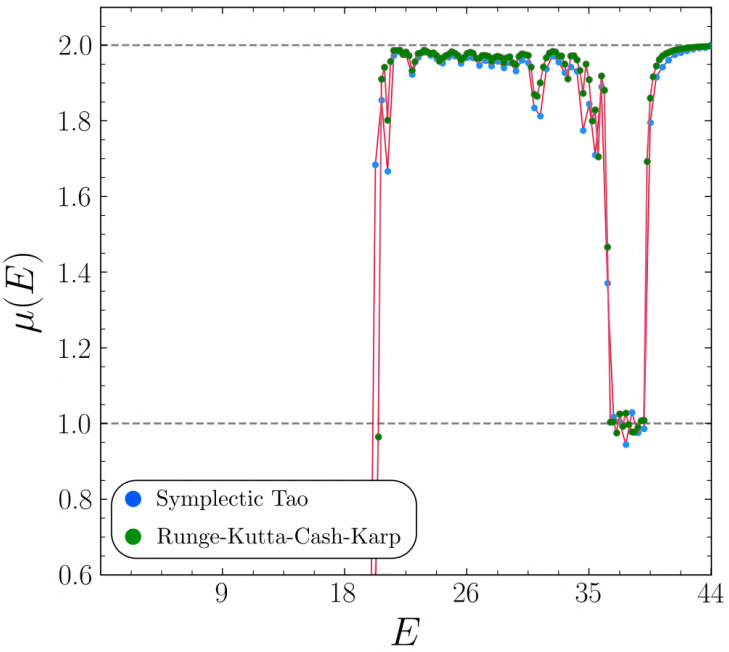

Figure 50: Comparison between diffusion exponent $\mu(E)$ calculation with RKCK and Tao's symplectic method.

F Local diffusion transitions

To fully explore the aspects of the diffusion profile obtained, this section briefly describes one example of a sudden change in diffusion uncorrelated with changes in chaotic area. Cases such as this are particularly visible in the region between local and global maxima lines in both diffusion and chaotic area color maps over parameter space (figs. 17 and 22 respectively).

As anticipated in the main text, area-uncorrelated transitions are associated to small

stability islands. The islands are small enough not to affect significantly the area measured but since they are composed of orbits traveling in straight paths through the lattice, they dominate the average $\langle R^2(t)\rangle$, increasing its asymptotic behavior towards free regime value ($\mu \to 2$). Therewith, to clearly display these small stable regions in phase-space, a displacement color map was used, coloring each initial point with its displacement after a given integration time t (here $t = 1000$). Figure 51 exemplifies this result for the transition at $E \approx 24$ and $\alpha = 0.5$, where a peak from $\mu \approx 1$ to $\mu \approx 1.3$ is found.

The only noticeable modification is the emergence of three small islands around each of the twin islands in the bottom region of the PSS, along with the bifurcation of these twin islands. The emergent island triads present a displacement of one order of magnitude higher than the surrounding chaotic sea. It is clear then that the ballistic transport due to these small islands increases the global average diffusion rate, making it increase quadratically but with smaller amplitude, thus taking longer times to increase μ but still converging towards $\mu \approx 2$. Although not shown here, the same behavior was found for other area-uncorrelated fluctuations.

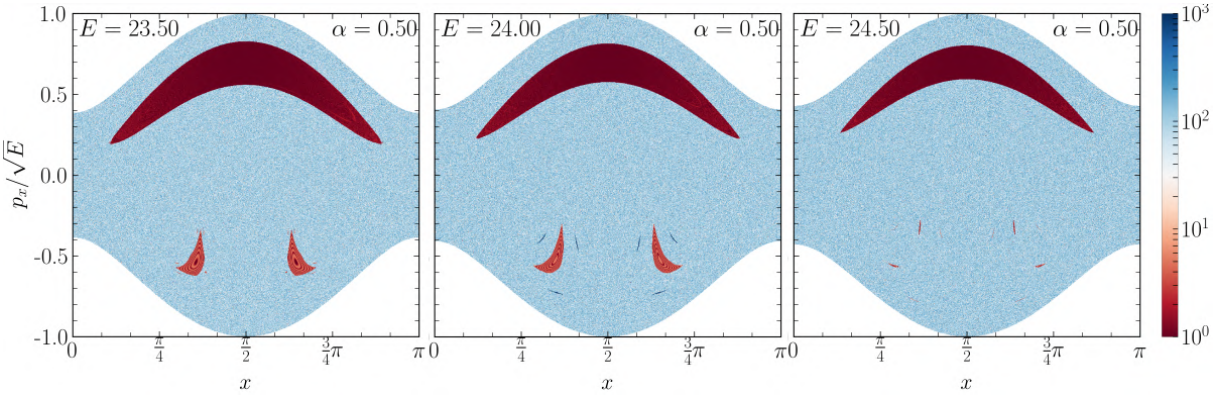

Figure 51: Displacement range color map for different energies around the sudden peak for $E \approx 24$. The integration time is $t = 10^3$ for each point in a 850×850 grid.

To emphasize that the variations for the energy values mentioned above are not global transitions, in the sense that they are not related to major changes in the chaotic domain, figure 52 shows the manifold structure for the same PSS shown in figure 51. Even though the island triads are not visible in the figure, one may notice that they appear between the manifold lobes without disturbing them. It is unexpected that islands with long displacement range appear amidst a chaotic sea with transport in a complete different regime, without major changes around it.

Consequently, for the diffusion calculation method used here, the presence of even small portions of phase-space with quadratic rate will imply a dominance over the total regime rate. Therefore, the method used requires this to be taken into consideration. Besides, this reiterates that fluctuations in diffusion will not necessarily correlate with the chaotic area, thus requiring a deeper inspection of properties and changes taking place in the system's phase-space to understand these modifications in transport.

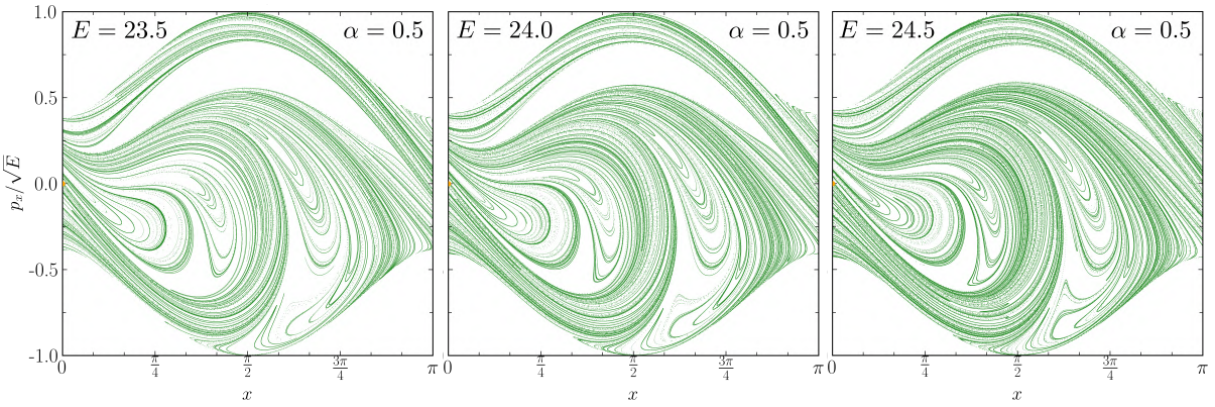

Figure 52: PSS portraits with the stable manifold branch from UPO U_y (along the stable direction of the saddle point at $(x_s, y_s) = (0, \cos^{-1}(\alpha))$) for different energies along the diffusion variation. Integration time is $t = 6.9$.

G Isochronous chains with higher multiplicity

Figure 53 shows a scenario where an isochronous island chain, of total period 12, is formed not by two orbits of period 6, but instead by two orbits of period 3 (shown in red and blue) and one of period 6 (shown in yellow). The orbits themselves are also presented, showing that they are indeed the same curve rotated and mirrored in three different ways. This particular case reveals that whenever an orbit's translation or rotation intersects the PSS with the same discrete period, isochronous chains with higher multiplicity may appear. However, for the square lattice, no more than 4 isochronous orbits can be expected to appear, since its symmetries are limited by rotations of $\pi/2$.

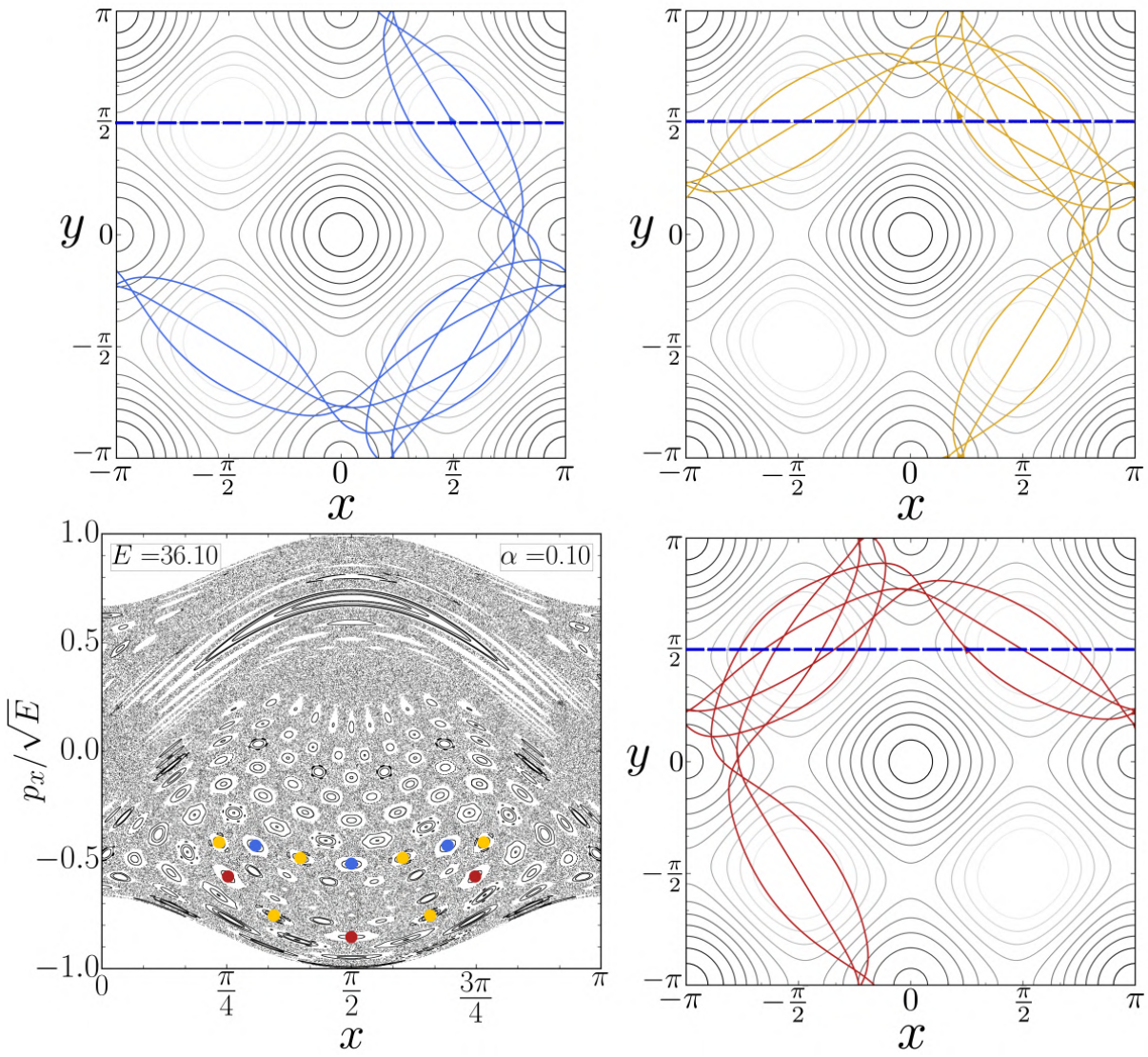

Figure 53: Myriad chain formed by three isochronous orbits. The colored dots indicate the fixed points of the trajectories relative to the PSS Σ (blue dotted line in trajectory frames).

H Phase-space near maximum potential energy

Figure 54 shows the island myriad emergence in phase-space for energy values close to the potential global maximum $V_{\text{g-max}} = 2U(1+\alpha)$. The emergent structure is qualitatively similar for any α considered, although the size of resonant islands increases with α. Along with the islands, an upper and bottom stability region is found.

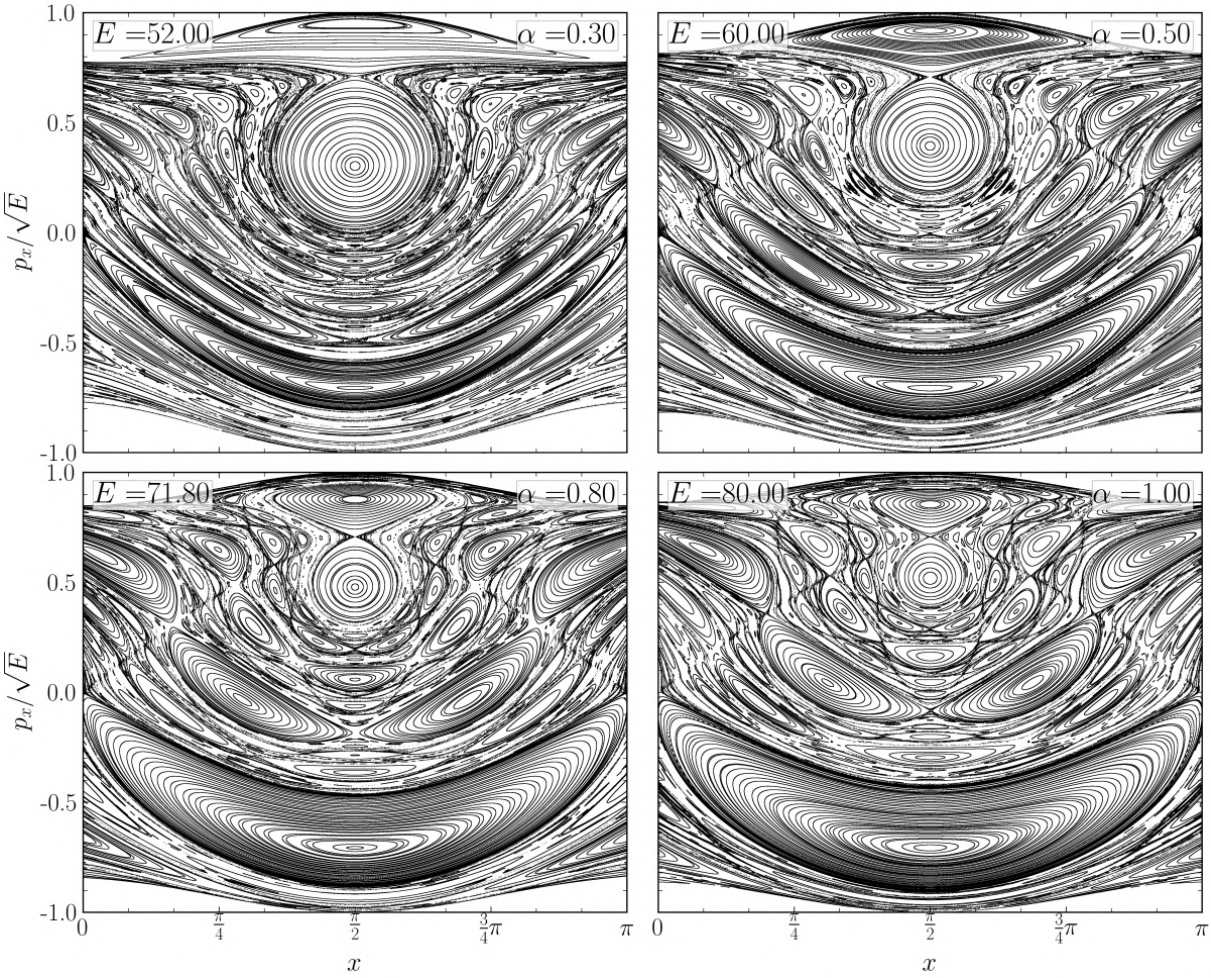

Figure 54: PSS ($y = \frac{\pi}{2}; p_y > 0$) calculated for energy values at the global maxima, showing the emergence of the island myriad for different couplings α. (Top left) $E = 52, \alpha = 0.3$. (Top right) $E = 60, \alpha = 0.5$. (Bottom left) $E = 72, \alpha = 0.8$. (Bottom right) $E = 80, \alpha = 1.0$.

References

[1] I. Bloch. Ultracold quantum gases in optical lattices. *Nature Physics*, 1:23–30, 2005.

[2] I. Bloch; J. Dalibard and W. Zwerger. Many-body physics with ultracold gases. *Reviews of modern physics*, 80:885–964, 2008.

[3] A. Hemmerich; D. Schropp Jr. and T. W. Hänsch. Light forces in two crossed standing waves with controlled time-phase difference. *Physical Review A*, 44(3):1911–1921, 1991.

[4] R. G. Kleva and J. F. Drake. Stochastic ExB particle transport. *Physics of Fluids*, 27(7):1686–1698, 1984.

[5] W. Horton. Nonlinear drift waves and transport in magnetized plasma. *Physics Reports*, 192(1-3):1–177, 1990.

[6] S.-P. Yu; J. A. Muniz; C.-L. Hung and H. J. Kimble. Two-dimensional photonic crystals for engineering atom-light interactions. *PNAS*, 116(26):12743–12751, 2019.

[7] D. S. Sholl and R. T. Skodje. Diffusion of xenon on a platinum surface: the influence of correlated flights. *Physica D*, 71:168–184, 1994.

[8] Q. Thommen; J.C. Garreau and V. Zehnlé. Classical chaos with Bose-Einstein condensates in tilted optical lattices. *Physical Review Letters*, 91(21):1–4, 2003.

[9] K. A. Mitchell and D. A. Steck. Fractal templates in the escape dynamics of trapped ultracold atoms. *Physical Review A*, 76(031403):1–4, 2007.

[10] S. V. Prants. Light-induced atomic elevator in optical lattices. *JETP Letters*, 104(11):749–753, 2016.

[11] S. V. Prants and L. E. Kon'kov. On the possibility of observing chaotic motion of cold atoms in rigid optical lattices. *Quantum Electronics*, 47(5):446–450, 2017.

[12] Y. Sinai. Dynamical systems with elastic reflections. ergodic properties of dispersing billiards. *Russ. Math. Surv.*, 25:137–189, 1970.

[13] J. Machta and R. Zwanzig. Diffusion in a periodic Lorentz gas. *Physical Review Letters*, 50(25), 1983.

[14] B. Bagchi; R. Zwanzig and M. C. Marchetti. Diffusion in a two-dimensional periodic potential. *Physical Review A*, 31(2):892–896, 1985.

[15] G. M. Zaslavsky; R. Z. Sagdeev; D. K. Chaikovsky and A. A. Chernikov. Chaos and two-dimensional random walk in periodic and quaseperiodic fields. *Sov. Phys. JETP*, 68(5):995–1000, 1989.

[16] G. M. Zaslavsky and M. K. Tippett. Connection between recurrence-time statistics and anomalous transport. *Physical Review Letters*, 67(23):3251–3254, 1991.

[17] G. M. Zaslavsky. Chaos, fractional kinetics, and anomalous transport. *Physics Reports*, 371:461–580, 2002.

[18] V. Yu. Argonov and S. V. Prants. Fractals and chaotic scattering of atoms in the field of a standing light wave. *Journal of Experimental and Theoretical Physics*, 96(5):832–845, 2003.

[19] V. Yu. Argonov and S. V. Prants. Nonlinear coherent dynamics of an atom in an optical lattice. *Journal of Russian Laser Research*, 27(4):360–378, 2006.

[20] V. Yu. Argonov and S. V. Prants. Theory of chaotic atomic transport in an optical lattice. *Physical Review A*, 75:063428, 2007.

[21] D. Mandal; Y. Elskens; X. Leoncini; N. Lemoine and F. Doveil. Sticky islands in stochastic webs and anomalous chaotic cross-field particle transport by ExB electron drift instability. *Chaos, Solitons and Fractals*, 145:110810, 2021.

[22] D. K. Chaikovsky and G. M. Zaslavsky. Channeling and percolation in two-dimensional chaotic dynamics. *Chaos*, 1:463, 1991.

[23] E. Horsley; S. Koppell and L. E. Reichl. Chaotic dynamics in a two-dimensional optical lattice. *Physical Review E*, 89(012917):1–5, 2014.

[24] M. D. Porter and I. E. Reichl. Chaos in the honeycomb optical-lattice unit cell. *Physical Review E*, 93(012204):1–7, 2016.

[25] M. D. Porter; A. Barr; A. Barr and L. E. Reichl. Chaos in the band structure of a soft Sinai lattice. *Physical Review E*, 95(052213):1–11, 2017.

[26] S. V. Prants. Weak chaos with cold atoms in a 2D optical lattice with orthogonal polarizations of laser beams. *Journal of Russian Laser Research*, 40(3):213–220, 2019.

[27] R. Grimm; M. Weidemuller and Y. B. Ovchinnikov. Optical dipole traps for neutral atoms. *Advances in Atomic, Molecular and optical physics*, 42:95–170, 2000.

[28] M. Greiner; I. Bloch; O. Mandel; T.W. Hänsch and T. Esslinger. Bose-Einstein condensates in 1D- and 2D optical lattices. *Applied Physics B*, 73:769–772, 2001.

[29] M. Greiner; I. Bloch; O. Mandel; T.W. Hänsch and T. Esslinger. Exploring phase coherence in a 2D lattice of Bose-Einstein condensates. *Physical Review Letters*, 87(16):1–4, 2001.

[30] J. S. Espinoza Ortiz; M. A. M. de Aguiar and A. M. Ozorio de Almeida. Scars of periodic orbits in the stadium action billiard. *Journal of Statistical Physics*, 83(1/2):275–287, 1996.

[31] M. C. Gutzwiller. *Chaos in Classical and Quantum Mechanics*. Springer-Verlag, New York, 1990.

[32] A. Kamor; C. Chandre; T. Uzer and F. Mauger. Recollision scenario without tunneling: Role of the ionic core potential. *Physical Review Letters*, 112(133003), 2014.

[33] F. Mauger; A. D. Bandrauk; A. Kamor; T. Uzer and C. Chandre. Quantum-classical correspondence in circularly polarized high harmonic generation. *Journal of Physics B: Atomic, Molecular and Optical Physics*, 47(041001):1–5, 2014.

[34] J. H. Conway; Heidi Burgiel and Chaim Goodman-Strauss. *The Symmetries of Things*. CRC Press, New York, 2008.

[35] S. H. Strogatz. *Nonlinear Dynamics and Chaos*. Perseus Books Publishing, New York, 1994.

[36] L. E. Reichl. *The Transition to Chaos in Conservative Classical Systems*. Springer-Verlag, New York, 1992.

[37] W. H. Press; S. A. Teukolsky; W. T. Vetterling; B. P. Flannery. *Numerical Recipes in C*. Cambridge University Press, Cambridge, UK, 2007.

[38] J. R. Cash and A. H. Karp. A variable order Runge-Kutta method for initial value problems with rapidly varying right-hand sides. *ACM Transactions on Mathematical Software*, (16):201–222, 1990.

[39] M. Tao. Explicit symplectic approximation of nonseparable hamiltonians algorithm and long time performance. *Physical Review E*, 94(4):1–13, 2016.

[40] G. M. Zaslavsky. *Hamiltonian Chaos and Fractional Dynamics*. Oxford University Press, Oxford, UK, 2005.

[41] M. Baranger; K. T. R. Davies and J. H. Mahoney. The calculation of periodic trajectories. *Annals of Physics*, (186):95–110, 1988.

[42] M. A. M. Aguiar; C. P. Malta; M. Baranger and K. T. R. Davies. Bifurcations of periodic trajectories in non-integrable hamiltonian systems with two degrees of freedom: Numerical and analytical results. *Annals of Physics*, (180):167–205, 1987.

[43] S. I. Tzenov. *Contemporary Accelerator Physics*. World Scientific, Singapore, 2004.

[44] V. A. Yakubovich and V. M. Starzhinskii. *Linear Differential Equations with Periodic Coefficients*. John Wiley and Sons, New York, Toronto, 1975.

[45] N. S. Simonovic. Calculations of periodic orbits: The monodromy method and application to regularized systems. *Chaos*, 9(4):854–864, 1999.

[46] K. T. Alligood; T. D. Sauer and J. A. Yorke. *Chaos: An Introduction to Dynamical Systems*. Springer-Verlag, New York, 1996.

[47] D. Ciro; I. L. Caldas; R. L. Viana and T. E. Evans. Efficient manifolds tracing for planar maps. *Chaos*, 28(093106):1–11, 2018.

[48] A. M. Ozorio de Almeida; N. De Leon; M. A. Mehta and C. C. Marston. Geometry and dynamics of stable and unstable cylinders in hamiltonian systems. *Physica D*, 46:265–285, 1990.

[49] G. A. Gottwald C. H. Skokos and J. Laskar. *Chaos Detection and Predictability*. Springer-Verlag, Heidelberg, 2015.

[50] C. Skokos; T. Bountis; C. G. Antonopoulos and M. N. Vrahatis. Detecting order and chaos in hamiltonian systems by the SALI method. *Journal of Physics A Mathematical and General*, 37:6269–6284, 2004.

[51] D. del Castillo-Negrete; J. M. Greene and P. J. Morrison. Area preserving nontwist maps: periodic orbits and transition to chaos. *Physica D*, 91(1):1–23, 1996.

[52] M. J. Lazarotto; I. L. Caldas and Y. Elskens. Diffusion transitions in a 2D periodic lattice. *Communications in Nonlinear Science and Numerical Simulation*, 112:106525, 2022.

[53] M. Gardner. *Penrose Tiles to Trapdoor Ciphers*. Cambridge University Press, Cambridge, 1997.

[54] M. Galassi; B. Gough; F. Rossi; J. Theiler; G. Jungman; M. Booth and J. Davies. GNU Scientific Library Reference Manual (2nd ed.) IBSN 0954161734. *Network Theory Limited*, 2001.

[55] P. F. Byrd and M. D. Friedman. *Handbook of Elliptic Integrals for Engineers and Physicists*. Springer, Berlin, 1954.